Summer 2023

Yield Extraction for the $\gamma d \rightarrow \Lambda X$ Reaction

K H P Nishadi Hasarangi Silva

Yield Extraction for the $\gamma d \to \Lambda X$ Reaction

by

K H P Nishadi Hasarangi Silva

Bachelor of Science
University of Colombo 2017

Submitted in Partial Fulfillment of the Requirements

for the Degree of Master of Science in

Physics

College of Arts and Sciences

University of South Carolina

2023

Accepted by:

Yordanka Ilieva, Director of Thesis

Ralf Gothe, Committee Member

Ann Vail, Dean of the Graduate School

Acknowledgments

Words cannot express my gratitude to my advisor, Prof. Yordanka Ilieva, who gave me valuable instructions on my journey; this Master's degree, and for her immense support. I also could not have undertaken this journey without the support of Professor Steffen Strauch, who generously provided knowledge and expertise. Additionally, this endeavor would not have been possible without the generous support from my group colleagues Anne, Brandon, and Dr. Matthew; a postdoctoral researcher.

I am also grateful to my teachers at the University of South Carolina; Prof. Matthias Schindler, Prof. Vladimir Gudkov, Prof. Pawel Mazur, Prof. Yuriy Pershin, Prof. Brett Altschul, Prof. Ralf Gothe, Prof. Fred Myhrer, and my teachers of my undergraduate university; University of Colombo, SriLanka and all the other teachers who impacted and inspired me.

Most importantly I would like to thank my parents and parents-in-law and my sister for their incredible support and encouragement and for all they have done to make my life happier. My heartfelt gratitude goes to my dear husband, who supported me in numerous ways to accomplish this target.

Lastly, I would be remiss in not mentioning my university colleagues from the Department of Physics and all the Sri Lankan friends from the USA for their invaluable help and friendship.

Abstract

Improving and adding new experimental measurements of hyperon-nucleon (YN) and hyperon-deuteron (Yd) cross sections is an active area in nuclear physics research. Scientists use such cross-section data to understand the composition of neutron stars and develop a comprehensive picture of the baryon-baryon interaction. Using high luminosity photon beam incident on a long liquid deuterium target and the CEBAF Large Acceptance Spectrometer (CLAS) at the Thomas Jefferson National Accelerator Facility (JLab), a sample of hyperon-deuteron elastic scattering events was previously identified. The E06-103 (g13) experiment was originally designed to address the scarcity of experimental data on hyperon photoproduction off the neutron in support of the JLab N^* program. However, the high statistics allows us to obtain meaningful signal for hyperon-deuteron scattering, where the hyperon beam is first photoproduced on a deuteron nucleus and then scattered on another nucleus in the same target cell. In order to obtain cross-section estimates from the elastic hyperon-deuteron sample, the number of beam lambda hyperons needs to be known. In this work, we extract the yield in $\gamma d \rightarrow \Lambda X$ reaction using data taken in the g13a experiment. By detecting the final state proton and π^- pairs, the Λ hyperons are identified. Background subtraction performed on event distributions over the hyperon mass yields the number of ΛX events originating within the target for various hyperon momenta and polar angles. A correction factor to the yields accounting for the error due to our assumption that the hyperon mass has a Gaussian shape has been estimated to be 15.5%. This analysis has established the foundational methods and techniques needed for the determination of the inclusive Λ photoproduction yields in

the g13 experiment and has provided preliminary yield estimates. Future work will include estimates of systematic uncertainties and acceptance normalization.

This work was supported in part by the U.S. NSF under award 2111050.

Table of Contents

Acknowledgments ii

Abstract iii

List of Tables vii

List of Figures viii

Chapter 1 Introduction 1

Chapter 2 Experiment and Experimental Setup 4

2.1 Overview 4

Chapter 3 Data Analysis 7

3.1 Extraction of the Inclusive Λ Photoproduction Yield 7

3.2 Exclusive Analysis 17

Chapter 4 Results 37

Chapter 5 Summary and Outlook 43

Bibliography 44

Appendix A Background subtracted $IM_{p\pi^-}$ histograms for the inclusive analysis fitted with Gaussian + second order polynomial functions for all $(p_\Lambda, \theta_\Lambda)$ bins . . . 45

Appendix B Background subtracted kaon-mass histogram for the exclusive analysis, fitted with Gaussian + exponential functions for all $IM^2_{p\pi^-}$ bins 97

Appendix C List of the $g13a$ runs 125

List of Tables

Table 2.1 List of the g13a runs according to the data taking period and electron beam energy. Experimental conditions were kept constant over three main run ranges. 5

Table 3.1 Number of good Λ counted in the data set for considered methods. 34

List of Figures

Figure 2.1 Schematic diagrams of the CLAS detector in Hall B. Left: side cross section. The beam is incident from left to right. Right: transverse cross section. The beam direction is into the page. In both schematics, one can see the three regions of drift chambers and the panels of TOF scintillator paddles. The Cherenkov counter and the electromagnetic calorimeters were not used in this analysis. The six-sector geometry can clearly be seen on the right figure. 6

Figure 3.1 β versus p for charged particles. One clearly sees pions, kaons, and protons. 8

Figure 3.2 $\Delta\beta$ versus p for positively-charged tracks assuming proton nominal mass. The red solid lines show our cut selecting protons for further analysis. The cuts were determined in a previous analysis [9]. Out of time protons populate the "wings" emanating from the true proton distribution at low momentum. Particles not consistent with the proton hypothesis show up in structures, such as the ones in the upper right area. 10

Figure 3.3 $\Delta\beta$ versus p for negatively-charged tracks assuming π^- nominal mass. One can see the effect of a wide selection cut applied on the reconstructed particle mass at a pre-processing stage that was not part of this work. 11

Figure 3.4 Left: z component of the production vertex of positively charged particles. Right: z component of the production vertex of negatively charged particles. The solid red lines show the cuts applied in this work. 12

Figure 3.5 Vertex time difference distribution using TOF timing. The coincidences between the tracks in the CLAS and the tagged photons are in the peak centered at zero. Photons from different electron beam bunches show in the smaller peaks that are 2.004-ns apart. 13

Figure 3.6 $IM_{p\pi^-}$ for each possible $p\pi^-$ pair combination. One can see the ΛX events in the peak centered at the nominal Λ mass. 14

Figure 3.7 θ_Λ versus p_Λ. 15

Figure 3.8 Top: $IM_{p\pi^-}$ distribution fitted with a sum of a Gaussian and a second-order polynomial for the bin of $1.3 < p_\Lambda < 1.4$ GeV/c and $0.6 < \theta_\Lambda < 0.7$ rad. Bottom: Background-subtracted histogram obtained by subtracting the fitted polynomial from the $IM_{p\pi^-}$ distribution. 16

Figure 3.9 $\Delta\beta$ versus p for positively-charged tracks assuming proton nominal mass. 19

Figure 3.10 $\Delta\beta$ versus p for negatively-charged tracks assuming π^- nominal mass. 19

Figure 3.11 $\Delta\beta$ versus p for positively-charged tracks assuming K^+ nominal mass. 20

Figure 3.12 Left: z component of the production vertex of positively charged particles. Right: z component of the production vertex of negatively charged particles. The solid vertical lines denote the cuts applied to reduce background in the data sample. 20

Figure 3.13 Left:$MM_{K^+\Lambda X}{}^2$ versus $MM_{pp\pi^-}{}^2$. Right:$MM_{K^+\Lambda X}{}^2$ versus $MM_{p\pi^+\pi^-}{}^2$. 22

Figure 3.14 $E_{\gamma good}$ versus $MM_{K^+\Lambda X}{}^2$ distribution after PID, z-vertex, photon selection, and veto cuts. 23

Figure 3.15 $IM^2_{p\pi^-}$ versus $MM_{K^+\Lambda X}{}^2$ distribution after PID, z-vertex, and veto cuts. 24

Figure 3.16 $MM_{K^+\Lambda X}{}^2$ distribution after PID, z vertex, photon selection, veto, $IM^2_{p\pi^-}$, and $E_{\gamma good}$ cuts. 25

Figure 3.17 $IM^2_{p\pi^-}$ versus $MM_{pp\pi^-}{}^2$ distribution after all the cuts applied. . . 26

Figure 3.18 $IM^2_{p\pi^-}$ versus $MM_{p\pi^-\pi^+}{}^2$ distribution after all the cuts applied. . 27

Figure 3.19 $IM_{p\pi^-}{}^2$ distribution after all the cuts applied. 28

Figure 3.20 Reconstructed mass squared of K^+ after all the cuts have been applied. 29

Figure 3.21 $IM_{p\pi^-}{}^2$ histogram for exclusive analysis excluding $\Delta\beta$ K^+ cut. . . 29

Figure 3.22 Reconstructed mass of K^+ after all the cuts were applied and the $\Delta\beta$ selection cut on K^+ was removed. 30

Figure 3.23 Reconstructed mass of K^+ distribution for $IM_{p\pi^-}{}^2$ bin 1.32 – 1.33 $((\mathrm{GeV}/c^2)^2)$ fitted with Gaussian+second order polynomial (K^+ $\Delta\beta$ cut is excluded). 31

Figure 3.24 Reconstructed mass of K^+ distribution for $IM_{p\pi^-}{}^2$ bin 1.32 – 1.33 $((\mathrm{GeV}/c^2)^2)$ fitted with Gaussian+exponential (K^+ $\Delta\beta$ cut is excluded). 32

Figure 3.25 Reconstructed mass of K^+ distribution for $IM_{p\pi^-}{}^2$ bin 1.32 – 1.33 $((\mathrm{GeV}/c^2)^2)$ fitted with Gaussian+exponential (K^+ $\Delta\beta$ cut is included). 33

Figure 3.26 Number of Λ events versus the average value of $IM_{p\pi^-}{}^2$ bin obtained with three methods discussed in the text. 34

Figure 3.27 Background subtraction of the $IM_{p\pi^-}{}^2$ histogram when excluding the $\Delta\beta$ K^+ cut, fitted with Gaussian + second order polynomial functions. The Λ events within the background-subtracted Gaussian peak were counted in the range of 1.22 – 1.27 $(\mathrm{GeV}/c^2)^2$. 36

Figure 4.1 N_Λ versus θ. The statistical uncertainty of the yield is smaller than the marker size for each data point. The X error bars show the width of the θ bin. 38

Figure 4.2 Mean value of Gaussain peak fit of background subtracted histograms of $IM_{p\pi^-}$ distribution for each $(p_\Lambda, \theta_\Lambda)$ bin. 39

Figure 4.3 Standard deviation value of Gaussian peak fit of background subtracted histograms of $IM_{p\pi^-}$ distribution for each $(p_\Lambda, \theta_\Lambda)$ bin. 41

Figure 4.4 Standard deviation value of Gaussian peak fit of background subtracted histograms of $IM_{p\pi^-}$ distribution for each $(\theta_\Lambda, p_\Lambda)$ bin. 42

Figure A.1 Background subtraction on $IM_{p\pi^-}$ for the inclusive analysis using a fit to a Gaussian + second order polynomial functions for $p_\Lambda = [0.5, 0.6]$ GeV/c and $\theta_\Lambda = [0.4, 0.5]$ rad. 46

Figure A.2 Background subtraction on $IM_{p\pi^-}$ for the inclusive analysis using a fit to a Gaussian + second order polynomial functions for $p_\Lambda = [0.5, 0.6]$ GeV/c and $\theta_\Lambda = [0.5, 0.6]$ rad. 47

Figure A.3 Background subtraction on $IM_{p\pi^-}$ for the inclusive analysis using a fit to a Gaussian + second order polynomial functions for $p_\Lambda = [0.6, 0.7]$ GeV/c and $\theta_\Lambda = [0.3, 0.4]$ rad. 48

Figure A.4 Background subtraction on $IM_{p\pi^-}$ for the inclusive analysis using a fit to a Gaussian + second order polynomial functions for $p_\Lambda = [0.6, 0.7]$ GeV/c and $\theta_\Lambda = [0.4, 0.5]$ rad. 49

Figure A.5 Background subtraction on $IM_{p\pi^-}$ for the inclusive analysis using a fit to a Gaussian + second order polynomial functions for $p_\Lambda = [0.6, 0.7]$ GeV/c and $\theta_\Lambda = [0.5, 0.6]$ rad. 50

Figure A.6 Background subtraction on $IM_{p\pi^-}$ for the inclusive analysis using a fit to a Gaussian + second order polynomial functions for $p_\Lambda = [0.6, 0.7]$ GeV/c and $\theta_\Lambda = [0.6, 0.7]$ rad. 51

Figure A.7 Background subtraction on $IM_{p\pi^-}$ for the inclusive analysis using a fit to a Gaussian + second order polynomial functions for $p_\Lambda = [0.6, 0.7]$ GeV/c and $\theta_\Lambda = [0.7, 0.8]$ rad. 52

Figure A.8 Background subtraction on $IM_{p\pi^-}$ for the inclusive analysis using a fit to a Gaussian + second order polynomial functions for $p_\Lambda = [0.6, 0.7]$ GeV/c and $\theta_\Lambda = [0.8, 0.9]$ rad. 53

Figure A.9 Background subtraction on $IM_{p\pi^-}$ for the inclusive analysis using a fit to a Gaussian + second order polynomial functions for $p_\Lambda = [0.7, 0.8]$ GeV/c and $\theta_\Lambda = [0.4, 0.5]$ rad. 54

Figure A.10 Background subtraction on $IM_{p\pi^-}$ for the inclusive analysis using a fit to a Gaussian + second order polynomial functions for $p_\Lambda = [0.7, 0.8]$ GeV/c and $\theta_\Lambda = [0.5, 0.6]$ rad. 55

Figure A.11 Background subtraction on $IM_{p\pi^-}$ for the inclusive analysis using a fit to a Gaussian + second order polynomial functions for $p_\Lambda = [0.7, 0.8]$ GeV/c and $\theta_\Lambda = [0.6, 0.7]$ rad. 56

Figure A.12 Background subtraction on $IM_{p\pi^-}$ for the inclusive analysis using a fit to a Gaussian + second order polynomial functions for $p_\Lambda = [0.7, 0.8]$ GeV/c and $\theta_\Lambda = [0.7, 0.8]$ rad. 57

Figure A.13 Background subtraction on $IM_{p\pi^-}$ for the inclusive analysis using a fit to a Gaussian + second order polynomial functions for $p_\Lambda = [0.7, 0.8]$ GeV/c and $\theta_\Lambda = [0.8, 0.9]$ rad. 58

Figure A.14 Background subtraction on $IM_{p\pi^-}$ for the inclusive analysis using a fit to a Gaussian + second order polynomial functions for $p_\Lambda = [0.8, 0.9]$ GeV/c and $\theta_\Lambda = [0.3, 0.4]$ rad. 59

Figure A.15 Background subtraction on $IM_{p\pi^-}$ for the inclusive analysis using a fit to a Gaussian + second order polynomial functions for $p_\Lambda = [0.8, 0.9]$ GeV/c and $\theta_\Lambda = [0.4, 0.5]$ rad. 60

Figure A.16 Background subtraction on $IM_{p\pi^-}$ for the inclusive analysis using a fit to a Gaussian + second order polynomial functions for $p_\Lambda = [0.8, 0.9]$ GeV/c and $\theta_\Lambda = [0.5, 0.6]$ rad. 61

Figure A.17 Background subtraction on $IM_{p\pi^-}$ for the inclusive analysis using a fit to a Gaussian + second order polynomial functions for $p_\Lambda = [0.8, 0.9]$ GeV/c and $\theta_\Lambda = [0.6, 0.7]$ rad. 62

Figure A.18 Background subtraction on $IM_{p\pi^-}$ for the inclusive analysis using a fit to a Gaussian + second order polynomial functions for $p_\Lambda = [0.8, 0.9]$ GeV/c and $\theta_\Lambda = [0.7, 0.8]$ rad. 63

Figure A.19 Background subtraction on $IM_{p\pi^-}$ for the inclusive analysis using a fit to a Gaussian + second order polynomial functions for $p_\Lambda = [0.8, 0.9]$ GeV/c and $\theta_\Lambda = [0.8, 0.9]$ rad. 64

Figure A.20 Background subtraction on $IM_{p\pi^-}$ for the inclusive analysis using a fit to a Gaussian + second order polynomial functions for $p_\Lambda = [0.9, 1.0]$ GeV/c and $\theta_\Lambda = [0.2, 0.3]$ rad. 65

Figure A.21 Background subtraction on $IM_{p\pi^-}$ for the inclusive analysis using a fit to a Gaussian + second order polynomial functions for $p_\Lambda = [0.9, 1.0]$ GeV/c and $\theta_\Lambda = [0.3, 0.4]$ rad. 66

Figure A.22 Background subtraction on $IM_{p\pi^-}$ for the inclusive analysis using a fit to a Gaussian + second order polynomial functions for $p_\Lambda = [0.9, 1.0]$ GeV/c and $\theta_\Lambda = [0.4, 0.5]$ rad. 67

Figure A.23 Background subtraction on $IM_{p\pi^-}$ for the inclusive analysis using a fit to a Gaussian + second order polynomial functions for $p_\Lambda = [0.9, 1.0]$ GeV/c and $\theta_\Lambda = [0.5, 0.6]$ rad. 68

Figure A.24 Background subtraction on $IM_{p\pi^-}$ for the inclusive analysis using a fit to a Gaussian + second order polynomial functions for $p_\Lambda = [0.9, 1.0]$ GeV/c and $\theta_\Lambda = [0.6, 0.7]$ rad. 69

Figure A.25 Background subtraction on $IM_{p\pi^-}$ for the inclusive analysis using a fit to a Gaussian + second order polynomial functions for $p_\Lambda = [0.9, 1.0]$ GeV/c and $\theta_\Lambda = [0.7, 0.8]$ rad. 70

Figure A.26 Background subtraction on $IM_{p\pi^-}$ for the inclusive analysis using a fit to a Gaussian + second order polynomial functions for $p_\Lambda = [0.9, 1.0]$ GeV/c and $\theta_\Lambda = [0.8, 0.9]$ rad. 71

Figure A.27 Background subtraction on $IM_{p\pi^-}$ for the inclusive analysis using a fit to a Gaussian + second order polynomial functions for $p_\Lambda = [1.0, 1.1]$ GeV/c and $\theta_\Lambda = [0.2, 0.3]$ rad. 72

Figure A.28 Background subtraction on $IM_{p\pi^-}$ for the inclusive analysis using a fit to a Gaussian + second order polynomial functions for $p_\Lambda = [1.0, 1.1]$ GeV/c and $\theta_\Lambda = [0.3, 0.4]$ rad. 73

Figure A.29 Background subtraction on $IM_{p\pi^-}$ for the inclusive analysis using a fit to a Gaussian + second order polynomial functions for $p_\Lambda = [1.0, 1.1]$ GeV/c and $\theta_\Lambda = [0.4, 0.5]$ rad. 74

Figure A.30 Background subtraction on $IM_{p\pi^-}$ for the inclusive analysis using a fit to a Gaussian + second order polynomial functions for $p_\Lambda = [1.0, 1.1]$ GeV/c and $\theta_\Lambda = [0.5, 0.6]$ rad. 75

Figure A.31 Background subtraction on $IM_{p\pi^-}$ for the inclusive analysis using a fit to a Gaussian + second order polynomial functions for $p_\Lambda = [1.0, 1.1]$ GeV/c and $\theta_\Lambda = [0.6, 0.7]$ rad. 76

Figure A.32 Background subtraction on $IM_{p\pi^-}$ for the inclusive analysis using a fit to a Gaussian + second order polynomial functions for $p_\Lambda = [1.0, 1.1]$ GeV/c and $\theta_\Lambda = [0.7, 0.8]$ rad. 77

Figure A.33 Background subtraction on $IM_{p\pi^-}$ for the inclusive analysis using a fit to a Gaussian + second order polynomial functions for $p_\Lambda = [1.1, 1.2]$ GeV/c and $\theta_\Lambda = [0.2, 0.3]$ rad. 78

Figure A.34 Background subtraction on $IM_{p\pi^-}$ for the inclusive analysis using a fit to a Gaussian + second order polynomial functions for $p_\Lambda = [1.1, 1.2]$ GeV/c and $\theta_\Lambda = [0.3, 0.4]$ rad. 79

Figure A.35 Background subtraction on $IM_{p\pi^-}$ for the inclusive analysis using a fit to a Gaussian + second order polynomial functions for $p_\Lambda = [1.1, 1.2]$ GeV/c and $\theta_\Lambda = [0.4, 0.5]$ rad. 80

Figure A.36 Background subtraction on $IM_{p\pi^-}$ for the inclusive analysis using a fit to a Gaussian + second order polynomial functions for $p_\Lambda = [1.1, 1.2]$ GeV/c and $\theta_\Lambda = [0.5, 0.6]$ rad. 81

Figure A.37 Background subtraction on $IM_{p\pi^-}$ for the inclusive analysis using a fit to a Gaussian + second order polynomial functions for $p_\Lambda = [1.1, 1.2]$ GeV/c and $\theta_\Lambda = [0.6, 0.7]$ rad. 82

Figure A.38 Background subtraction on $IM_{p\pi^-}$ for the inclusive analysis using a fit to a Gaussian + second order polynomial functions for $p_\Lambda = [1.1, 1.2]$ GeV/c and $\theta_\Lambda = [0.7, 0.8]$ rad. 83

Figure A.39 Background subtraction on $IM_{p\pi^-}$ for the inclusive analysis using a fit to a Gaussian + second order polynomial functions for $p_\Lambda = [1.2, 1.3]$ GeV/c and $\theta_\Lambda = [0.2, 0.3]$ rad. 84

Figure A.40 Background subtraction on $IM_{p\pi^-}$ for the inclusive analysis using a fit to a Gaussian + second order polynomial functions for $p_\Lambda = [1.2, 1.3]$ GeV/c and $\theta_\Lambda = [0.3, 0.4]$ rad. 85

Figure A.41 Background subtraction on $IM_{p\pi^-}$ for the inclusive analysis using a fit to a Gaussian + second order polynomial functions for $p_\Lambda = [1.2, 1.3]$ GeV/c and $\theta_\Lambda = [0.4, 0.5]$ rad. 86

Figure A.42 Background subtraction on $IM_{p\pi^-}$ for the inclusive analysis using a fit to a Gaussian + second order polynomial functions for $p_\Lambda = [1.2, 1.3]$ GeV/c and $\theta_\Lambda = [0.5, 0.6]$ rad. 87

Figure A.43 Background subtraction on $IM_{p\pi^-}$ for the inclusive analysis using a fit to a Gaussian + second order polynomial functions for $p_\Lambda = [1.2, 1.3]$ GeV/c and $\theta_\Lambda = [0.6, 0.7]$ rad. 88

Figure A.44 Background subtraction on $IM_{p\pi^-}$ for the inclusive analysis using a fit to a Gaussian + second order polynomial functions for $p_\Lambda = [1.3, 1.4]$ GeV/c and $\theta_\Lambda = [0.2, 0.3]$ rad. 89

Figure A.45 Background subtraction on $IM_{p\pi^-}$ for the inclusive analysis using a fit to a Gaussian + second order polynomial functions for $p_\Lambda = [1.3, 1.4]$ GeV/c and $\theta_\Lambda = [0.3, 0.4]$ rad. 90

Figure A.46 Background subtraction on $IM_{p\pi^-}$ for the inclusive analysis using a fit to a Gaussian + second order polynomial functions for $p_\Lambda = [1.3, 1.4]$ GeV/c and $\theta_\Lambda = [0.4, 0.5]$ rad. 91

Figure A.47 Background subtraction on $IM_{p\pi^-}$ for the inclusive analysis using a fit to a Gaussian + second order polynomial functions for $p_\Lambda = [1.3, 1.4]$ GeV/c and $\theta_\Lambda = [0.5, 0.6]$ rad. 92

Figure A.48 Background subtraction on $IM_{p\pi^-}$ for the inclusive analysis using a fit to a Gaussian + second order polynomial functions for $p_\Lambda = [1.3, 1.4]$ GeV/c and $\theta_\Lambda = [0.6, 0.7]$ rad. 93

Figure A.49 Background subtraction on $IM_{p\pi^-}$ for the inclusive analysis using a fit to a Gaussian + second order polynomial functions for $p_\Lambda = [1.4, 1.5]$ GeV/c and $\theta_\Lambda = [0.2, 0.3]$ rad. 94

Figure A.50 Background subtraction on $IM_{p\pi^-}$ for the inclusive analysis using a fit to a Gaussian + second order polynomial functions for $p_\Lambda = [1.4, 1.5]$ GeV/c and $\theta_\Lambda = [0.3, 0.4]$ rad. 95

Figure A.51 Background subtraction on $IM_{p\pi^-}$ for the inclusive analysis using a fit to a Gaussian + second order polynomial functions for $p_\Lambda = [1.4, 1.5]$ GeV/c and $\theta_\Lambda = [0.4, 0.5]$ rad. 96

Figure B.1 Background subtracted kaon-mass histogram for the exclusive analysis, fitted with Gaussian + exponential functions for $IM^2_{p\pi^-}$ bin 1.17 – 1.18 ((GeV/c^2)^2). 97

Figure B.2 Background subtracted kaon-mass histogram for the exclusive analysis, fitted with Gaussian + exponential functions for $IM^2_{p\pi^-}$ bin 1.18 – 1.19 ((GeV/c^2)^2). 98

Figure B.3 Background subtracted kaon-mass histogram for the exclusive analysis, fitted with Gaussian + exponential functions for $IM^2_{p\pi^-}$ bin 1.19 – 1.20 ((GeV/c^2)^2). 99

Figure B.4 Background subtracted kaon-mass histogram for the exclusive analysis, fitted with Gaussian + exponential functions for $IM^2_{p\pi^-}$ bin 1.20 – 1.21 ((GeV/c^2)^2). 100

Figure B.5 Background subtracted kaon-mass histogram for the exclusive analysis, fitted with Gaussian + exponential functions for $IM^2_{p\pi^-}$ bin 1.21 – 1.22 ((GeV/c^2)^2). 101

Figure B.6 Background subtracted kaon-mass histogram for the exclusive analysis, fitted with Gaussian + exponential functions for $IM^2_{p\pi^-}$ bin 1.22 – 1.23 ((GeV/c^2)^2). 102

Figure B.7 Background subtracted kaon-mass histogram for the exclusive analysis, fitted with Gaussian + exponential functions for $IM^2_{p\pi^-}$ bin 1.23 – 1.24 ((GeV/c^2)^2). 103

Figure B.8 Background subtracted kaon-mass histogram for the exclusive analysis, fitted with Gaussian + exponential functions for $IM^2_{p\pi^-}$ bin 1.24 – 1.25 ((GeV/c^2)^2). 104

Figure B.9 Background subtracted kaon-mass histogram for the exclusive analysis, fitted with Gaussian + exponential functions for $IM^2_{p\pi^-}$ bin 1.25 – 1.26 ((GeV/c^2)^2). 105

Figure B.10 Background subtracted kaon-mass histogram for the exclusive analysis, fitted with Gaussian + exponential functions for $IM^2_{p\pi^-}$ bin 1.26 – 1.27 ((GeV/c^2)^2). 106

Figure B.11 Background subtracted kaon-mass histogram for the exclusive analysis, fitted with Gaussian + exponential functions for $IM^2_{p\pi^-}$ bin 1.27 – 1.28 ((GeV/c^2)^2). 107

Figure B.12 Background subtracted kaon-mass histogram for the exclusive analysis, fitted with Gaussian + exponential functions for $IM^2_{p\pi^-}$ bin 1.28 – 1.29 ((GeV/c^2)^2). 108

Figure B.13 Background subtracted kaon-mass histogram for the exclusive analysis, fitted with Gaussian + exponential functions for $IM^2_{p\pi^-}$ bin 1.29 – 1.30 ((GeV/c^2)^2). 109

Figure B.14 Background subtracted kaon-mass histogram for the exclusive analysis, fitted with Gaussian + exponential functions for $IM^2_{p\pi^-}$ bin 1.30 – 1.31 ((GeV/c^2)^2). 110

Figure B.15 Background subtracted kaon-mass histogram for the exclusive analysis, fitted with Gaussian + exponential functions for $IM^2_{p\pi^-}$ bin 1.31 – 1.32 ((GeV/c^2)^2). 111

Figure B.16 Background subtracted kaon-mass histogram for the exclusive analysis, fitted with Gaussian + exponential functions for $IM^2_{p\pi^-}$ bin 1.32 – 1.33 ((GeV/c^2)^2). 112

Figure B.17 Background subtracted kaon-mass histogram for the exclusive analysis, fitted with Gaussian + exponential functions for $IM^2_{p\pi^-}$ bin 1.33 – 1.34 ((GeV/c^2)^2). 113

Figure B.18 Background subtracted kaon-mass histogram for the exclusive analysis, fitted with Gaussian + exponential functions for $IM^2_{p\pi^-}$ bin 1.34 – 1.35 ((GeV/c^2)^2). 114

Figure B.19 Background subtracted kaon-mass histogram for the exclusive analysis, fitted with Gaussian + exponential functions for $IM^2_{p\pi^-}$ bin 1.35 – 1.36 ((GeV/c^2)^2). 115

Figure B.20 Background subtracted kaon-mass histogram for the exclusive analysis, fitted with Gaussian + exponential functions for $IM^2_{p\pi^-}$ bin 1.36 – 1.37 ((GeV/c^2)^2). 116

Figure B.21 Background subtracted kaon-mass histogram for the exclusive analysis, fitted with Gaussian + exponential functions for $IM^2_{p\pi^-}$ bin 1.37 – 1.38 ((GeV/c^2)^2). 117

Figure B.22 Background subtracted kaon-mass histogram for the exclusive analysis, fitted with Gaussian + exponential functions for $IM^2_{p\pi^-}$ bin 1.38 – 1.39 ((GeV/c^2)^2). 118

Figure B.23 Background subtracted kaon-mass histogram for the exclusive analysis, fitted with Gaussian + exponential functions for $IM^2_{p\pi^-}$ bin 1.39 – 1.40 ((GeV/c^2)^2). 119

Figure B.24 Background subtracted kaon-mass histogram for the exclusive analysis, fitted with Gaussian + exponential functions for $IM^2_{p\pi^-}$ bin 1.40 – 1.41 ((GeV/c^2)^2). 120

Figure B.25 Background subtracted kaon-mass histogram for the exclusive analysis, fitted with Gaussian + exponential functions for $IM^2_{p\pi^-}$ bin 1.41 – 1.42 ((GeV/c^2)^2). 121

Figure B.26 Background subtracted kaon-mass histogram for the exclusive analysis, fitted with Gaussian + exponential functions for $IM^2_{p\pi^-}$ bin 1.42 – 1.43 ((GeV/c^2)^2). 122

Figure B.27 Background subtracted kaon-mass histogram for the exclusive analysis, fitted with Gaussian + exponential functions for $IM^2_{p\pi^-}$ bin 1.43 – 1.44 ((GeV/c^2)^2). 123

Figure B.28 Background subtracted kaon-mass histogram for the exclusive analysis, fitted with Gaussian + exponential functions for $IM^2_{p\pi^-}$ bin 1.44 – 1.45 ((GeV/c^2)^2). 124

Chapter 1

Introduction

The hyperon-nucleon (YN) and hyperon-deuteron(Yd) interactions are fundamental for studies in both nuclear physics and astrophysics. These are mainly focused on gaining a better understanding of the composition of the core of neutron stars and resolving the neutron-star hyperon puzzle as well as on building a comprehensive model of the baryon-baryon interaction. A neutron star is a compact but massive object containing neutrons as the primary particle. The Pauli pressure of the nucleons increases when the mass of the neutron star increases and the inbuilt pressure could be released by transforming neutrons to hyperons [1] [2]. Hyperons are baryons that contain strange quarks. Examples include $\Lambda(uds), \Sigma(uus$ or uds or $dds)$, $\Xi(uss$ or $dss)$, and $\Omega^{-}(sss)$ particles. Theoretical work suggests that hyperons should be present in the core of a neutron star, however astrophysical observations of neutron stars with masses larger than two solar masses cannot be explained by current predictions that use state-of-the-art hyperon-nucleon interaction in the equation of state of neutron star matter. The calculations predict lower star masses than observed. This discrepancy is known as the "hyperon puzzle" in strangeness physics. To resolve the "hyperon puzzle", significant experimental efforts have been invested in improving the precision of the lower-energy constants of the hyperon-nucleon potentials by means of providing high-precision scattering and hypernuclear data.

The scarcity of hyperon-nucleon and hyperon-deuteron elastic scattering measurements and availability of elastic scattering cross sections has been a challenge to this field of research [3]. The main reason for this situation is that hyperons are

unstable particles with relatively short lifetimes before decaying into other particles through the weak interaction. Thus, the preparation of hyperon beams is very difficult, whereas hyperon targets do not exist. To overcome these challenges, scientists use techniques such as secondary scattering in the same target cell while exploiting or designing high-statistics accelerator-based experiments.

In response to the needs described above, new YN and Yd programs have been initiated by the CLAS Collaboration using data taken with the CLAS detector in large photoproduction experiments. In these experiments, a real photon beam is incident on a proton (or a deuteron) target cell and photoproduces a Λ hyperon in a first step. In a second step, the Λ scatters elastically off another proton (or a deuteron) in the same target cell. Λp elastic cross sections demonstrating the technique for the CLAS data have been recently published [2]. Λd elastic yields have been extracted at the University of South Carolina (USC), whereas an exploratory study of the reaction $\Lambda d \to \Lambda pn$ ongoing as of the time of writing of this thesis.

The method of secondary scattering has been also used in the J-PARC E40 Σp scattering experiment. As a solution to the shortage of hyperon beams, $\Sigma^{\pm}$ beam was produced using the $\pi^{\pm} p \to K^{+}\Sigma^{\pm}$ reaction and then targeted on a liquid hydrogen (LH_2) target. In both Σ production and Σp scattering ($\Sigma p \to \Sigma p$), Σp elastic scattering events were identified kinematically by measuring 3-momentum vectors of the $\pi^{\pm}$ beam, the K^{+}, the recoil proton, and the produced Σ. The momentum of the Σs was obtained using the momentum data of πs. The momentum of the K^{+} was obtained using the measurements of K1.8 beamline spectrometer and the KURAMA spectrometer. The momentum vector of the recoil proton was determined by the analysis of CATCH (Cylindrical Active Tracker and Calorimeter system for Hyperon-proton scattering) system [4].

In this project, $\gamma d \to \Lambda X$ signal was identified in the g13a data set for obtaining an estimate of the inclusive Λ photoproduction yield in bins of Λ scattering angle and Λ

momentum in the laboratory system. Symultaneously, we estimated the systematic error of the background subtraction used in the yield extraction by analyzing the exclusive reaction $\gamma d \to K^+ \Lambda n$. Our final result is the inclusive Λ yields and yield correction factor.

Chapter 2

Experiment and Experimental Setup

2.1 Overview

The data analyzed in this project were collected in the E06-103 (g13) experiment, which was conducted using the CLAS in Hall B at JLab.

The g13 experiment collected approximately 50 billion triggers over two distinct run periods, g13a and g13b. g13a and g13b made use of a circularly-polarized and a linearly-polarized real-photon beam, respectively. The real photon beams were produced when the electron beam delivered from the accelerator interacted with a radiator positioned in the Hall-B Tagger. The study presented here is based on the g13a data set, which contains 20 billion triggers and was conducted during October to December 2006 and March 2007. The photon beam energies ranged from 0.418 GeV to 1.895 GeV. The target was a 40-cm-long unpolarized liquid deuterium (LD_2) cell located 20 cm upstream from the center of the CLAS to enhance the acceptance for particles scattered at small polar angles. The data are portioned in 2-hour-long data subsets, referred to as runs. Table 2.1 gives detail about the times and electron-beam energies corresponding to the g13a runs.

The electron beam in Hall B was delivered by the Continuous Electron Beam Accelerator Facility (CEBAF) at JLab. The main objective of the laboratory has been to investigate the electromagnetic structure of mesons, nucleons, and nuclei using polarized electron and photon beams [5]. During the g13 experiment, CEBAF could deliver electrons with energies up to 6 GeV. An upgrade between 2013 and 2016

Table 2.1 List of the g13a runs according to the data taking period and electron beam energy. Experimental conditions were kept constant over three main run ranges.

Period	Electron beam energy	Run number
October 30 - November 21 2006	1.987 GeV	53164 – 53532
November 28 - December 22 2006	2.649 GeV	53538 – 53862
March 12 - March 15 2007	1.987 GeV	53998 – 54035

increased the maximum energy to 12 GeV [6]. CEBAF is a Superconducting Radio Frequency Linear Accelerator (SRF LINAC) with a recirculating configuration that allows for five passes. It was capable of simultaneous delivery of three beams to three end stations (Halls A, B, and C) during the 6-GeV era. These beams could reach up to 200 μA with up to 85% polarization. The accelerator maintained a geometric emittance of less than 10^{-9} m·rad and a relative momentum spread of only 10^{-5} GeV/c, ensuring high precision and stability during operation. The combination of a five-pass re-circulation design, three laser photo-cathode sources, and sub-harmonic RF separator-based extraction allowed for the simultaneous delivery of three beams at different energies. This configuration also enabled hall-to-hall current ratios approaching 10^6 while maintaining the specified orientation of the beam polarization [7].

The CLAS detector employed in Hall B was a nearly 4π detector, specifically designed for the examination of photo- and electro-induced nuclear and hadronic reactions with multiple charged-particle final states. The detector configuration consisted of six superconducting coils that generated a toroidal magnetic field with azimuthal symmetry around the beam axis and separated the CLAS into six independent mag-

netic spectrometers. The magnetic field allowed for the bending of charged particles in the θ (polar angle) direction while minimally affecting their ϕ (azimuthal angle) direction.

Tracking of charged particles was achieved by means of three regions of drift chambers (DC), consisting of a combined total of 18 axial and 16 stereo layers of drift cells. Tracks in DC, combined with the known magnetic field, allowed for the determination of the particle momentum, as well as the sign of the particle charge. Besides the drift chambers, the detector components relevant for this work are two scintillation detectors, the Start Counter (ST), and the Time-of-Flight Detector (TOF). The former was used to determine the start time of an event, whereas the latter provided the time of flight (tof) of charged particles [8]. Charged-particle identification in the CLAS was based on the tof technique. Figure 2.1 shows transverse and side cross-sections of the CLAS that visualize the main detector components.

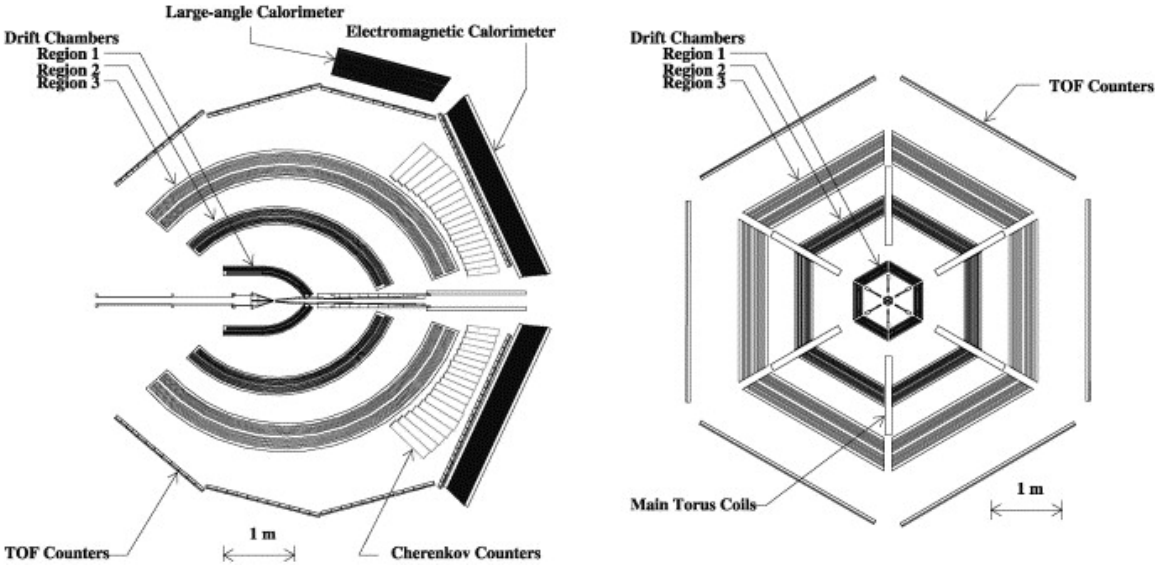

Figure 2.1 Schematic diagrams of the CLAS detector in Hall B. Left: side cross section. The beam is incident from left to right. Right: transverse cross section. The beam direction is into the page. In both schematics, one can see the three regions of drift chambers and the panels of TOF scintillator paddles. The Cherenkov counter and the electromagnetic calorimeters were not used in this analysis. The six-sector geometry can clearly be seen on the right figure.

Chapter 3

Data Analysis

3.1 Extraction of the Inclusive Λ Photoproduction Yield

This section describes our process of selecting $\gamma d \to \Lambda X$ inclusive events. The hyperon was reconstructed by means of its charge decay products, a proton and a π^-, so the data sample we are using contains at least one p and at least one π^- without any constraints on the number of neutral or other charged particles. The branching ratio of $\Lambda \to p\pi^-$ is well known and is $63.9 \pm 0.5\%$. The reason for using the $p\pi^-$ decay is due to the large CLAS acceptance for charged particles, whereas the acceptance for neutrals is very limited. We do not impose any constraints on the total number of charged particles and neutrals to accommodate for the fact that Λ can be produced in various nuclear reactions, such as $\gamma d \to \Lambda K^+ n$, $\gamma d \to K^0 \Lambda p$, $\gamma d \to \Sigma^0 K^+ n$ where Σ^0 decays to $\Lambda\gamma$, *etc.* The analysis has two main stages: particle identification and background subtraction.

3.1.1 Particle Identification (PID)

The PID method for charged particles with the CLAS is based on the tof technique, *i.e.*, particles with different masses but same momenta have different speeds. The method assumes that each particle moves with constant speed throughout the detector.

The relative speed of each charged particle is determined by the ratio

$$\beta_{measured} = \frac{l}{ct}, \tag{3.1}$$

where l and t is the traveled path length and the time of flight of the particle, respectively, from the vertex to the TOF detector, and c is the speed of light in vacuum. The tof technique is visualized in Fig. 3.1, which shows an event distribution of β versus p for charged particles.

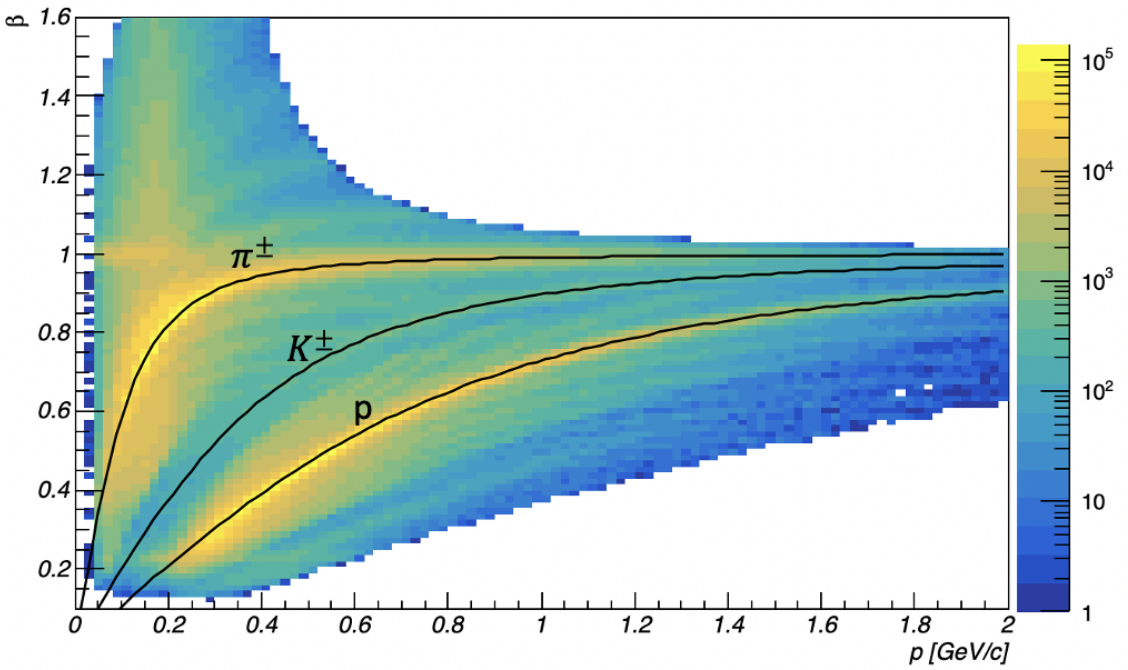

Figure 3.1 β versus p for charged particles. One clearly sees pions, kaons, and protons.

In this work, the tof technique was applied by assessing the difference between the measured relative speed of each particle and the one calculated using the measured momentum, p, and a hypothesis for the nominal particle mass, m. The calculated speed was determined using the definition of relativistic momentum as

$$\beta_{calculated} = \frac{p}{\sqrt{p^2 + m^2}}, \tag{3.2}$$

whereas the difference between $\beta_{measured}$ and $\beta_{calculated}$ was determined as

$$\Delta\beta = \beta_{measured} - \beta_{calculated}. \tag{3.3}$$

In the above equations, and throughout the rest of the thesis, we work in a system where $c = 1$.

Four mass hypotheses were tested for each positively-charged track: pion, kaon, proton, and deuteron, reflecting the most common positively charged particles detected with the CLAS at the energies of the experiment. Only two hypotheses were tested for each negatively-charged track: pion and kaon, due to the visible lack of anti-protons and anti-deuterons.

The event distribution over $\Delta\beta$ is expected to be consistent with zero, within the detector resolution, when the nominal mass in Eq. 3.2 is the true mass of the particle. From all mass hypotheses, the mass yielding a difference consistent with zero, within the detector resolutions, was assigned to the particle.

Figure 3.2 demonstrates our method by showing the $\Delta\beta$ versus p distribution for the positively-charged tracks with a proton hypothesis. True in-time proton tracks have $\Delta\beta$ consistent with zero throughout the full momentum range. All tracks with $\Delta\beta$ values falling between the red solid lines were identified as protons and selected for further analysis. The red solid lines are two third order polynomial functions $f_{top} = -0.0181x^3 + 0.0652x^2 - 0.0684x + 0.0437$ and $f_{bottom} = 0.0344x^3 - 0.1121x^2 + 0.1193x - 0.0691$, showing the lower and the upper cuts we applied. These were determined in a previous analysis [9] by dividing the momentum range into sub-ranges and fitting the $\Delta\beta$ distribution in each sub-range to a Gaussian. The standard deviation of each fit was used to calculate the lower and upper $\Delta\beta$ cuts for those bins. The functions allow for a momentum-dependent selection cuts, reflecting the fact that detector resolutions depend on particle momentum.

The π^-s were selected by applying a wide $\Delta\beta$ cut in the range of -0.2 to $+0.2$, as shown in Fig. 3.3. The cut was established in [9] and its width reflects the fact that the pions from the Λ decay are predominantly low-momentum particles yielding a wide $\Delta\beta$ distribution at low momenta and the wide cut allows not to exclude good

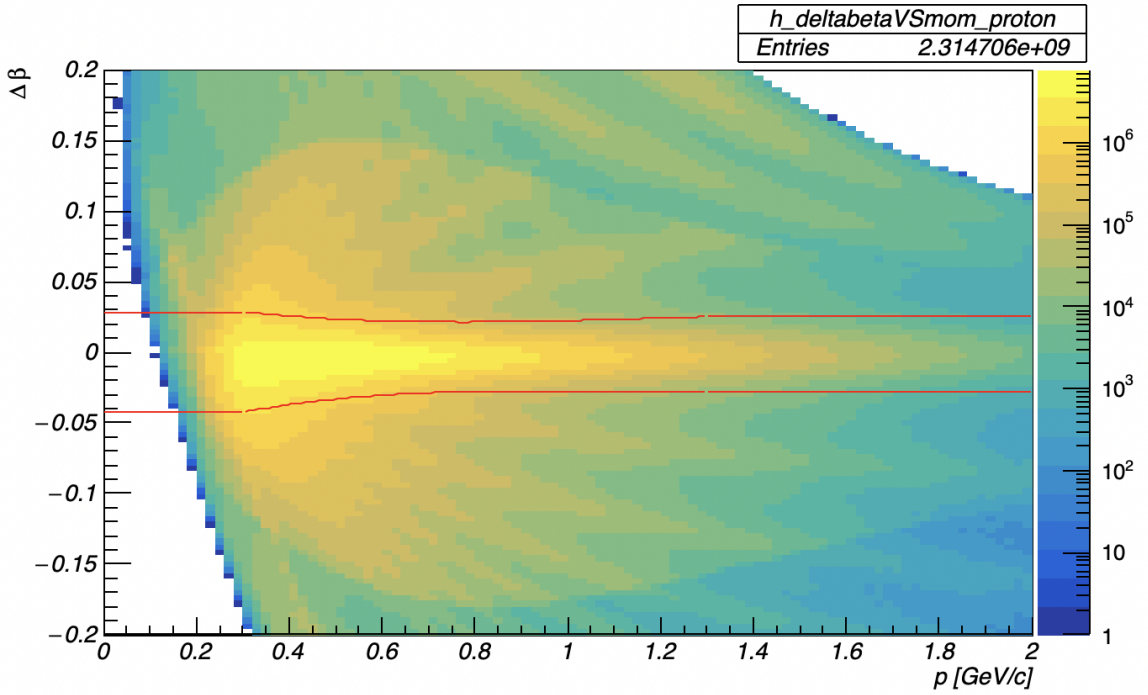

Figure 3.2 $\Delta\beta$ versus p for positively-charged tracks assuming proton nominal mass. The red solid lines show our cut selecting protons for further analysis. The cuts were determined in a previous analysis [9]. Out of time protons populate the "wings" emanating from the true proton distribution at low momentum. Particles not consistent with the proton hypothesis show up in structures, such as the ones in the upper right area.

π^-.

3.1.2 Selection Cuts

After selecting events with at least one proton and at least one π^-, further cuts were applied to reduce contributions from background events.

Vertex cut: While the scattered Λ could have decayed outside of the target, the reconstruction of a particle 3-momentum vector from hits in the drift chambers extrapolates the track back to the beam line in order to determine the particle direction at the vertex and the vertex components. While more precise methods for the determination of the Λ decay vertex have been previously applied to hyperon analy-

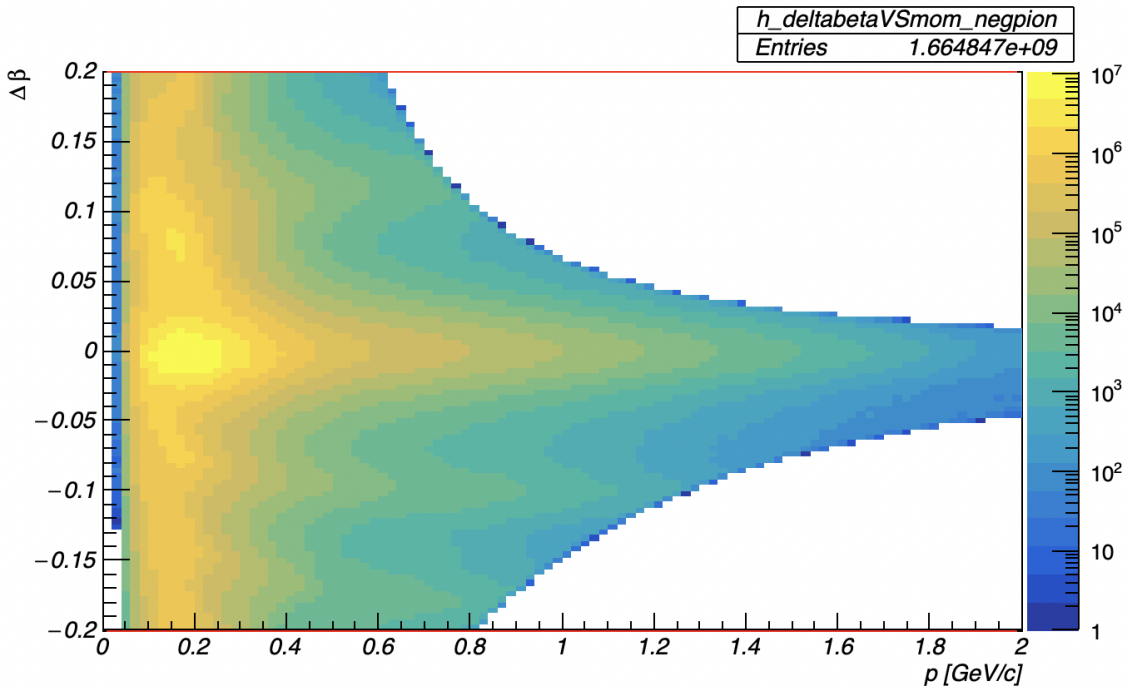

Figure 3.3 $\Delta\beta$ versus p for negatively-charged tracks assuming π^- nominal mass. One can see the effect of a wide selection cut applied on the reconstructed particle mass at a pre-processing stage that was not part of this work.

ses, those are beyond the scope of this work. Here, we eliminate events in which the z-vertex component of either the pion or the proton track falls outside of the target. The vertex position along the Z axis was measured relative to the center of the CLAS, which is located at 0 cm. The cut covers the physical length of the target and its most important effect is to filter out events originating from a non-target material located at $z = 7$ cm along the beam line. The z-vertex distributions and our selection cuts are shown in Fig. 3.4 for both, positively and negatively-charged tracks.

Selection of the good photon: For each event detected in the CLAS, the photon tagger registers more than one electron that has radiated a bremsstrahlung photon. The main reason for this effect is the length of the readout window of detector electronics that is much longer than the 2.004-ns interval between neighboring electron beam bunches. Thus, while the CLAS detects the particles originating from the

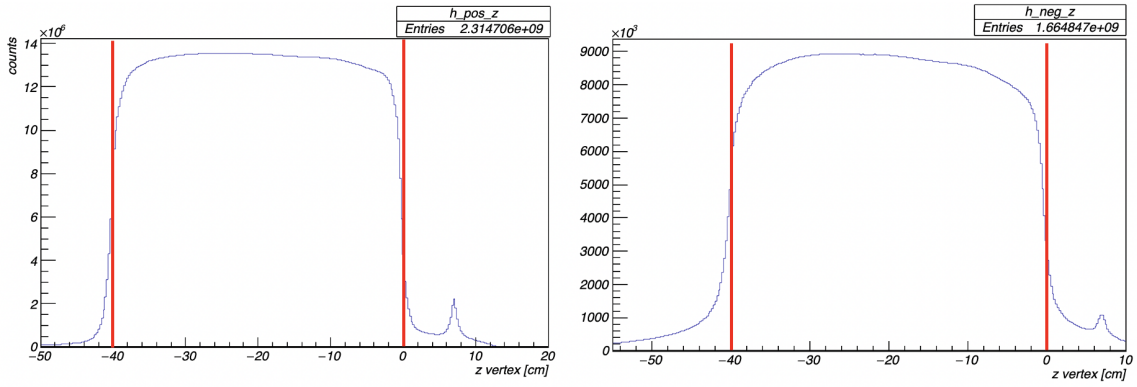

Figure 3.4 Left: z component of the production vertex of positively charged particles. Right: z component of the production vertex of negatively charged particles. The solid red lines show the cuts applied in this work.

interaction of one photon with the target nucleus, the number of tagged photons per event is larger than one (on average 14 for g13a) and a selection procedure identifying the photon, which initiated the CLAS event (good photon) needs to be applied. The good photon was determined by comparing the photon arrival time at the production vertex ($t_{v,\gamma}$) and the vertex time of the fastest track detected in the CLAS for that event ($t_{v,scfasteststrack}$). The fastest track was chosen as it has the lowest error in the vertex time due to the lowest energy loss. $t_{v,\gamma}$ is calculated as:

$$t_{v,\gamma} = t_{CLAScenter} + \frac{(z+20)}{c}, \tag{3.4}$$

where z is the component of the production vertex along the beam axis, $t_{CLAScenter}$ is the photon arrival time at the center of the CLAS (typically returned by the CLAS reconstruction procedures), and the 20-cm shift was included as the center of the target was located at 20 cm upstream of the CLAS center in the g13 experiment. $t_{v,scfasteststrack}$ was calculated from measured TOF timing. The notation sc is used to denote quantities measured by the TOF detector (as compared to those measured by ST).

$$t_{v,scfasteststrack} = t_{scfasteststrack} - \frac{d_{scfasteststrack}}{c\beta_{measuredfasteststrack}}, \tag{3.5}$$

where $t_{scfastesttrack}$ is the time it takes the fastest particle to travel from the vertex to the TOF detector, measured relative to the reference time for the event (trigger time), $d_{scfastesttrack}$ is the distance the fastest particle travels from the vertex to the TOF detector, and $\beta_{measuredfastesttrack}$ is the speed of the particle.

The coincidence time between each photon and the fastest track is then formed as the vertex time difference (Δt)

$$\Delta t = t_{v,\gamma} - t_{v,scfastesttrack} \tag{3.6}$$

Figure 3.5 shows the event distribution over Δt. The 2.004-ns electron-beam bunch separation is clearly visible. The good photon was selected to be the photon with the smallest vertex time difference in the range of ± 1 ns.

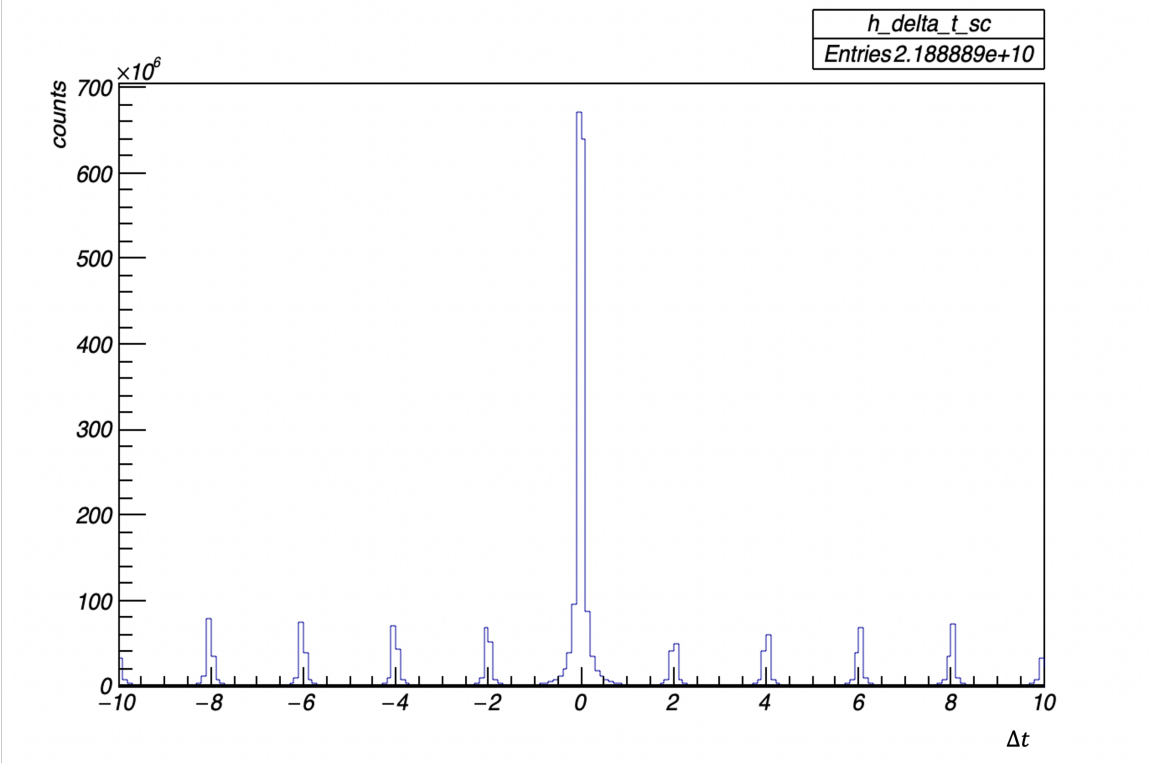

Figure 3.5 Vertex time difference distribution using TOF timing. The coincidences between the tracks in the CLAS and the tagged photons are in the peak centered at zero. Photons from different electron beam bunches show in the smaller peaks that are 2.004-ns apart.

3.1.3 Reaction Selection

In the data sample obtained after all the cuts described above were applied, not all proton and π^- pairs originated from a Λ decay. To identify those that did, 4-momentum conservation was applied at the Λ decay vertex, the Λ 4-vector was reconstructed, and its square, referred here as the invariant mass squared of $p\pi^-$, $IM_{p\pi^-}{}^2$, was determined,

$$IM_{p\pi^-}{}^2 = (\tilde{P}_p + \tilde{P_{\pi^-}})^2, \tag{3.7}$$

where $\tilde{P}_p$ and $\tilde{P_{\pi^-}}$ are the 4-vectors of the proton and the pion, respectively. The square-root value of this quantity gives $IM_{p\pi^-}$. For events with more than one proton or more than one pion, one could not determine on event-by-event basis which $p\pi^-$ pair originated from a Λ decay. Thus, the $IM_{p\pi^-}$ was calculated for each possible pair combination.

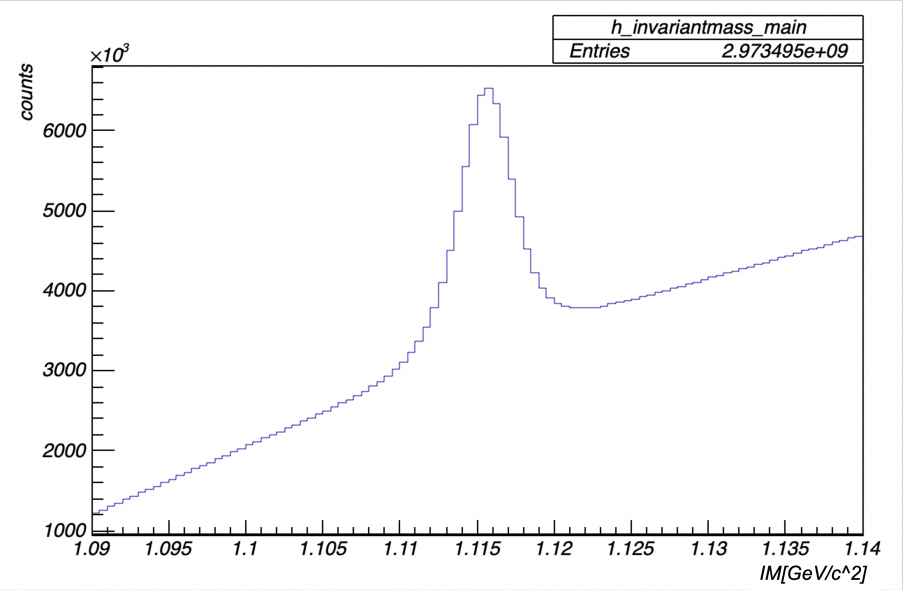

Figure 3.6 $IM_{p\pi^-}$ for each possible $p\pi^-$ pair combination. One can see the ΛX events in the peak centered at the nominal Λ mass.

3.1.4 Binning

For each $p\pi^-$ combination, the momentum p_Λ and the polar angle θ_Λ in laboratory frame were determined. Figure 3.7 shows the event distribution over θ_Λ versus p_Λ to visualize the data coverage in both quantities. One can see that most of the Λs produced at angles below 1 rad. This is due to the fact that the inclusive yield is dominated by the exclusive reactions $\gamma d \to K^+\Lambda n$ and $\gamma d \to K^0\Lambda p$, which are characterized with a maximum θ_Λ of about $50° - 60°$.

We binned the data sample in intervals of 0.1 rad in θ_Λ and 0.1 GeV/c in p_Λ and determined the inclusive yield for each such bin.

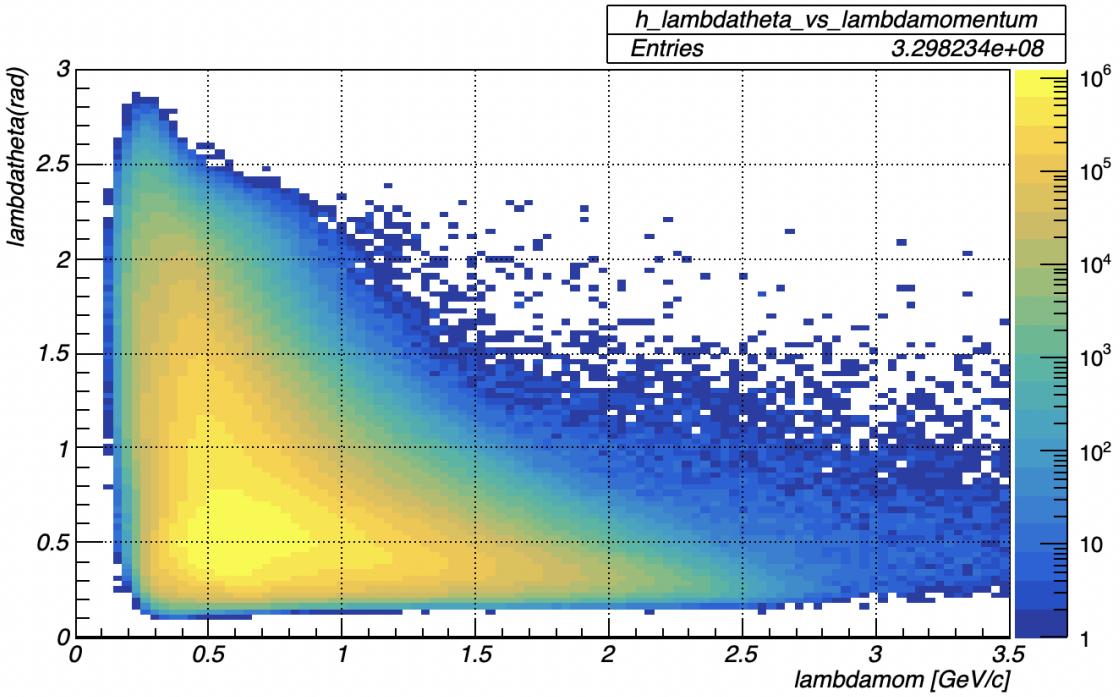

Figure 3.7 θ_Λ versus p_Λ.

3.1.5 Yield Extraction

Figure 3.8 shows the $IM_{p\pi^-}$ distribution for one representative $(p_\Lambda, \theta_\Lambda)$ bin and demonstrates our background subtraction technique.

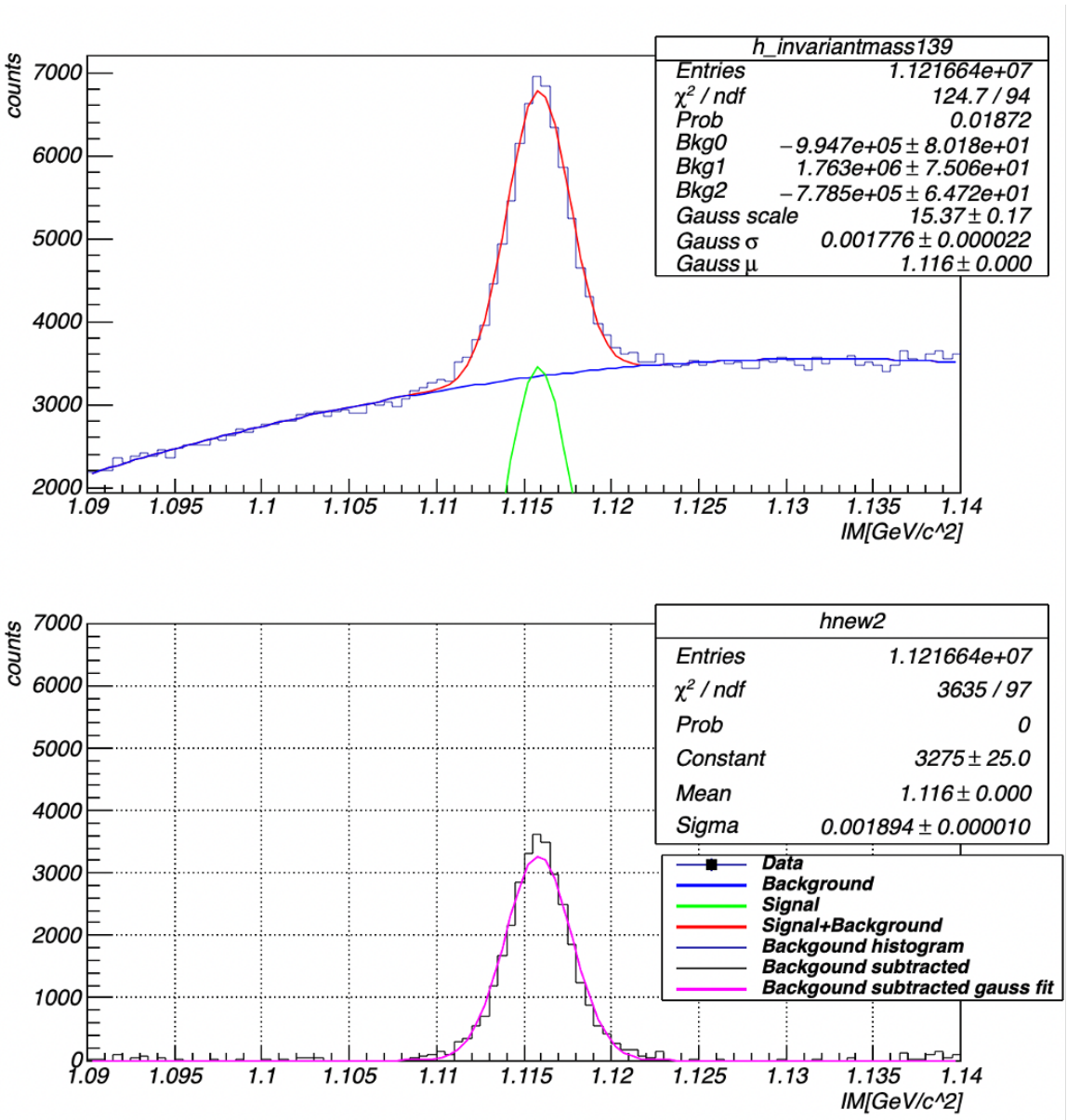

Figure 3.8 Top: $IM_{p\pi^-}$ distribution fitted with a sum of a Gaussian and a second-order polynomial for the bin of $1.3 < p_\Lambda < 1.4$ GeV/c and $0.6 < \theta_\Lambda < 0.7$ rad. Bottom: Background-subtracted histogram obtained by subtracting the fitted polynomial from the $IM_{p\pi^-}$ distribution.

The $IM_{p\pi^-}$ distribution for every bin $(p_\Lambda, \theta_\Lambda)$ was fitted to a sum of a Gaussian and a second-order polynomial. While we also tested an exponential shape for the background, we were able to get best fitting results from fitting the background with second order polynomial function. The objective of this fit was to obtain as

good description of the background as possible. Since we did not have an accurate description of the shape of the Λ peak in the $IM_{p\pi^-}$ distribution, we assumed that it was a simple Gaussian for all the bins.

For each $(p_\Lambda, \theta_\Lambda)$ bin, the inclusive yield was then obtained as

$$N_\Lambda = N_{AllIM} - N_{Background_{IM}}, \tag{3.8}$$

where N_Λ is the number of events in the background-subtracted histogram within the range of 1.105 GeV/c^2 and 1.125 GeV/c^2, N_{AllIM} is the number of events in the background-unsubtracted histogram within the same range, and $N_{Background_{IM}}$ is the number of events under the background function within the same range. The range within which we counted the number of events, is about $\pm 4\sigma$ from the peak position as determined by a Gaussian fit to the backrgound subtracted IM distribution. The uncertainty of the number of Λ events, σ_{N_Λ}, was calculated as

$$\sigma_{N_\Lambda} = \sqrt{N_{AllIM} + N_{Background_{IM}}}, \tag{3.9}$$

using uncertainty propagation and assuming that N_{AllIM} and $N_{Background_{IM}}$ are not correlated.

To monitor how the position and the width of the background-subtracted Λ peak varies we fitted it with a Gaussian for every $(p_\Lambda, \theta_\Lambda)$ bin.

3.2 Exclusive Analysis

Previous analyses of g13 data selecting final states with at least one Λ have shown that the $IM_{p\pi^-}$ does not have a simple Gaussian shape. While the bulk of the peak can be described by a single Gaussian, that Gaussian sits on top of long non-Gaussian tails. Describing accurately these tails have proven to be very difficult. Thus, while we made the concious decision to perform a background subtraction assuming a Gaussian shape for the Λ peak, we also undertook a dedicated analysis to quantify the error caused by this assumption.

In this analysis, we selected a sample of $\gamma d \to \Lambda K^+ n$ events. In this exclusive reaction, the hyperon is tagged by a K^+ meson, which not only reduces the background, but allows to quantify the number of $K^+\Lambda$ events over a wide range of $IM_{p\pi^-}$. This reaction was chosen among all other exclusive reactions with a Λ in the final state as it has the smallest number of detected charged particles and the highest statistics. Below, we describe our study in details.

3.2.1 Particle Identification and Selection Cuts

We started with an event sample containing exactly three charged tracks, of which two were positively-charged and one was negatively charged. No constrains on the neutrals were made. Following the same steps as in our inclusive ΛX analysis, the final-state particles were identified using information about momentum and time of flight. $\Delta\beta$ for each charged track was determined using the difference between $\beta_{measured}$ and $\beta_{calculated}$. As mentioned, previously, the event distribution over $\Delta\beta$ is centered at zero, when the nominal mass in $\beta_{calculated}$ is the true mass of the particle. Figures 3.9, 3.10, and 3.11, show event distributions of $\Delta\beta$ versus p for proton, π^-, and K^+ hypotheses, respectively. The $\Delta\beta$ cuts for positively-charged tracks from [9] were applied here (shown by solid red lines in Fig. 3.9 and Fig. 3.11) to select the proton and K^+. As in the case of the proton, the kaon $\Delta\beta$ cuts are two third-order polynomial functions $f_{top} = -0.0022x^3 + 0.0084x^2 - 0.0091x + 0.0343$ and $f_{bottom} = -0.0067x^3 + 0.0180x^2 - 0.0118x - 0.0316$. The π^-s were selected by applying the same $\Delta\beta$ cut as in our inclusive analysis.

After identifying the charged particles in the final state of $\gamma d \to \Lambda K^+ X$ reaction, we then selected events that originated within the target. Figure 3.12 shows the z-vertex distributions of the positively- and negatively- charged tracks, as well as the cuts we applied to reduce the amount of background events that did not originate in the target cell.

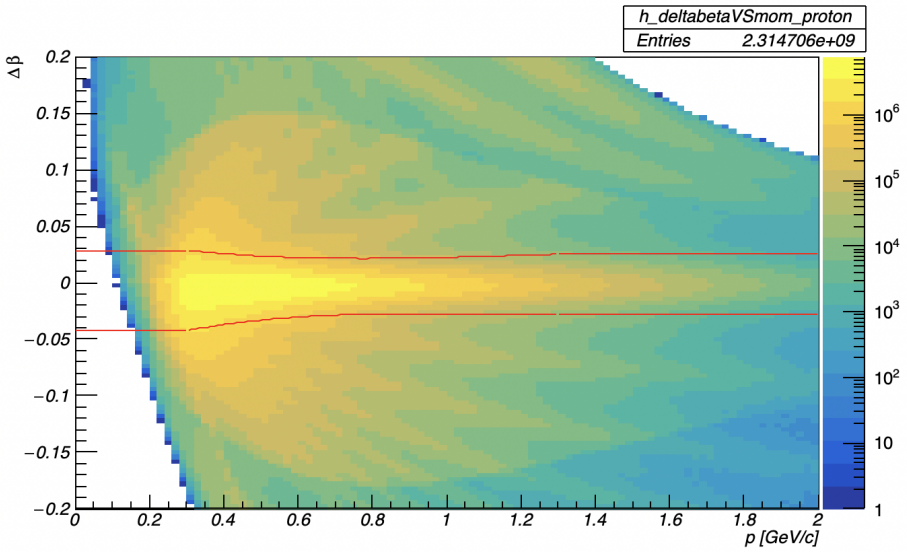

Figure 3.9 $\Delta\beta$ versus p for positively-charged tracks assuming proton nominal mass.

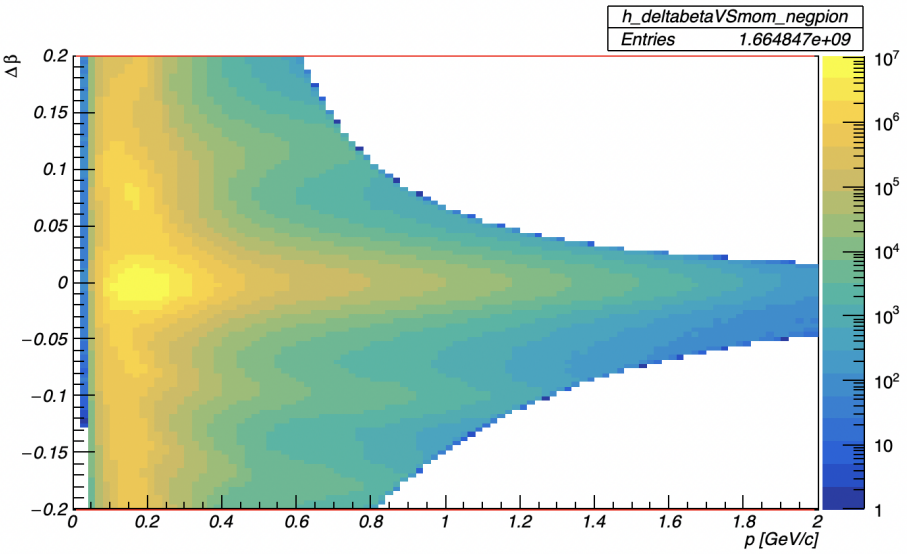

Figure 3.10 $\Delta\beta$ versus p for negatively-charged tracks assuming π^- nominal mass.

In the next analysis step, we selected the good photon by applying the same procedure as described in Sec. 3.1. Events with exactly one good photon within ± 1 ns were used for further studies. Events with more than one good photon were discarded.

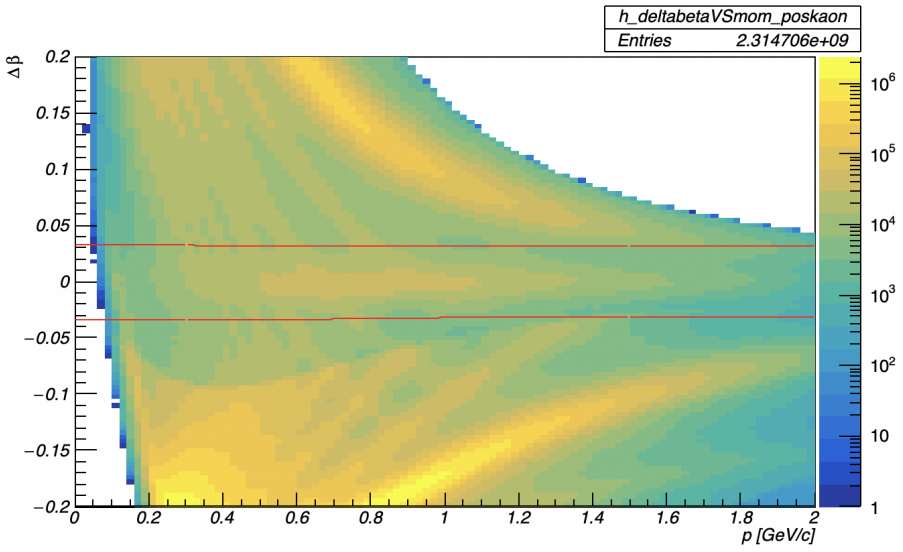

Figure 3.11 $\Delta\beta$ versus p for positively-charged tracks assuming K^+ nominal mass.

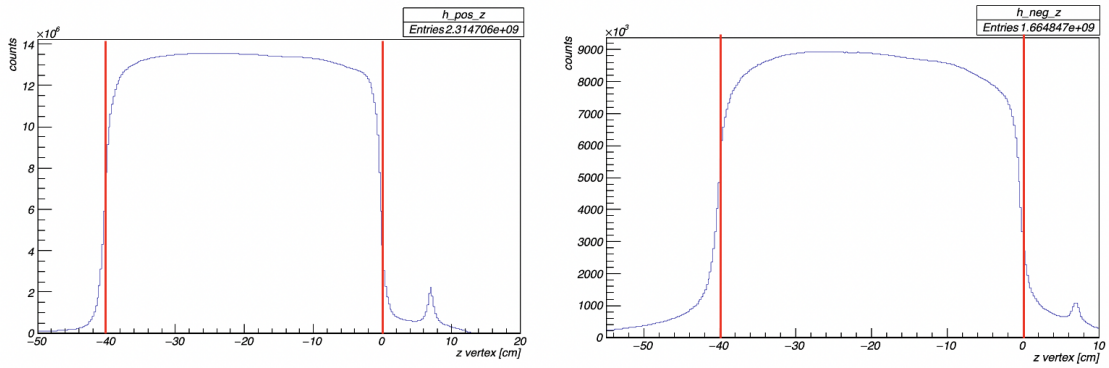

Figure 3.12 Left: z component of the production vertex of positively charged particles. Right: z component of the production vertex of negatively charged particles. The solid vertical lines denote the cuts applied to reduce background in the data sample.

3.2.2 Kinematic cuts

In the next step, we determined the square of the mass M_X of the state X in the $\gamma d \to \Lambda K^+ X$ reaction using four-momentum conservation

$$M_X{}^2 \equiv MM^2 \equiv MM^2_{K^+\Lambda X} = \tilde{P}^2_X = (\tilde{P}_\gamma + \tilde{P}_d - \tilde{P}_p - \tilde{P}_{\pi^-} - \tilde{P}_{K^+})^2. \qquad (3.10)$$

Assigning the true particle mass to each track, the total energy of the particle was calculated and its four-momentum vector ($\tilde{P}$) was formed. $\gamma d \to \Lambda K^+ n$ events would be contained in a peak at the nominal neutron mass of the event distribution over M_X (or M_X^2).

Veto cut

In the particle identification, K^+s were selected by applying a $\Delta\beta$ cut (see Fig. 3.11). Due to finite detector resolutions, the proximity of the kaon mass to the pion and the proton masses, and the large number of pions and protons, compared to kaons, there can be misidentified protons and π^+s in the K^+ sample. To reduce the amount of those misidentified positively-charged particles, we tested whether our events originated in the exclusive reactions $\gamma d \to pp\pi^-$ and $\gamma d \to \pi^+ p\pi^- n$, which are the highest-cross-section processes that could contaminate our event sample with protons and pions, respectively, in the kaon track. By applying four-momentum conservation, for each $\Lambda K^+ X$ event, we determined two other kinematic quantities, ${MM_{p\pi^+\pi^-}}^2$ and ${MM_{pp\pi^-}}^2$, assuming the K^+ track was a π^+ and a proton, respectively

$${MM_{p\pi^+\pi^-}}^2 = (\tilde{P}_\gamma + \tilde{P}_d - \tilde{P}_p - \tilde{P}_{\pi^-} - \tilde{P}_{\pi^+})^2, \tag{3.11}$$

$${MM_{pp\pi^-}}^2 = (\tilde{P}_\gamma + \tilde{P}_d - \tilde{P}_p - \tilde{P}_{\pi^-} - \tilde{P}_p)^2. \tag{3.12}$$

The left panel of Fig. 3.13 shows the event distribution of $MM^2_{K^+\Lambda X}$ versus $MM^2_{pp\pi^-}$. One can clearly see the true $\Lambda K^+ n$ events clustering at the nominal neutron mass squared on the Y axis (a horizontal band around 0.8827 $(\mathrm{GeV}/c^2)^2$). One can also see true $pp\pi^-$ events clustering at a mass of zero on the X axis (a vertical band at 0 $(\mathrm{GeV}/c^2)^2$). Due to finite detector resolutions, the two bands cross each other, which made it complicated to devise a cut that would exclude $pp\pi^-$ events, so we did not apply any.

The right panel of Fig. 3.13 shows the event distribution of $MM^2_{K^+\Lambda X}$ versus $MM^2_{p\pi^+\pi^-}$. One can clearly see $p\pi^+\pi^- n$ events clustered around the square of the

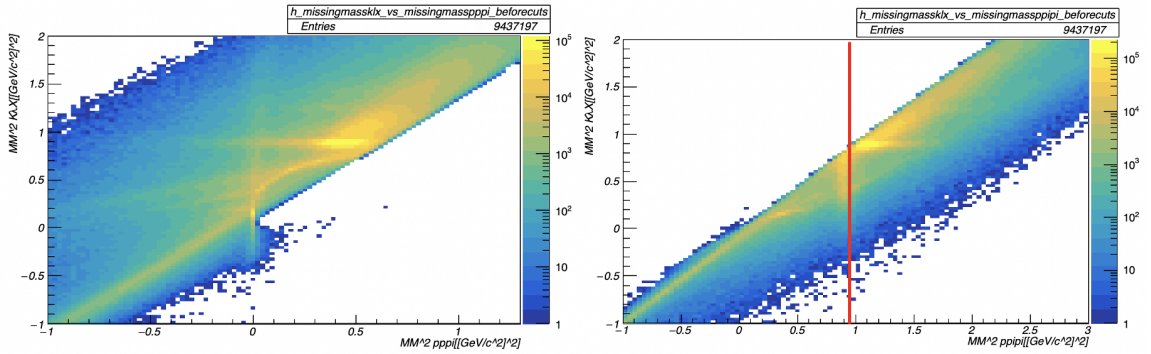

Figure 3.13 Left:$MM_{K^+\Lambda X}{}^2$ versus $MM_{pp\pi^-}{}^2$. Right:$MM_{K^+\Lambda X}{}^2$ versus $MM_{p\pi^+\pi^-}{}^2$.

neutron mass on the X axis (a vertical band at 0.8827 $(\mathrm{GeV}/c^2)^2$). One can also see the true $\Lambda K^+ n$ events clustering at the nominal neutron mass squared on the Y axis (a horizontal band around 0.8827 $(\mathrm{GeV}/c^2)^2$). While the two bands overlap somewhat, the separation between the two sets of events is sufficient to apply a cut on $MM^2_{p\pi^+\pi^-}$, as shown by the solid vertical line. This cut reduced significantly the pion contamination in the kaon sample, while it did not exclude good $\Lambda K^+ n$. We will refer to this cut as a veto cut. It removes events with $MM_{p\pi^+\pi^-}{}^2 < 0.93$ $(\mathrm{GeV}/c^2)^2$.

Photon energy cut

Since the exclusive reaction of interest requires a minimum photon beam energy in order to take place, we applied a minimum cut on the energy of the good photon in order to reduce background contributions. Figure 3.14 shows the energy of the good photon versus MM^2. One sees that there are no good $K^+\Lambda n$ events produced by photons with energies below ~ 0.85 GeV. The photon energy cut was chosen based on the event distribution shown in Fig. 3.14. The exact threshold photon energy value obtained from kinematic calculations [9] is

$$E_{\gamma,threshold} = \frac{(m_{K^+} + m_\Lambda)^2 - {m_p}^2}{2m_p} = 0.911 \text{ GeV}. \tag{3.13}$$

Here, m_{K^+}, m_Λ, and m_p are the nominal masses of the K^+, Λ, and proton, respectively.

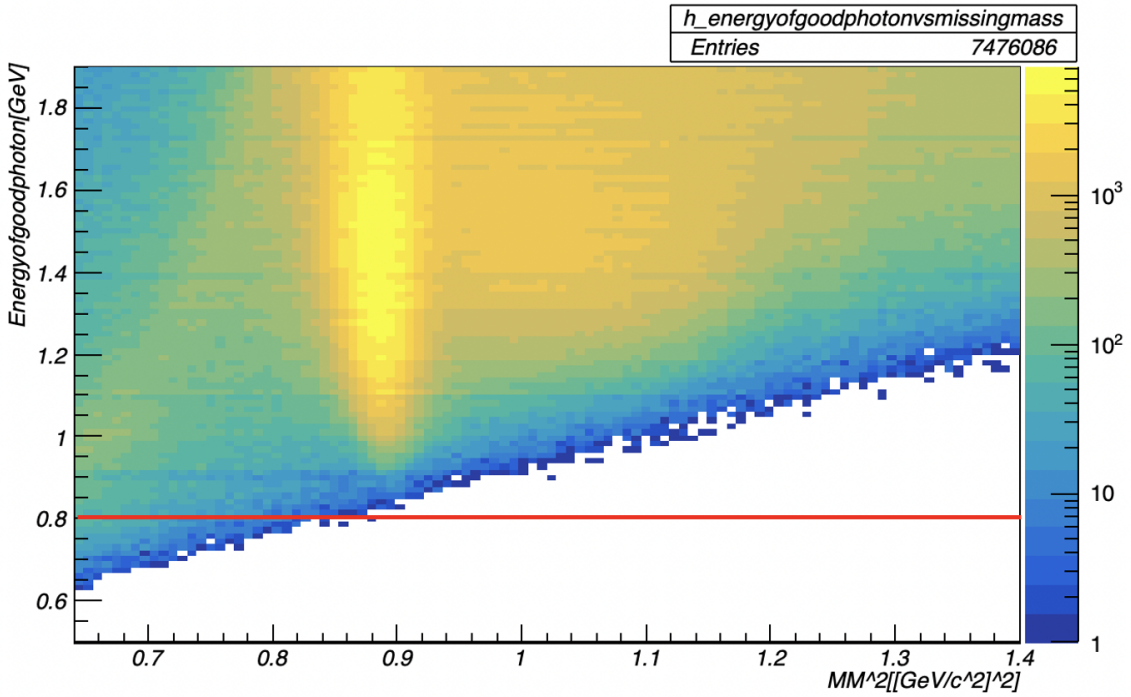

Figure 3.14 $E_{\gamma good}$ versus ${MM_{K^+\Lambda X}}^2$ distribution after PID, z-vertex, photon selection, and veto cuts.

We apply a conservative cut at 0.8 GeV. It removes a fraction of the background at lower missing masses. Remaining accidental background can be seen in the existence of lower missing-mass events. At missing masses higher than the neutron mass squared, physics background events from other reactions with more missing particles are seen.

$IM_{p\pi^-}$ CUT

Similarly to our inclusive analysis, we formed the invariant mass squared of proton and π^-, $IM^2_{p\pi^-}$, in order to select those events where the pair originated from a decay of Λ. Here also true Λ events would form a narrow peak centered at the Λ nominal mass squared value of 1.2445 $(\mathrm{GeV}/c^2)^2$. Due to the narrowness of the Λ peak, events with $IM^2_{p\pi^-} < 1.15$ $(\mathrm{GeV}/c^2)^2$ and $IM^2_{p\pi^-} > 1.5$ $(\mathrm{GeV}/c^2)^2$ were removed from further analysis.

After all of the above cuts, the $IM^2_{p\pi^-}$ versus ${MM_{K^+\Lambda X}}^2$ distribution was observed to assess the widths and the tails of the Λ and neutron peaks, respectively. The

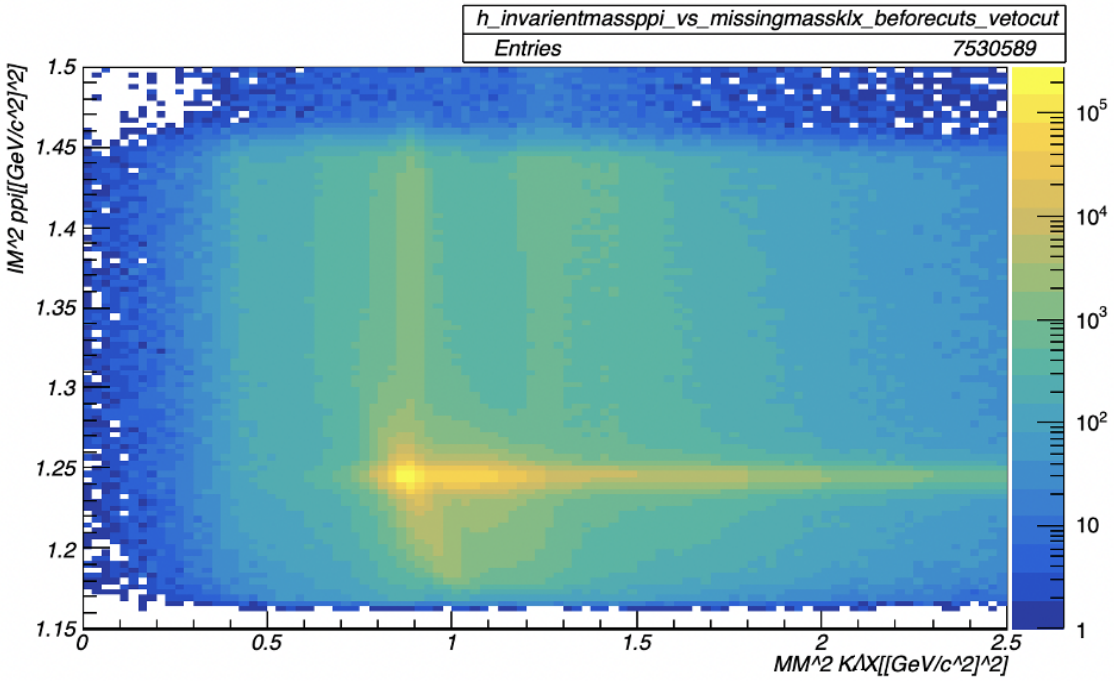

Figure 3.15 $IM^2_{p\pi^-}$ versus ${MM_{K^+\Lambda X}}^2$ distribution after PID, z-vertex, and veto cuts.

good events in the $IM^2_{p\pi^-}$ distribution were distributed over the range of [1.17, 1.45] $(\mathrm{GeV}/c^2)^2$ and events within this region were used for our further analysis with the concern of not removing any true Λ events from data set.

Missing mass cut

After applying PID, z-vertex, photon selection, veto, and E_γ cuts, further background reduction was achieved by the application of a cut on the ${MM_{K^+\Lambda X}}^2$ distribution as shown in Fig. 3.16 The cut range [0.82,0.94] $(\mathrm{GeV}/c^2)^2$ is the same as in [9]. It is interesting to note that the neutron peak is located at 0.8827 $(\mathrm{GeV}/c^2)^2$, which is the nominal mass squared value of neutron. The cut is not symmetric around the peak in order to remove as much physics background as possible while not removing many

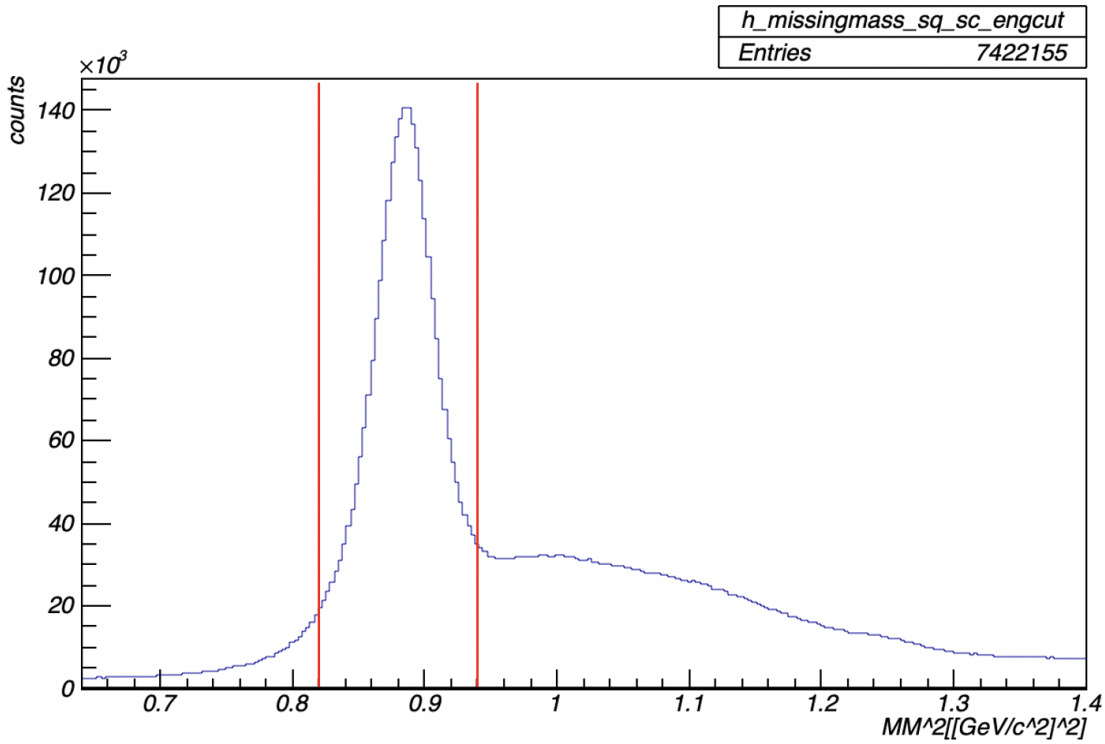

Figure 3.16 $MM_{K^+\Lambda X}{}^2$ distribution after PID, z vertex, photon selection, veto, $IM^2_{p\pi^-}$, and $E_{\gamma good}$ cuts.

good events at lower missing masses. It is clear that within the missing-mass cut range, there are background events. Based on the prior extensive experience of the USC group with the exclusive analysis, we already know that accidental background due to misidentified particles is the main contributor at lower missing masses. Most of the background at higher missing masses is physics background due to extra missing particle(s). The physics background, however, still contains true $K^+\Lambda$ events. As our target is to find the true shape of $IM^2_{p\pi^-}$ Λ peak, we are not concerned with the physics background events as they would not affect our study, but only with the accidental background.

After applying all of the above selection cuts, we assessed again the $IM^2_{p\pi^-}$ versus $MM_{pp\pi^-}{}^2$ distribution (see Fig. 3.17) to check how the additional selection cuts have affected the background $pp\pi^-$ events where a true proton was misidentified as a K^+ in

the K^+ selection. Figure 3.17 shows that the kinematic cuts have reduced the amount

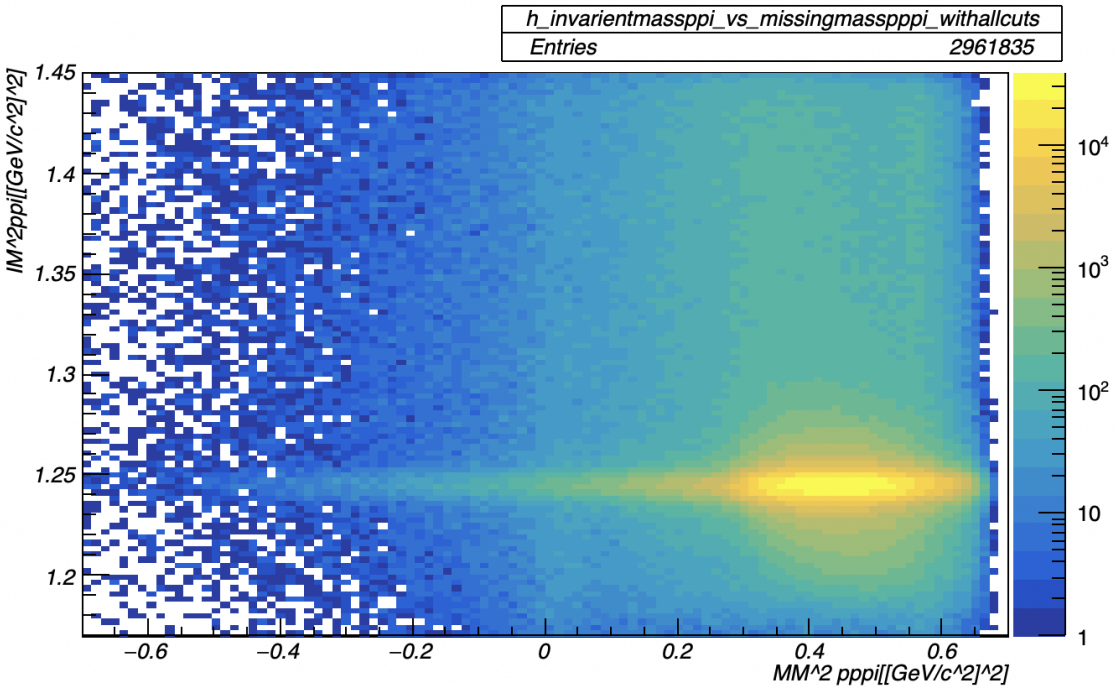

Figure 3.17 $IM^2_{p\pi^-}$ versus $MM_{pp\pi^-}{}^2$ distribution after all the cuts applied.

of $pp\pi^-$ events significantly such that the distribution does not visually exhibit any vertical structure at $MM_{pp\pi^-}{}^2 \sim 0$.

Similarly, we assessed the effect of the kinematic cuts on the amount of the background $p\pi^+\pi^-$ events. Figure 3.18 shows $IM_{p\pi^-}{}^2$ versus $MM_{p\pi^-\pi^+}{}^2$ distribution after all selection cuts have been applied. The distribution does not show any enhancement at the mass squared of the neutron peak, so we conclude the amount of this background in our data sample is minimized.

Finally, we assess the $IM_{p\pi^-}$ and the kaon-mass distributions of events that pass all of our selection cuts. Figure 3.19 shows the $IM^2_{p\pi^-}$ distribution. Qualitatively, the Λ peak looks like a Gaussian with a non-Gaussian, asymmetric long tails, whereas the tail at the higher invariant masses spans a wider range than the one at lower invariant masses. The mean value of the peak is 1.2445 $(\mathrm{GeV}/c^2)^2$, which is the nominal mass

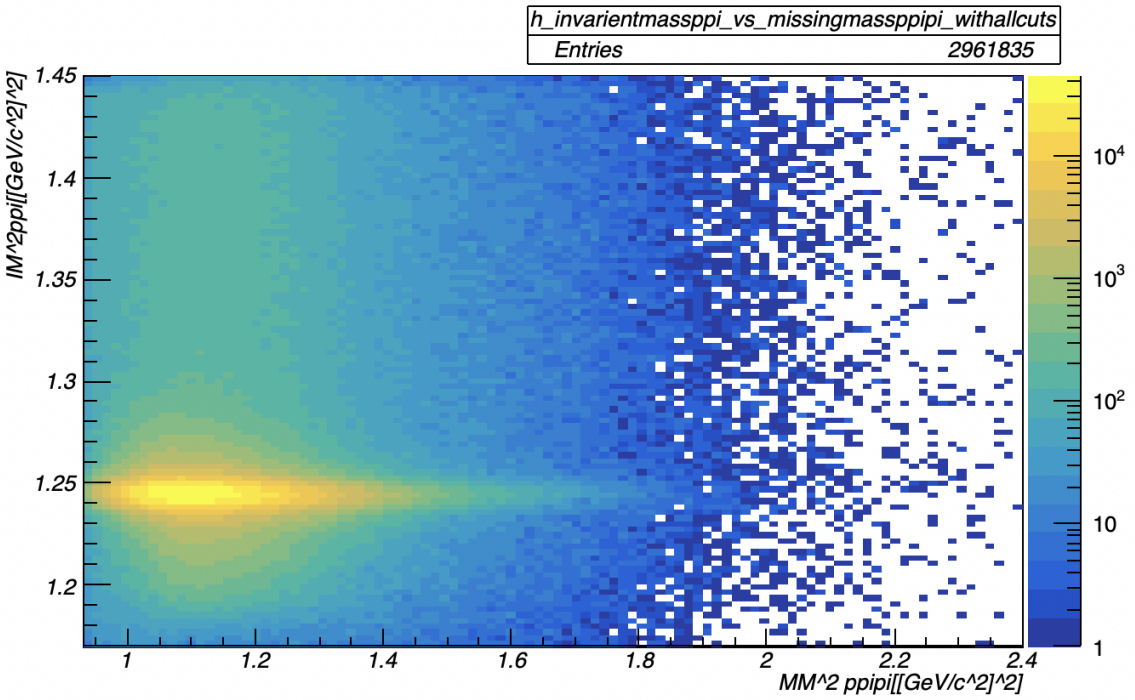

Figure 3.18 $IM^2_{p\pi^-}$ versus $MM_{p\pi^-\pi^+}{}^2$ distribution after all the cuts applied.

squared of Λ.

In a true Λ photoproduction, the hyperon is always produced with a K, so the number of true Λs in the $IM_{p\pi^-}$ can be obtained from the number of true kaons. To form the kaon-mass distribution of events that pass all of our selection cuts, we reconstructed the kaon mass from the measured momentum and relative speed, using the definition of relativistic momentum, as

$$m_K = \frac{p}{c}\sqrt{\frac{1}{\beta^2} - 1}, \tag{3.14}$$

where p and β are the measured momentum and relative speed, respectively. The kaon-mass distribution is shown in Fig. 3.20. It shows a peak at the nominal kaon mass with a slight enhancement of the lower-mass tail, compared to the higher-mass tail. This asymmetry suggests that there is a likelihood to have some misidentified π^+s passing all of our selection criteria. While the number of these events seems to be much smaller than the total number of events, we estimate it in the next step of

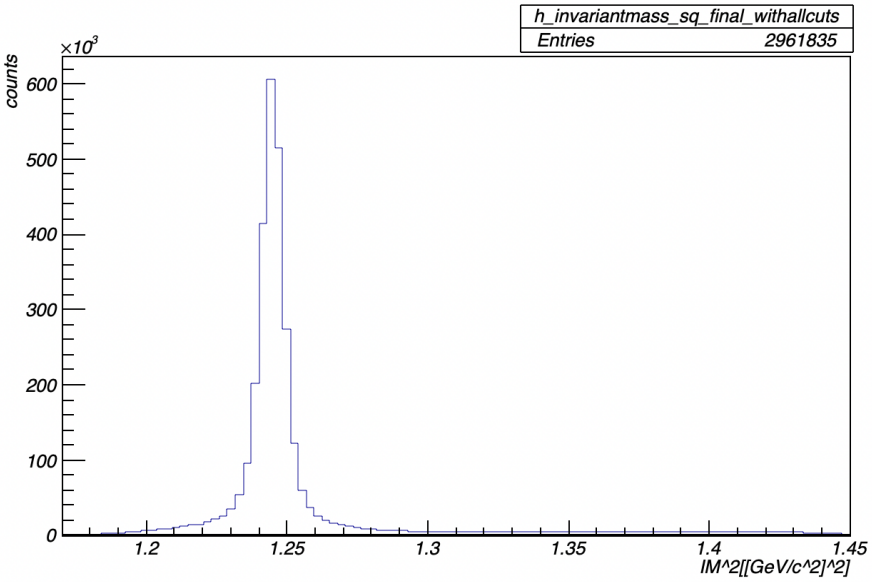

Figure 3.19 $IM_{p\pi^-}{}^2$ distribution after all the cuts applied.

our analysis.

3.2.3 Determination of the shape of the $IM_{p\pi^-}$ distribution over a wide range

We estimated the true number of Λ events in three different ways. Methods 1 and 2 involve the binning of the $IM_{p\pi^-}$ distribution in discrete intervals. The number of Λ events in each interval was obtained by background subtraction in the corresponding kaon-mass distribution assuming a simple Gaussian shape and a background. In method 3, we obtain the number of Λ events by means of only applying all of our selection cuts. Details about the application of each method are given below.

Method 1: In order to be able to estimate the amount of background in the kaon mass distribution, we formed a sample of events that pass all of our selection criteria except the kaon $\Delta\beta$ cut, which was removed. This allowed accidental background in the sample. The $IM_{p\pi^-}$ and the kaon mass distribution of this event sample is shown in Fig. 3.21 right and Fig. 3.22, respectively.

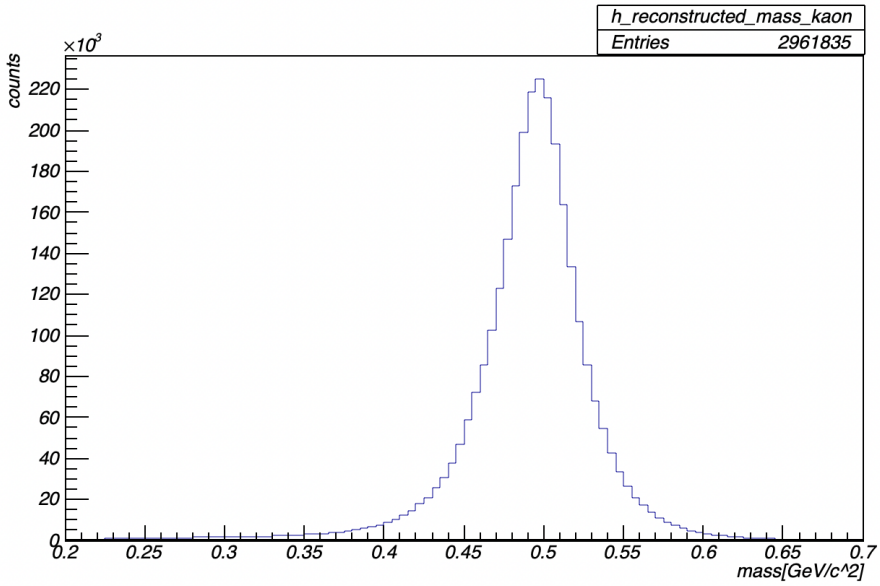

Figure 3.20 Reconstructed mass squared of K^+ after all the cuts have been applied.

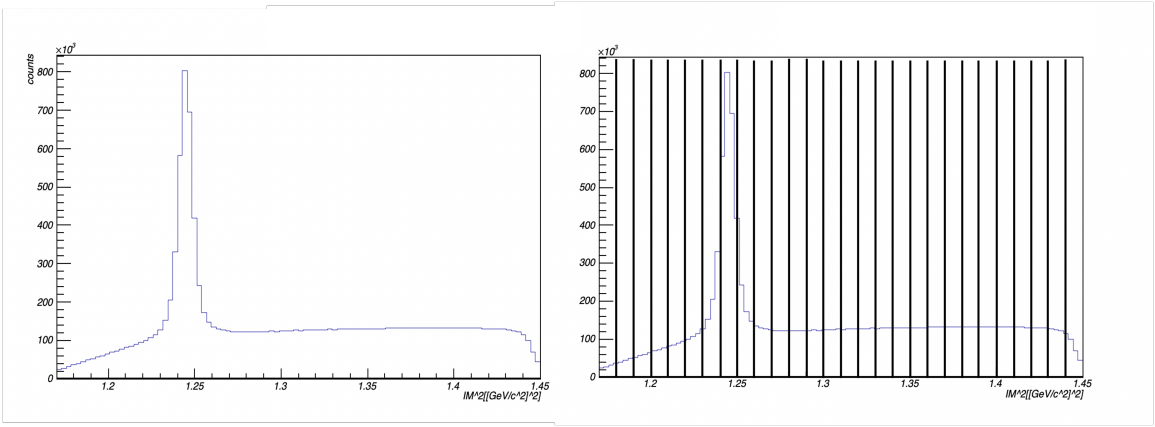

Figure 3.21 ${IM_{p\pi^-}}^2$ histogram for exclusive analysis excluding $\Delta\beta$ K^+ cut.

The kaon-mass distribution shows clearly a pion peak (true pions identified as kaons) and the tails of the proton peak (true protons identified as kaons). In the next step, we divided the $IM_{p\pi^-}$ distribution into subranges (see Fig. 3.21 left). For each such subrange, the K^+ mass distribution in the range between 0.3 GeV/c^2 and 0.7 GeV/c^2 was fitted to a Gaussian (for the peak) plus exponential (for the background) and to a Gaussian (for the peak) plus second-order polynomial function

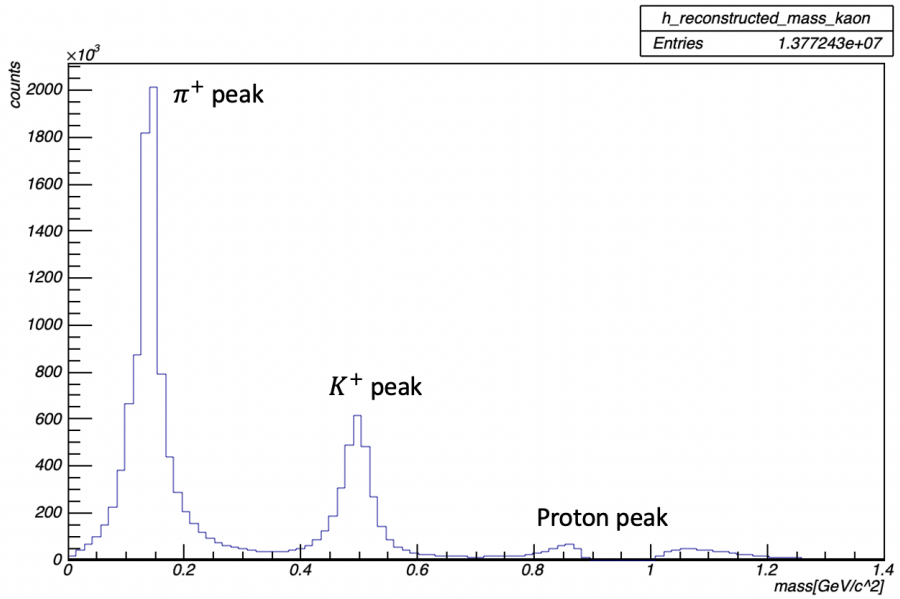

Figure 3.22 Reconstructed mass of K^+ after all the cuts were applied and the $\Delta\beta$ selection cut on K^+ was removed.

(for the background). The two sets of fits were performed in order to identify which function best described the background. The shape of the background, which is due to misidentified particles, was independent of the $IM_{p\pi^-}$ bin. Figures 3.23 and 3.24 show examples of the K^+-mass fitting for one bin of ${IM_{p\pi^-}}^2$.

The black-colored histogram in each of the bottom panels is the background-subtracted distribution, which was obtained by subtracting the background function (blue color function of the top figure) from the K^+ mass histogram (blue color histogram of the top figure). This histogram gives us the number of Λ events in that IM bin.

When comparing the two fits, the quality of the fit functions was evaluated by using the χ^2 fit value. During fitting, χ^2/NDF (chi-squared per the number of degrees of freedom) was determined for each bin for both fitted functions. Considering this specific ${IM_{p\pi^-}}^2$ bin, χ^2/NDF for the second-order polynomial, background fit was 2.62, and for the exponential, background fit was 2.08. In both fits, the χ^2/NDF value is reasonably close to 1 (given the fact that we do not know the true shape

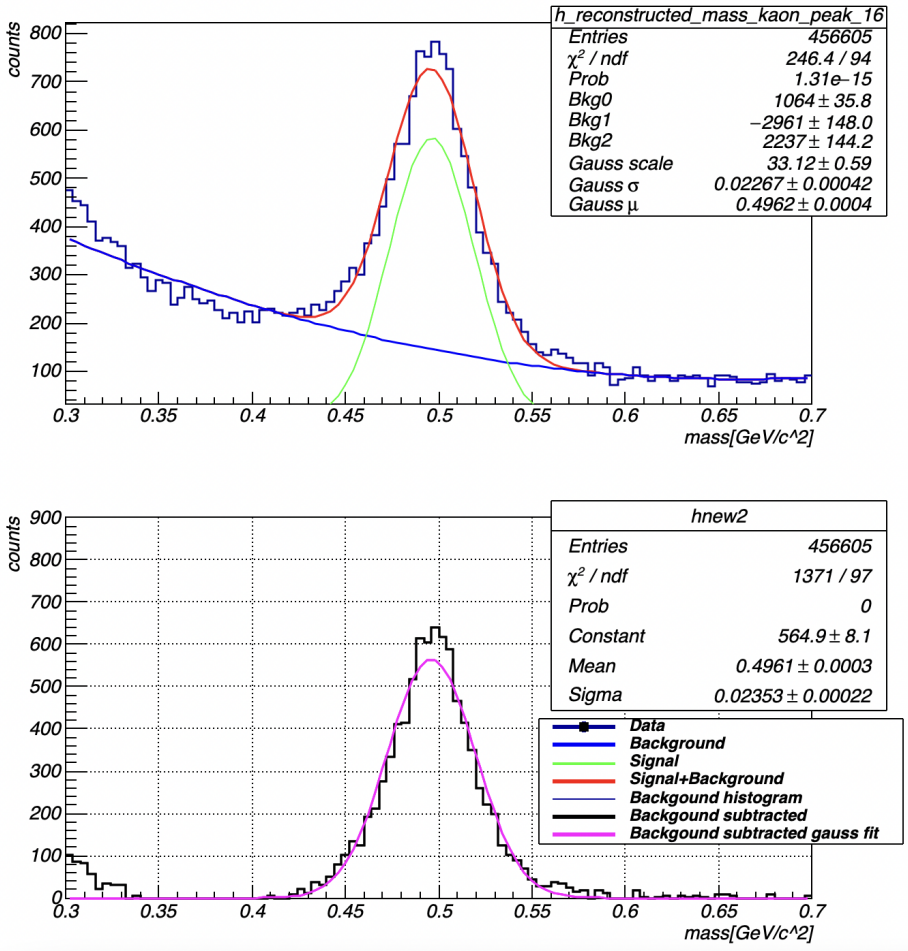

Figure 3.23 Reconstructed mass of K^+ distribution for $IM_{p\pi^-}{}^2$ bin 1.32 – 1.33 ((GeV/c^2)^2) fitted with Gaussian+second order polynomial (K^+ $\Delta\beta$ cut is excluded).

of the kaon-mass peak), but the exponential fit quality is somewhat higher than the quality of the second-order polynomial fit. So the exponential fit was considered to be a better fit than the second-order polynomial and it was used further in our analysis. The χ^2/NDF was high for some low-statistics bins and those bins were removed from the analysis.

Method 2: The strategy here is the same as for Method 1, except, we use the event sample obtained after the application of all of our selection cuts, including the K^+ $\Delta\beta$ cut (as shown in Fig. 3.19 and Fig. 3.20). The $IM_{p\pi^-}{}^2$ distribution was divided into bins with a width each of 0.1 (GeV/c^2)^2 and for each bin the reconstructed

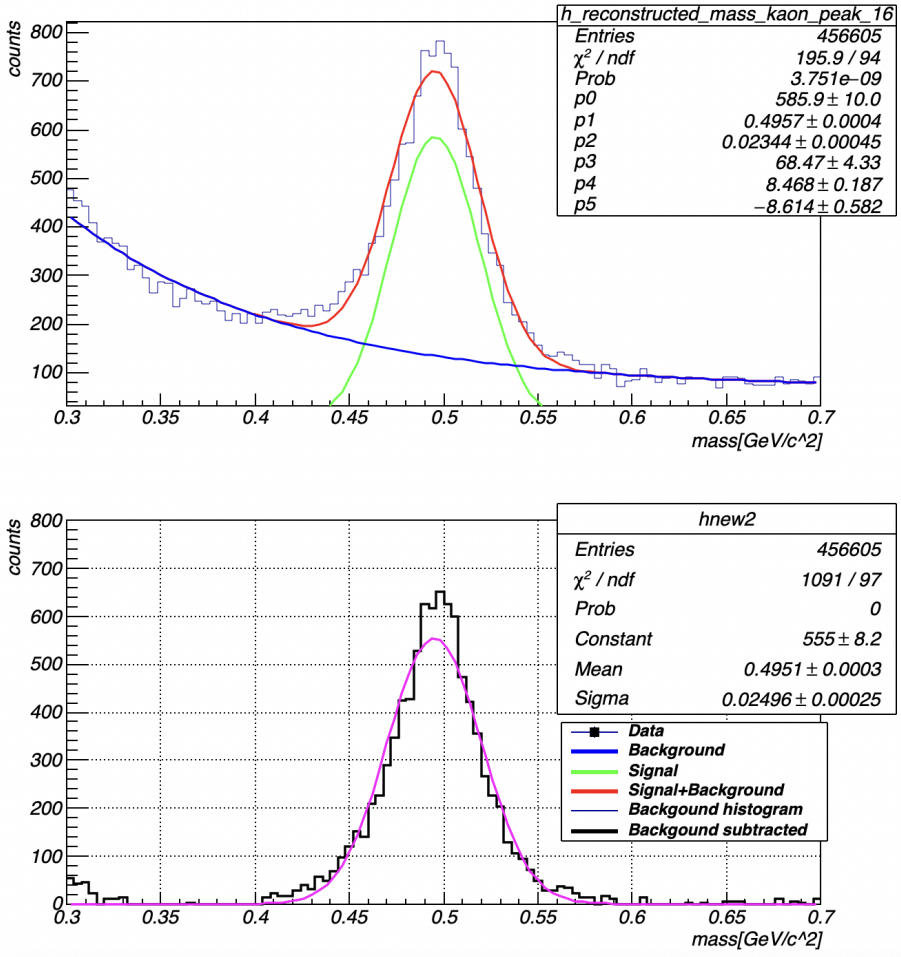

Figure 3.24 Reconstructed mass of K^+ distribution for $IM_{p\pi^-}{}^2$ bin 1.32 – 1.33 $((\mathrm{GeV}/c^2)^2)$ fitted with Gaussian+exponential (K^+ $\Delta\beta$ cut is excluded).

mass of K^+ distribution was plotted. Then the peak was fitted with a Gaussian function and the background was fitted with an exponential function.

In Figure 3.25 we demonstrate the background subtraction for one IM bin. The χ^2/NDF value is 2.97 and gives an overall reasonable description of the background.

Considering all the other kinematic bins, the same process was conducted and the bins that gave fitted results with high χ^2/NDF values were removed from the fitting.

In both, methods 1 and 2, the total number of events was counted within the mass range 0.4 $((\mathrm{GeV}/c^2)^2)$ to 0.6 $((\mathrm{GeV}/c^2)^2)$. That gave us the total number of K^+ events, which was also the total number of Λ events for each $IM_{p\pi^-}{}^2$ bin.

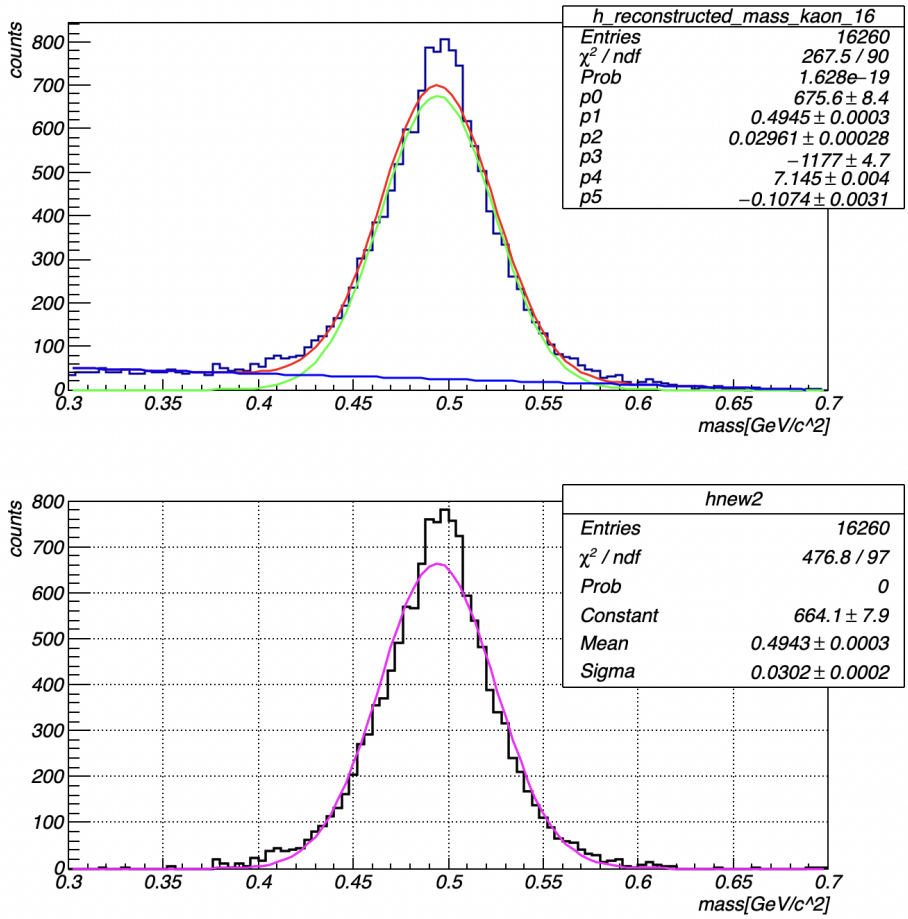

Figure 3.25 Reconstructed mass of K^+ distribution for $IM_{p\pi^-}{}^2$ bin 1.32 – 1.33 $((\mathrm{GeV}/c^2)^2)$ fitted with Gaussian+exponential (K^+ $\Delta\beta$ cut is included).

Method 3: Considering that our selection cuts reduce significantly the background and produce an event sample that is close to being background-free (see Fig. 3.19), we counted the number of events for each $IM_{p\pi^-}{}^2$ kinematic bin. This method has the advantage of having no background subtraction, and therefore, does not have systematic uncertainty due to the assumption about the shapes of the peak and the background. One has to keep in mind, though, that it contains a small contamination of accidental background events.

Figure 3.26 shows the distribution of the number of Λ events obtained with the three methods over the average value of the $IM_{p\pi^-}{}^2$ bin. The non-Gaussian asym-

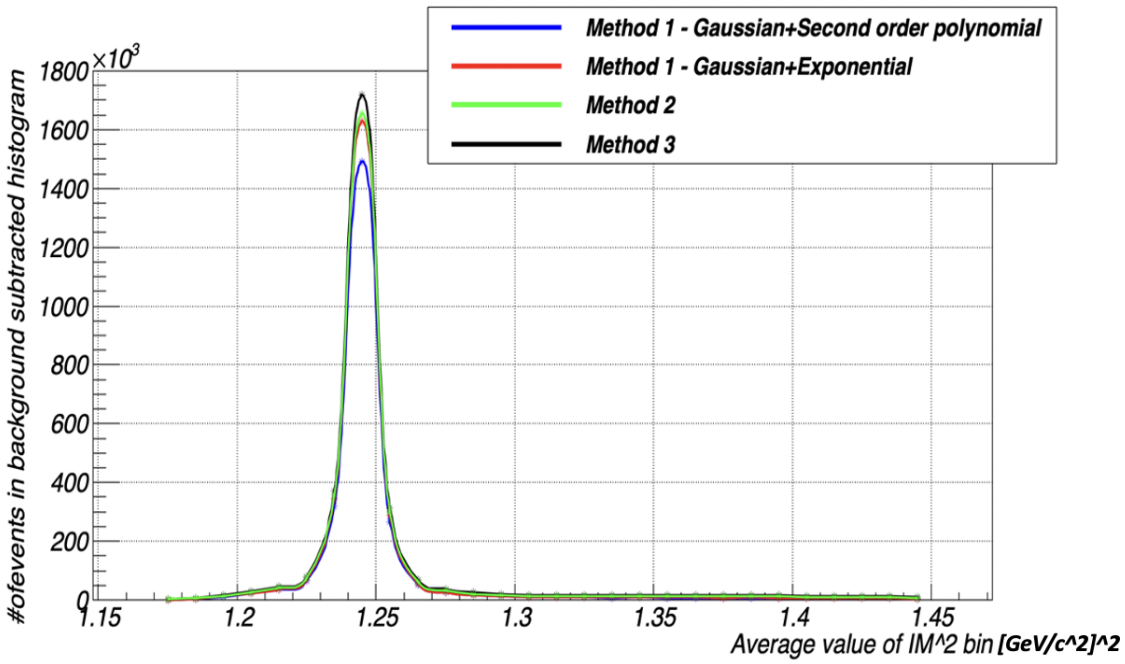

Figure 3.26 Number of Λ events versus the average value of $IM_{p\pi^-}{}^2$ bin obtained with three methods discussed in the text.

metric tail is clearly visible in all cases. The total number of Λ events within the full IM range obtained with the three methods is shown in Table 3.1.

Table 3.1 Number of good Λ counted in the data set for considered methods.

Method	Number of good Λ events
1, Gaussian + second-order polynomial	2440315
1, Gaussian + exponential	2641028
2	2786033
3	2961838

One can see that the Gaussian+second-order polynomial fit in Method 1 yields a systematically lower number of events than the Gaussian+exponential fit. Since the quality of the latter was assessed to be better, we disregard the result of the former.

A comparison of the results obtained with methods 2 and 3 yields an upper limit of the number of background events remaining in the sample for Method 3 (selection

cuts only) as well as an upper limit of the amount of good events removed by the background subtraction in Method 2. This is because the background subtraction on the kaon mass distribution disregards the non-Gaussian tails of that distribution, *i.e.*, misses good kaon events in these tails. Thus, while the number of Λ events obtained with Method 2 is underestimated, the number obtained with Method 3 is overestimated. The difference between the two numbers is about 6%.

3.2.4 Inclusive-Yield Correction Factor

The correction factor that needs to be applied to the inclusive Λ yields is calculated as the ratio R of the number of Λ events calculated as an average of the numbers obtained with Methods 2 and 3 to the number of Λ events considering the Λ peak to be a simple Gaussian (obtained after background subtraction of the IM distribution shown in Fig. 3.21 right that models the Λ peak with a Gaussian and the background with a polynomial of second order). The background subtraction is demonstrated in Fig. 3.27.

$$R = \frac{N_{\Lambda}}{N_{\Lambda,\mathrm{GaussPeak}}} = \frac{2873936}{2488008} = 1.155. \tag{3.15}$$

This factor accounts for the fact that in the inclusive yields extracted by means of background subtraction, good events in the non-Gaussian tails of the IM Λ peak were not counted. The fraction of these events is 15.5%.

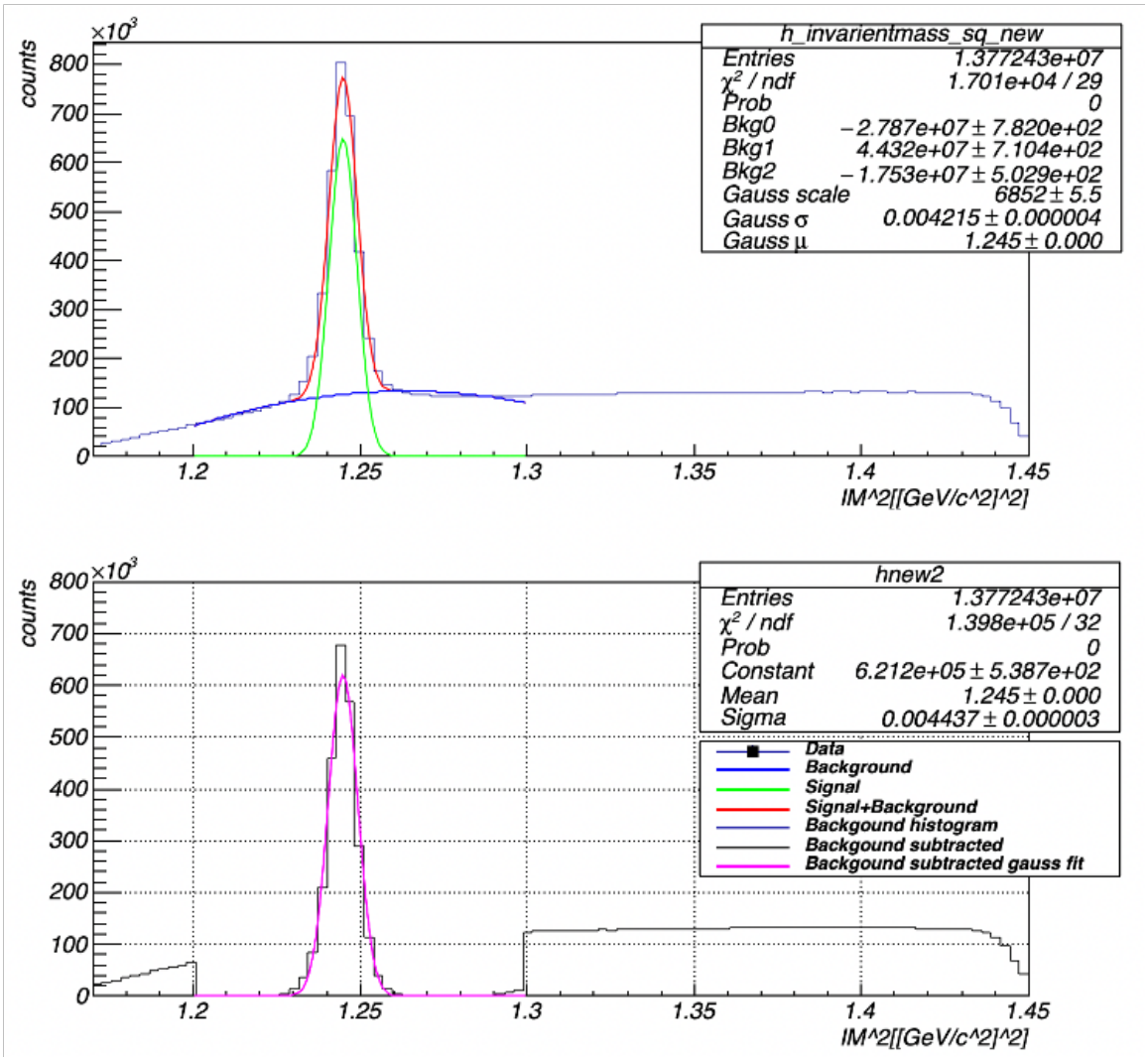

Figure 3.27 Background subtraction of the $IM_{p\pi^-}{}^2$ histogram when excluding the $\Delta\beta$ K^+ cut, fitted with Gaussian + second order polynomial functions. The Λ events within the background-subtracted Gaussian peak were counted in the range of 1.22 – 1.27 $(\mathrm{GeV}/c^2)^2$.

Chapter 4

Results

Figure 4.1 shows our results for the inclusive $\gamma d \to \Lambda X$ yields for all kinematic bins where we obtained good background fits. The statistical uncertainties of N_Λ are smaller than the symbol size. The width of the bin of θ angle is 0.1 rad, which is represented by the X error bars.

The yields need to be corrected for the error due to the exclusion of the long tails of the Λ peak in our background subtraction. To assess whether a common correction factor could be applied to each yield, we monitored the position and the width of the background-subtracted Λ peaks.

Figure 4.2 shows the peak position obtained as the mean value of the Gaussian fit to the background subtracted histograms for each $(p_\Lambda, \theta_\Lambda)$ bin. Here it can be observed that the peak position remains unchanged over all bins. The mean value is very close to the nominal mass of Λ, 1.1156 GeV/c^2. The small deviation from the nominal value can be attributed to errors in the momentum determination in the proton and/or the pion or error in the background shape during the IM background subtraction.

Figures 4.3 and 4.4 show the width the Λ peak estimated from the standard deviation of the Gaussian fit to the background-subtracted IM histograms. One can see that for a given momentum bin, the width of the peak decreases as the polar angle increases. The largest variation, observed at the lowest momentum bin, is about 17%. Overall, as the momentum increases, the peak becomes narrower, which is primarily due to decreased energy-loss effects for higher momenta particles. Considering both

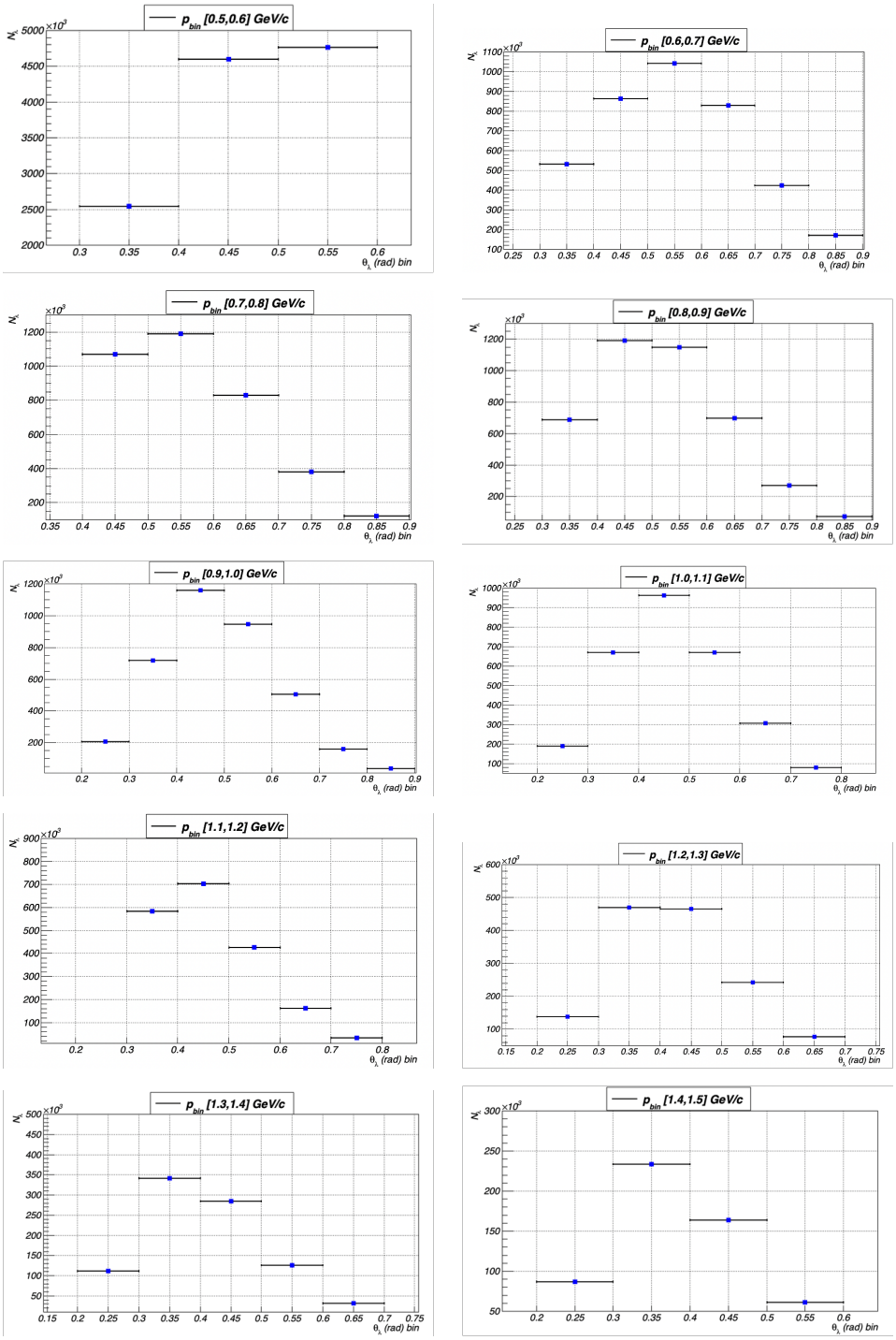

Figure 4.1 N_Λ versus θ. The statistical uncertainty of the yield is smaller than the marker size for each data point. The X error bars show the width of the θ bin.

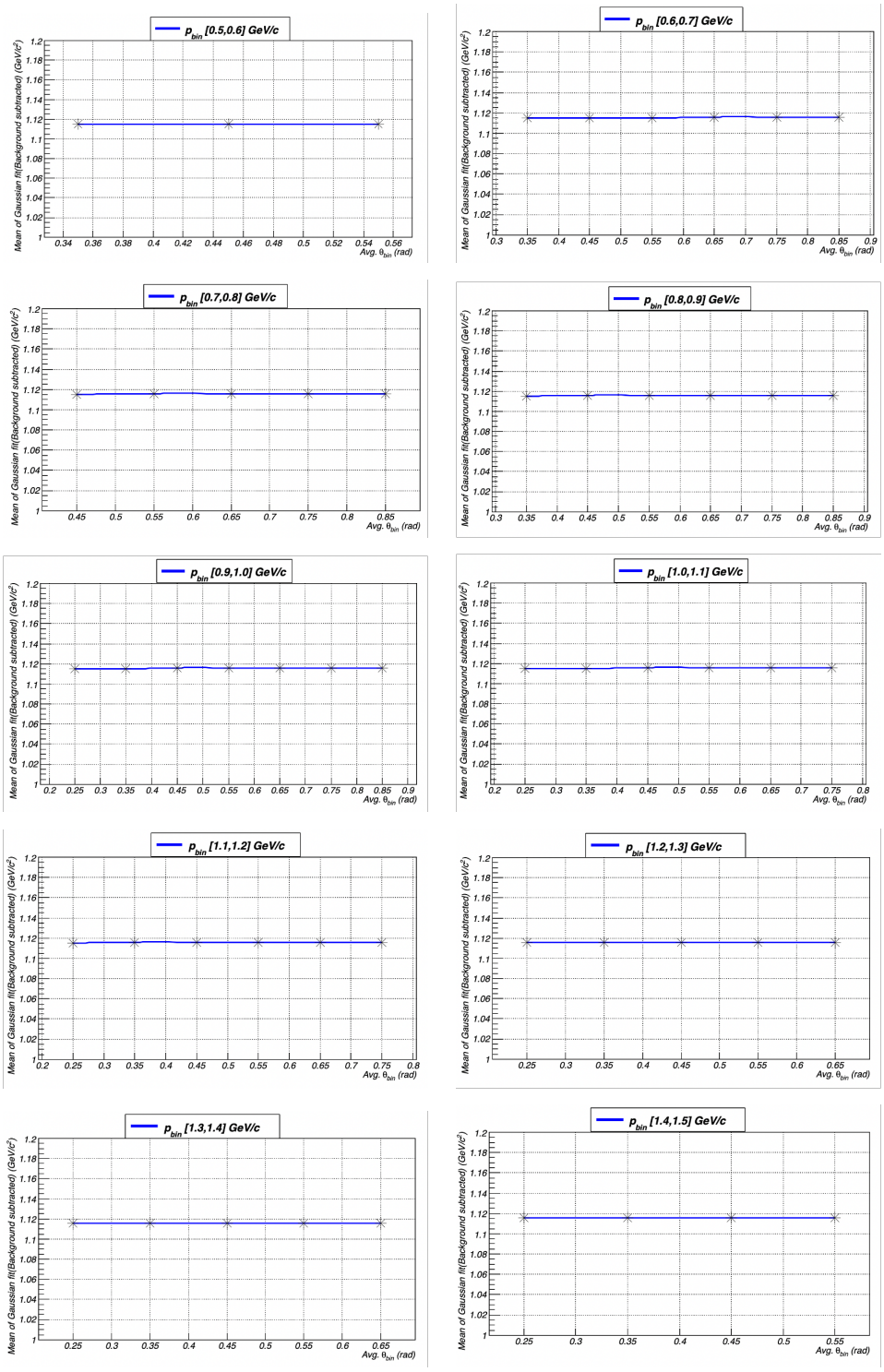

Figure 4.2 Mean value of Gaussain peak fit of background subtracted histograms of $IM_{p\pi^-}$ distribution for each $(p_\Lambda, \theta_\Lambda)$ bin.

figures, it can be concluded that the width of the Lambda peak varies both with hyperon momentum and polar angle.

The varying peak width brings up the question whether a common correction factor can be applied to all yields to account for the loss of peak tails in our yield extraction. We consider that this would be reasonable as the correction factor accounts for the relative fraction of the yield in the non-Gaussian tails to the total yield and we do not expect this fraction to change as the peak width changes. Qualitatively, this is because as the Λ peaks become wider (or narrower), its non-Gaussian tails also become wider (or narrower). This statement needs to be quantified in future work.

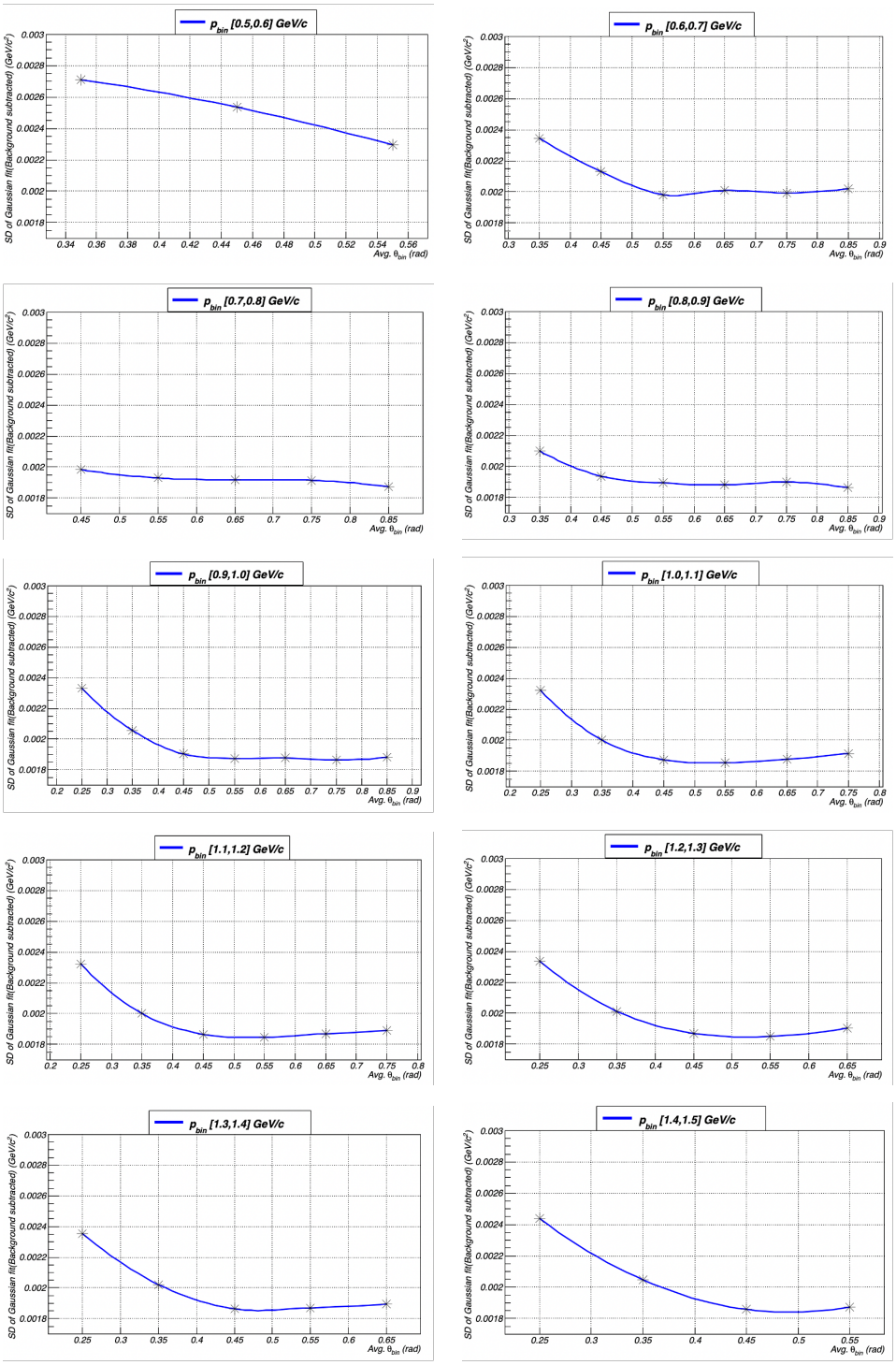

Figure 4.3 Standard deviation value of Gaussian peak fit of background subtracted histograms of $IM_{p\pi^-}$ distribution for each $(p_\Lambda, \theta_\Lambda)$ bin.

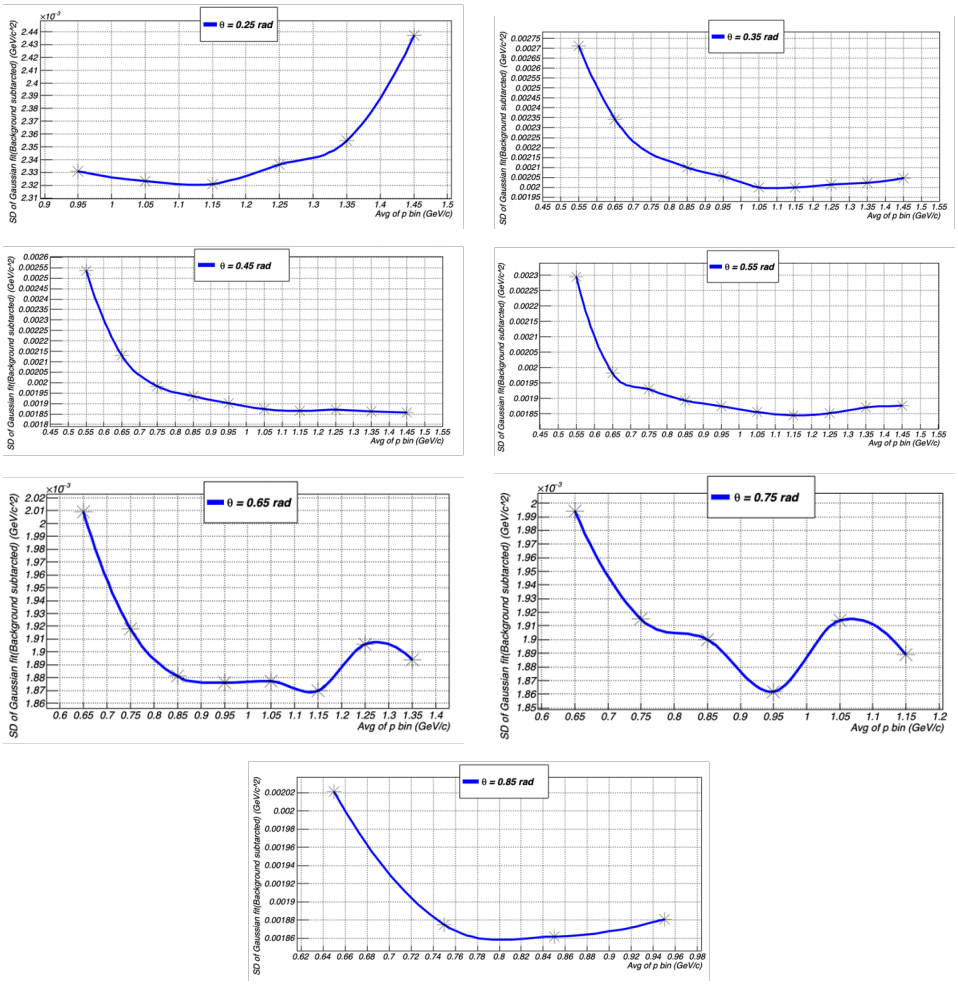

Figure 4.4 Standard deviation value of Gaussian peak fit of background subtracted histograms of $IM_{p\pi^-}$ distribution for each $(\theta_\Lambda, p_\Lambda)$ bin.

Chapter 5

Summary and Outlook

In this work, we extracted preliminary yields for the $\gamma d \to \Lambda X$ reaction in bins of Λ scattering angle and Λ momentum in the laboratory system. We also quantified the systematic error of the background subtraction used in the yield extraction by analyzing the exclusive reaction $\gamma d \to K^+ \Lambda n$. The main characteristics of the data, such as statistical significance, kinematic coverage, properties of the Λ peak, shape of background were identified and the main analysis methods established.

With these yields, future determination of the acceptance of the detector, and simulations, the luminosity for Λd scattering can be determined, which makes it possible to calculate Λd scattering cross sections of reactions such as $\Lambda d \to \Lambda d$, $\Lambda d \to \Lambda pn$, and any other reaction having the same initial state studied in the g13 data set. Differential cross sections would be extracted as

$$\frac{d\sigma}{dcos(\theta)} = \frac{dY}{A \times \mathcal{L} \times B.R \times dcos(\theta)}, \tag{5.1}$$

where dY is the yield of the reaction of interest, A is the CLAS acceptance for that reaction, $\mathcal{L}$ is the luminosity, and B.R. is the $\Lambda \to p\pi^-$ branching ratio.

Future work on the ΛX yield will involve the determination of the systematic uncertainties of the yield extraction, determination of the CLAS acceptance for inclusive Λ photoproduction in g13, a binning on the z-vertex, and adding the g13b data set to the analysed event sample. This will allow for finer binning in $p_\Lambda, \theta_\Lambda, z_\Lambda$. A more accurate determination of z_Λ, which does not assume that the proton and the pion originate from the target would, for example, reduce the error of the z-vertex cut.

Bibliography

[1] John W Price and CLAS Collaboration. "Λ p elastic scattering in the CLAS detector". In: *AIP Conference Proceedings*. Vol. 2130. 1. AIP Publishing LLC. 2019, p. 020004.

[2] Joseph A Rowley. *Improved Λp Elastic Scattering Cross Sections Between 0.9 and 2.0 GeV/c and Connections to the Neutron Stars*. Ohio University, 2022.

[3] Salam Agus, Kazuya Miyagawa, et al. "K^ 0 photoproduction on the deuteron". In: ().

[4] T Nanamura et al. "The Analysis Status of\varSigma^+ p Σ+ p Scattering Events in the J-PARC E40 Experiment". In: *Few-Body Systems* 62 (2021), pp. 1–6.

[5] Bernhard A Mecking et al. "The CEBAF large acceptance spectrometer (CLAS)". In: *Nuclear Instruments and Methods in Physics Research Section A: Accelerators, Spectrometers, Detectors and Associated Equipment* 503.3 (2003), pp. 513–553.

[6] YC Chao et al. "CEBAF accelerator achievements". In: *Journal of Physics: Conference Series*. Vol. 299. 1. IOP Publishing. 2011, p. 012015.

[7] Christoph W Leemann, David R Douglas, and Geoffrey A Krafft. "The continuous electron beam accelerator facility: CEBAF at the Jefferson Laboratory". In: *Annual Review of Nuclear and Particle Science* 51.1 (2001), pp. 413–450.

[8] G Adams et al. "The CLAS cherenkov detector". In: *Nuclear Instruments and Methods in Physics Research Section A: Accelerators, Spectrometers, Detectors and Associated Equipment* 465.2-3 (2001), pp. 414–427.

[9] Tongtong Cao. "Determination of the polarization observables C x, Cz, and Py for the quasi-free mechanisms and the final-state interactions respectively in polarized d → K+polarized n". In: *University of South Carolina, ProQuest Dissertations Publishing*. 2016, pp. 1–153.

Appendix A

Background subtracted $IM_{p\pi^-}$ histograms for the inclusive analysis fitted with Gaussian + second order polynomial functions for all $(p_\Lambda, \theta_\Lambda)$ bins

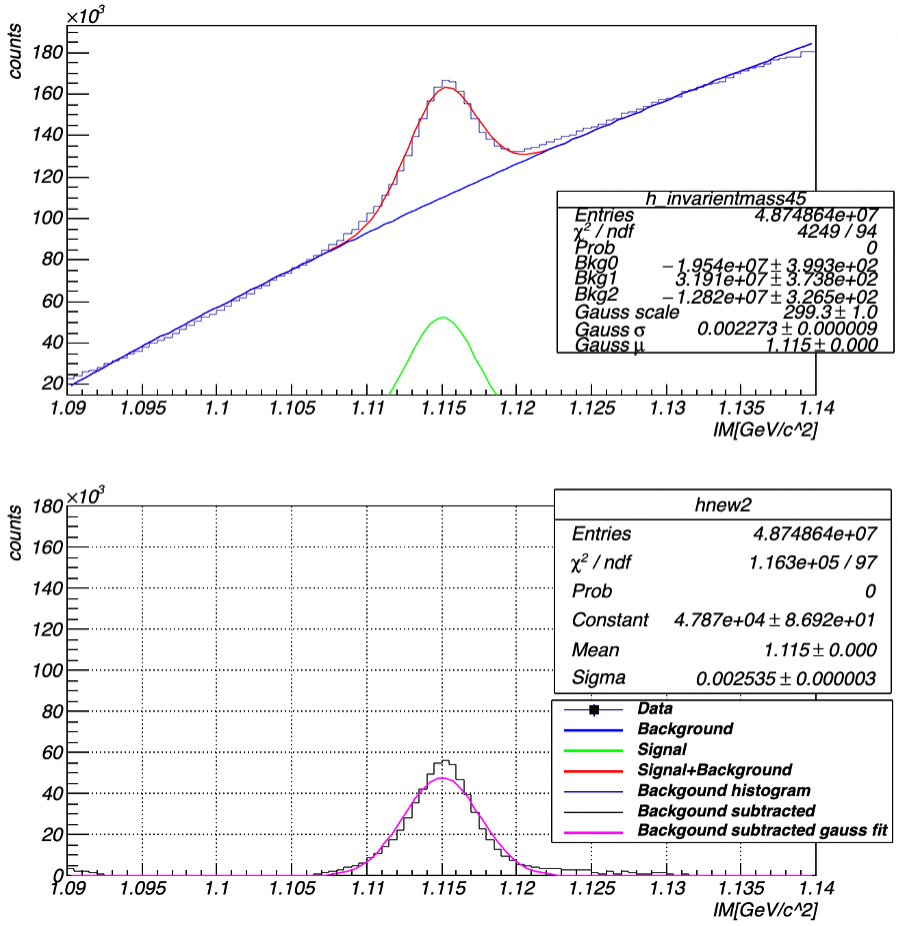

Figure A.1 Background subtraction on $IM_{p\pi^-}$ for the inclusive analysis using a fit to a Gaussian + second order polynomial functions for $p_\Lambda = [0.5, 0.6]$ GeV/c and $\theta_\Lambda = [0.4, 0.5]$ rad.

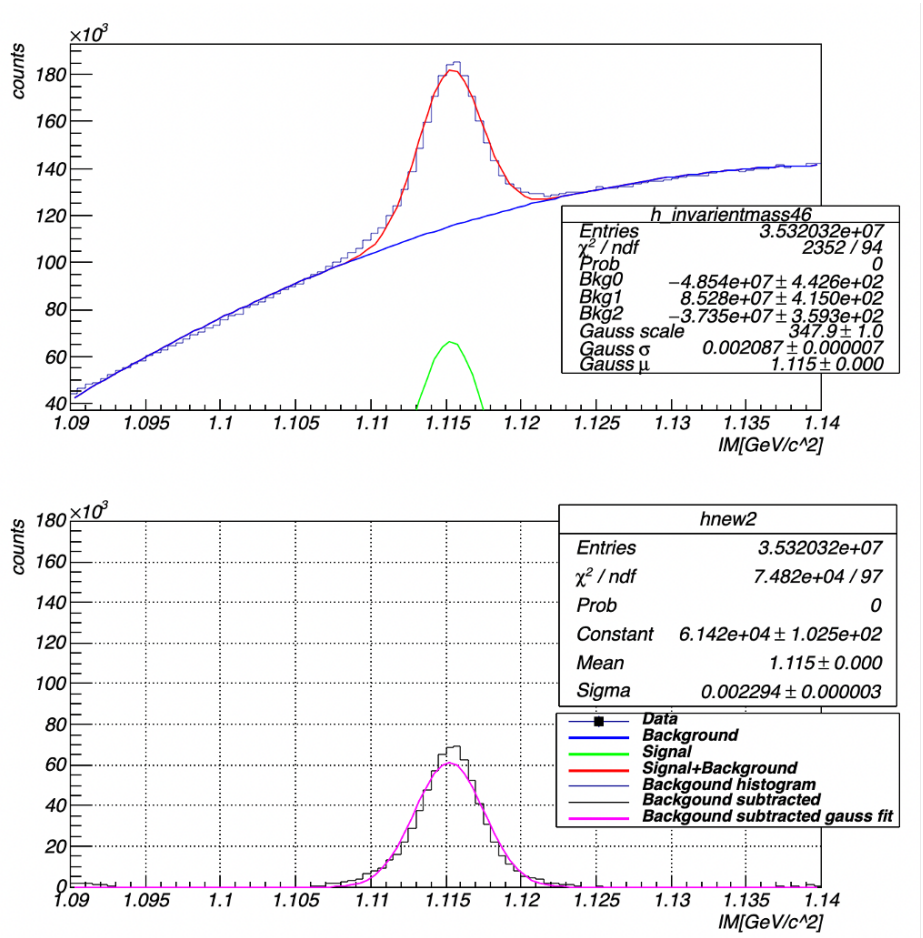

Figure A.2 Background subtraction on $IM_{p\pi^-}$ for the inclusive analysis using a fit to a Gaussian + second order polynomial functions for $p_\Lambda = [0.5, 0.6]$ GeV/c and $\theta_\Lambda = [0.5, 0.6]$ rad.

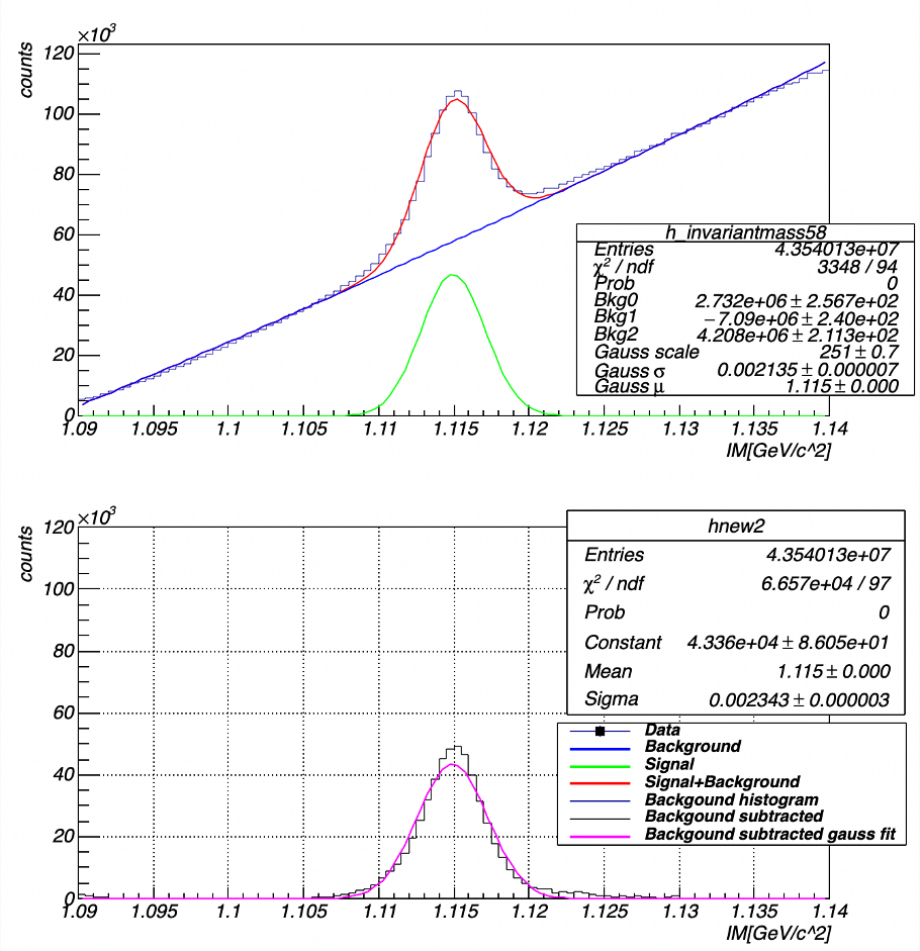

Figure A.3 Background subtraction on $IM_{p\pi^-}$ for the inclusive analysis using a fit to a Gaussian + second order polynomial functions for $p_\Lambda = [0.6, 0.7]$ GeV/c and $\theta_\Lambda = [0.3, 0.4]$ rad.

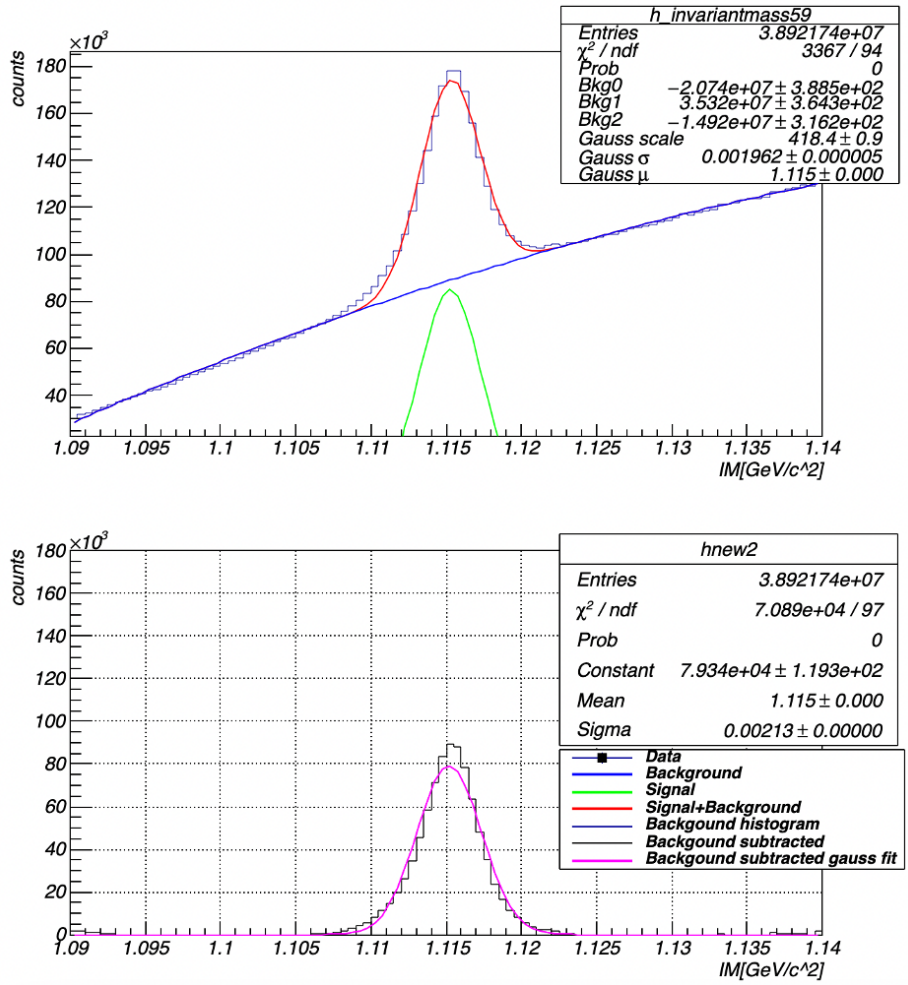

Figure A.4 Background subtraction on $IM_{p\pi^-}$ for the inclusive analysis using a fit to a Gaussian + second order polynomial functions for $p_\Lambda = [0.6, 0.7]$ GeV/c and $\theta_\Lambda = [0.4, 0.5]$ rad.

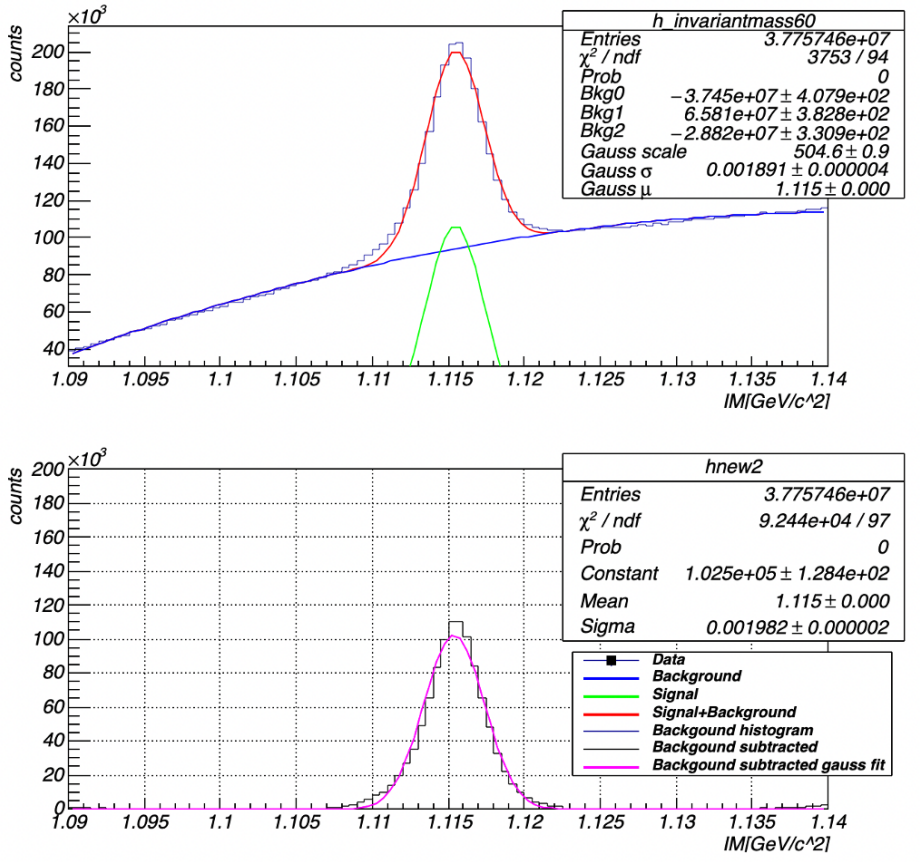

Figure A.5 Background subtraction on $IM_{p\pi^-}$ for the inclusive analysis using a fit to a Gaussian + second order polynomial functions for $p_\Lambda = [0.6, 0.7]$ GeV/c and $\theta_\Lambda = [0.5, 0.6]$ rad.

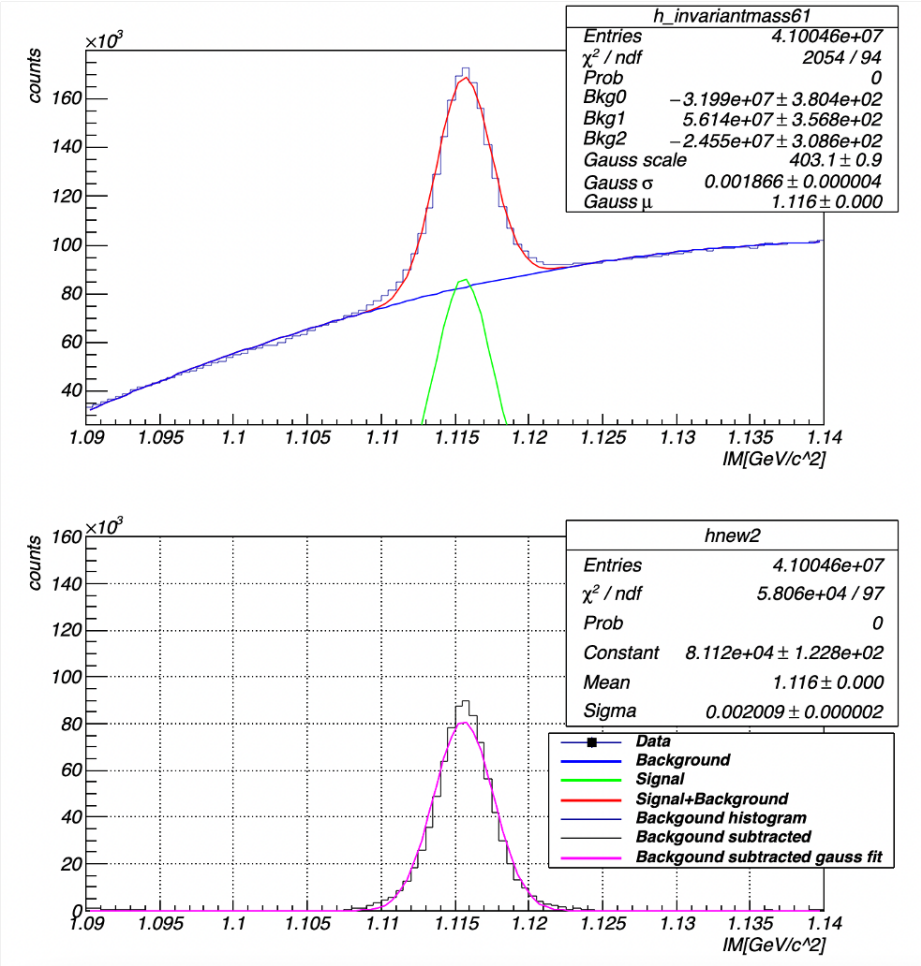

Figure A.6 Background subtraction on $IM_{p\pi^-}$ for the inclusive analysis using a fit to a Gaussian + second order polynomial functions for $p_\Lambda = [0.6, 0.7]$ GeV/c and $\theta_\Lambda = [0.6, 0.7]$ rad.

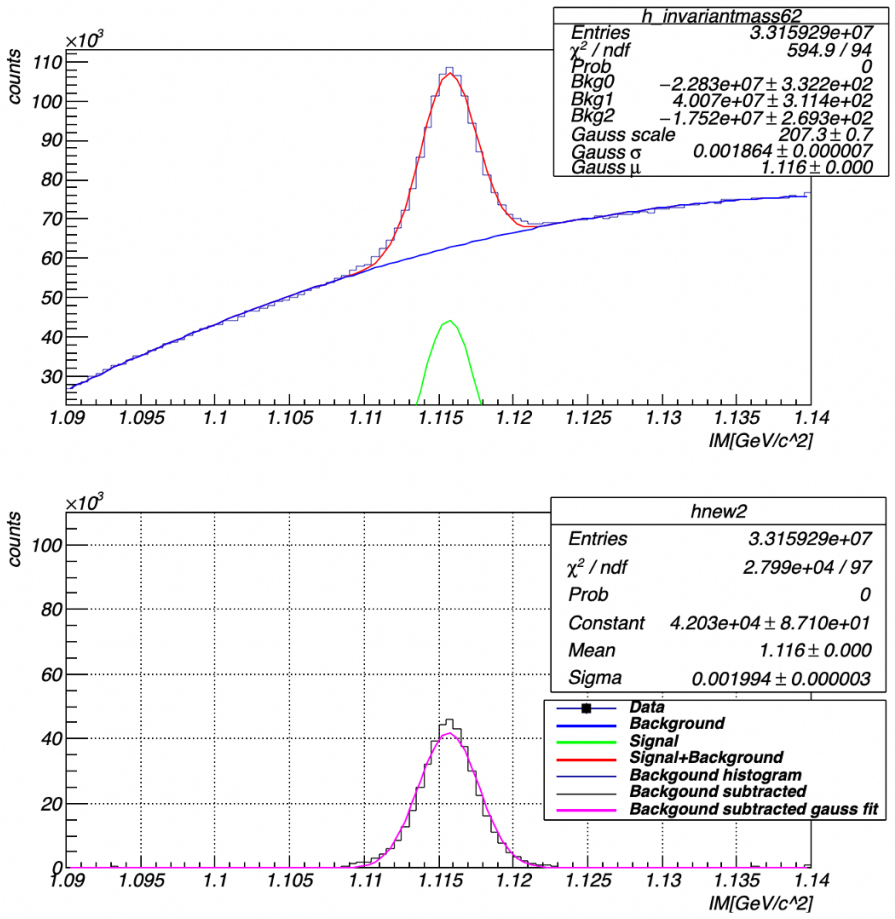

Figure A.7 Background subtraction on $IM_{p\pi^-}$ for the inclusive analysis using a fit to a Gaussian + second order polynomial functions for $p_\Lambda = [0.6, 0.7]$ GeV/c and $\theta_\Lambda = [0.7, 0.8]$ rad.

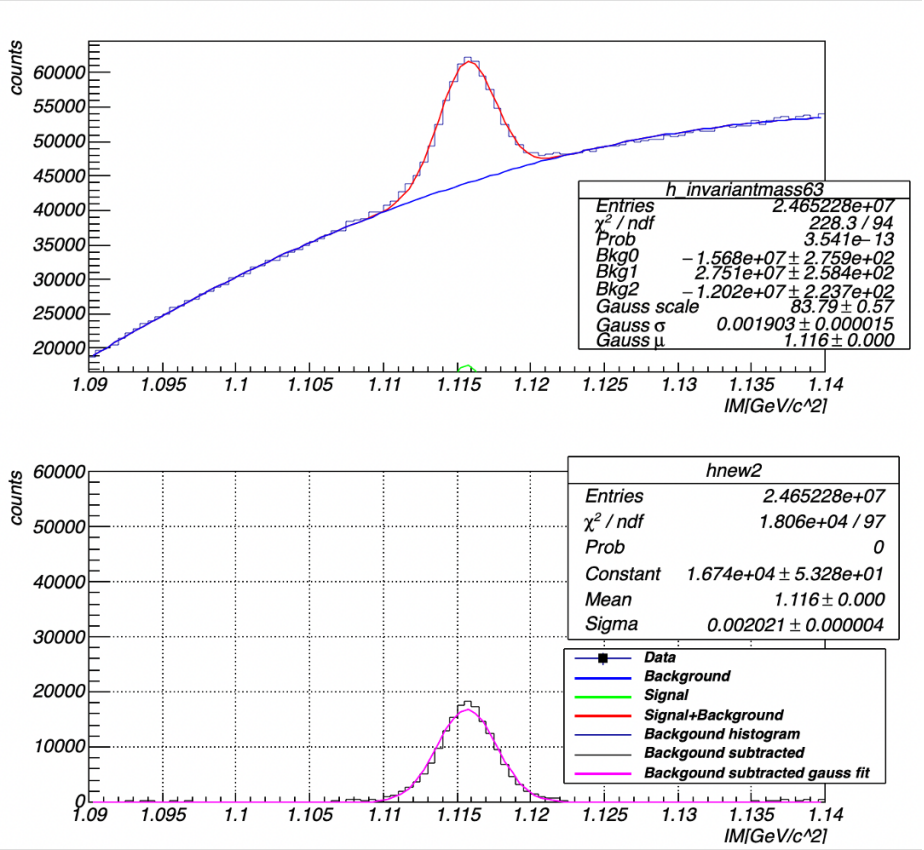

Figure A.8 Background subtraction on $IM_{p\pi^-}$ for the inclusive analysis using a fit to a Gaussian + second order polynomial functions for $p_\Lambda = [0.6, 0.7]$ GeV/c and $\theta_\Lambda = [0.8, 0.9]$ rad.

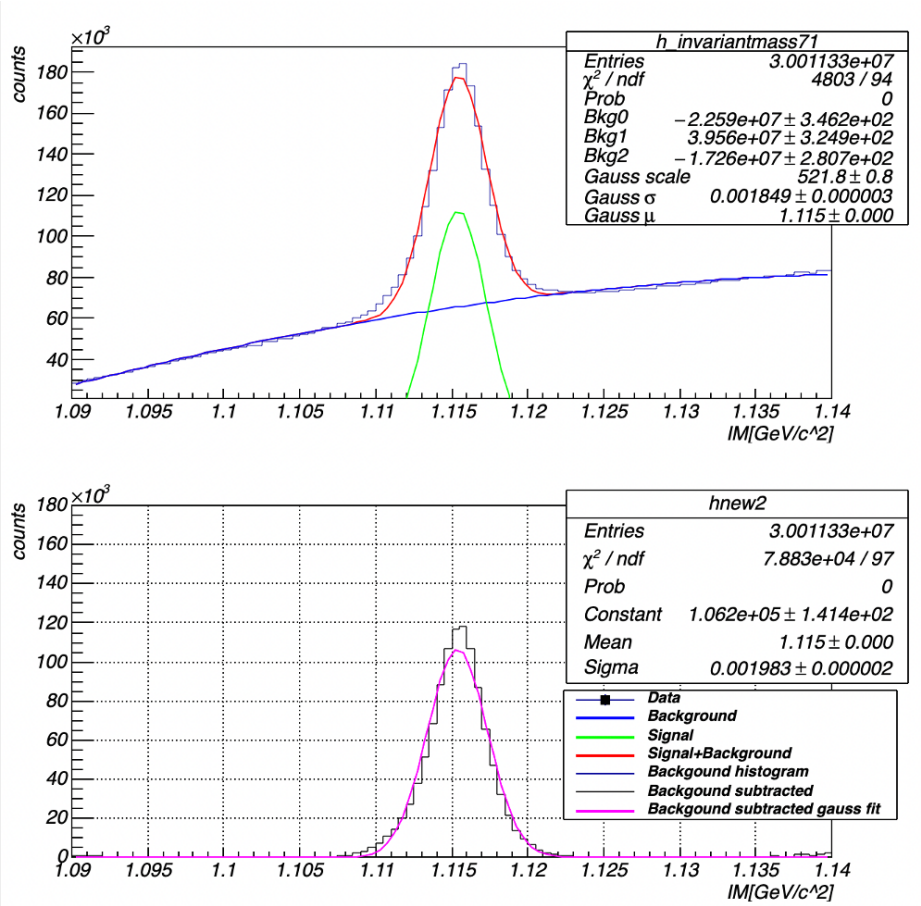

Figure A.9 Background subtraction on $IM_{p\pi^-}$ for the inclusive analysis using a fit to a Gaussian + second order polynomial functions for $p_\Lambda = [0.7, 0.8]$ GeV/c and $\theta_\Lambda = [0.4, 0.5]$ rad.

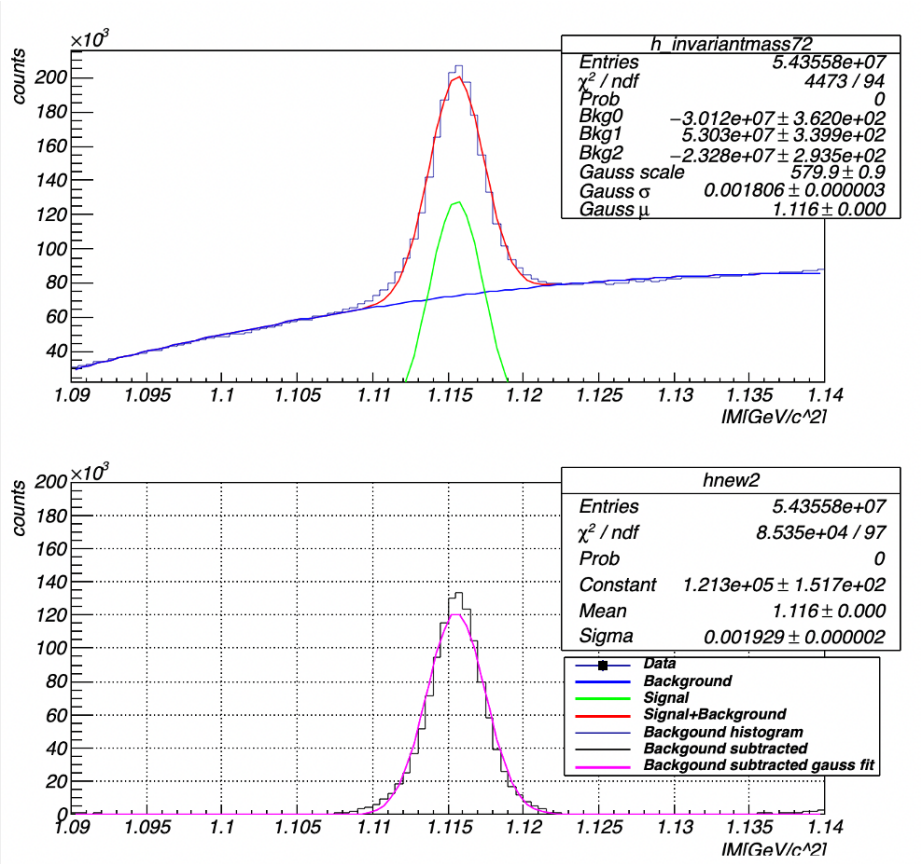

Figure A.10 Background subtraction on $IM_{p\pi^-}$ for the inclusive analysis using a fit to a Gaussian + second order polynomial functions for $p_\Lambda = [0.7, 0.8]$ GeV/c and $\theta_\Lambda = [0.5, 0.6]$ rad.

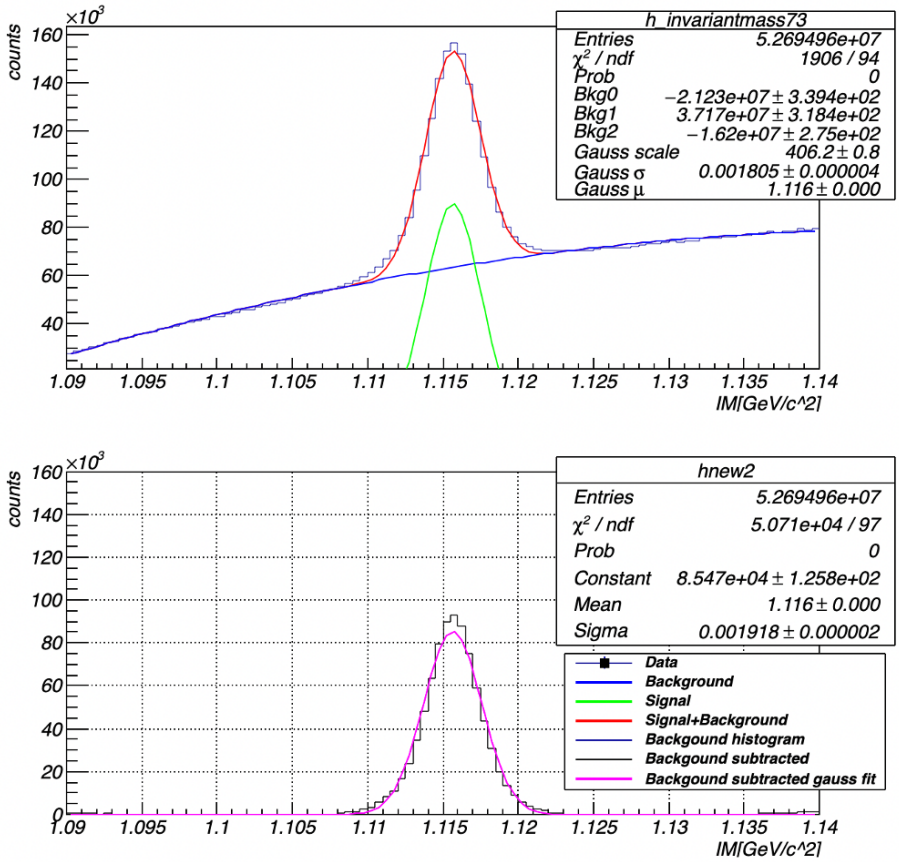

Figure A.11 Background subtraction on $IM_{p\pi^-}$ for the inclusive analysis using a fit to a Gaussian + second order polynomial functions for $p_\Lambda = [0.7, 0.8]$ GeV/c and $\theta_\Lambda = [0.6, 0.7]$ rad.

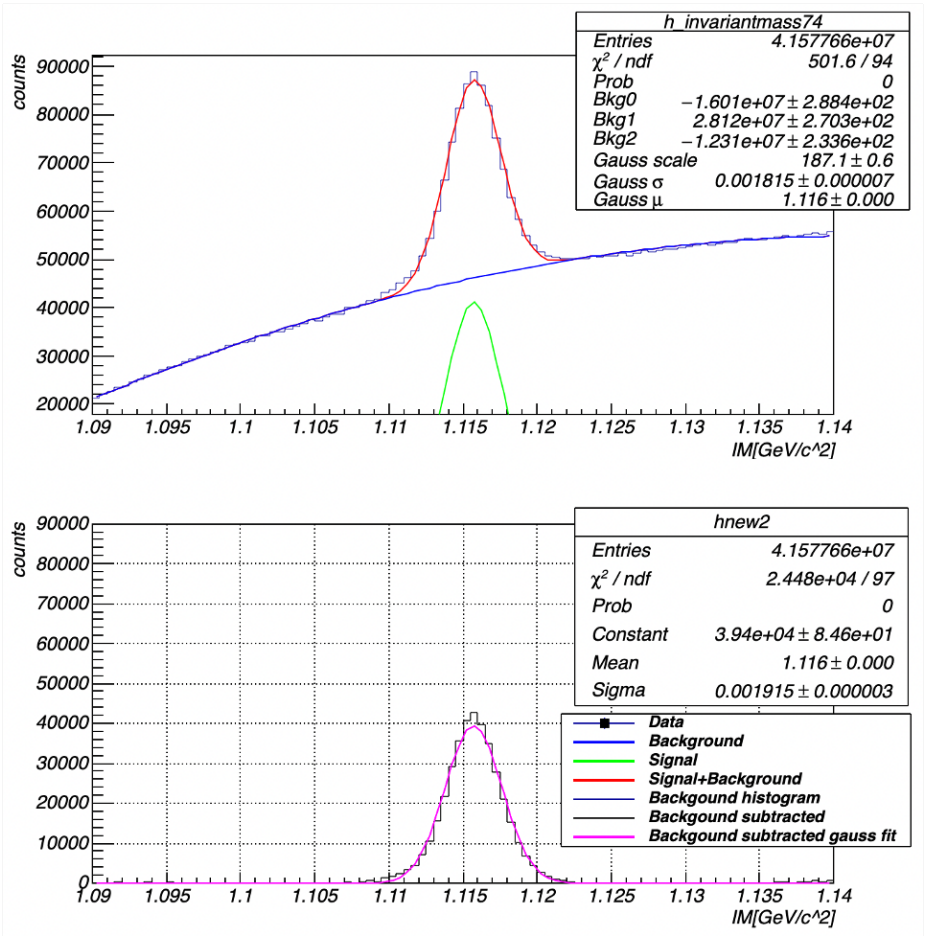

Figure A.12 Background subtraction on $IM_{p\pi^-}$ for the inclusive analysis using a fit to a Gaussian + second order polynomial functions for $p_\Lambda = [0.7, 0.8]$ GeV/c and $\theta_\Lambda = [0.7, 0.8]$ rad.

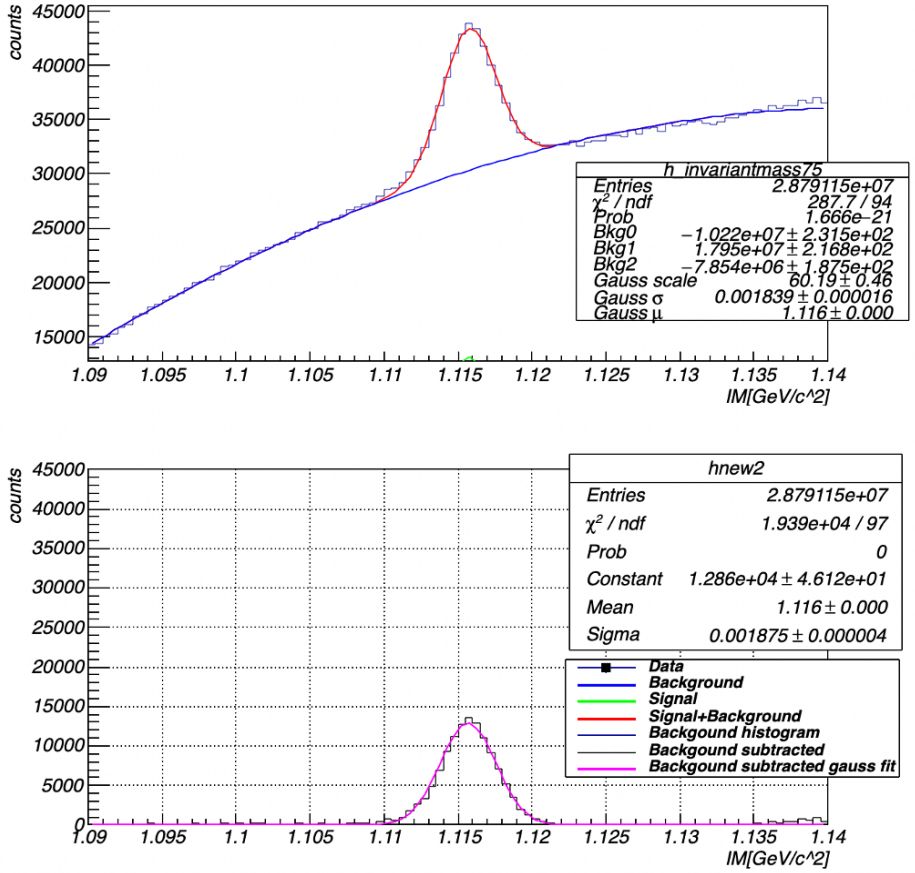

Figure A.13 Background subtraction on $IM_{p\pi^-}$ for the inclusive analysis using a fit to a Gaussian + second order polynomial functions for $p_\Lambda = [0.7, 0.8]$ GeV/c and $\theta_\Lambda = [0.8, 0.9]$ rad.

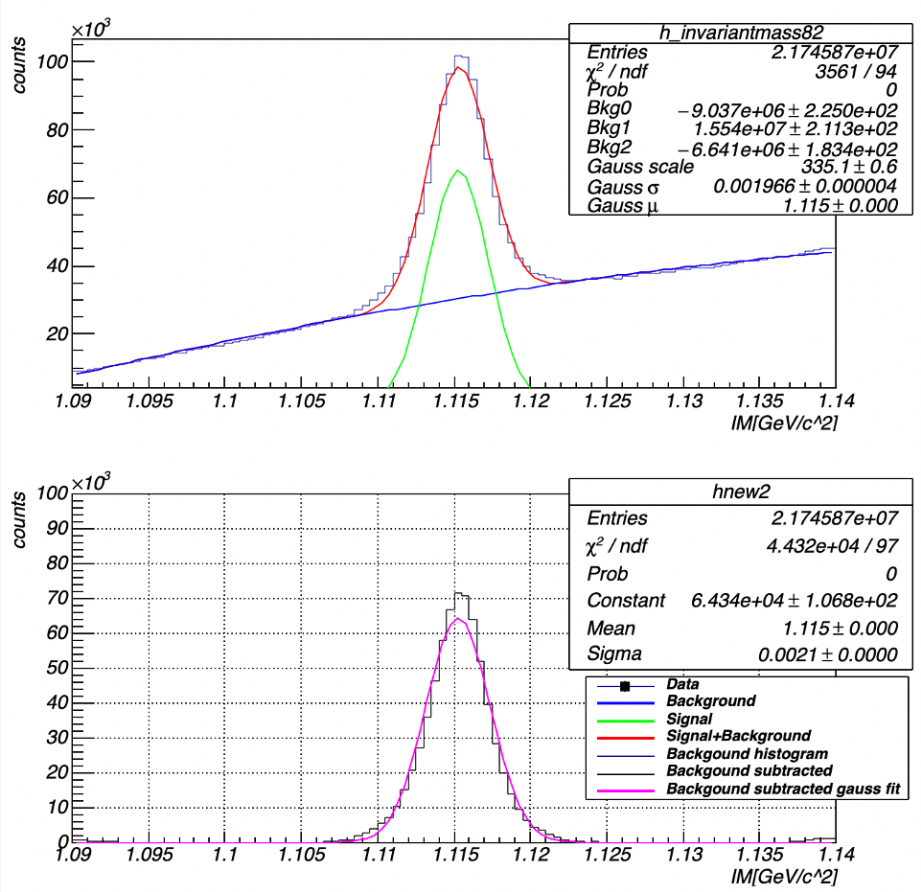

Figure A.14 Background subtraction on $IM_{p\pi^-}$ for the inclusive analysis using a fit to a Gaussian + second order polynomial functions for $p_\Lambda = [0.8, 0.9]$ GeV/c and $\theta_\Lambda = [0.3, 0.4]$ rad.

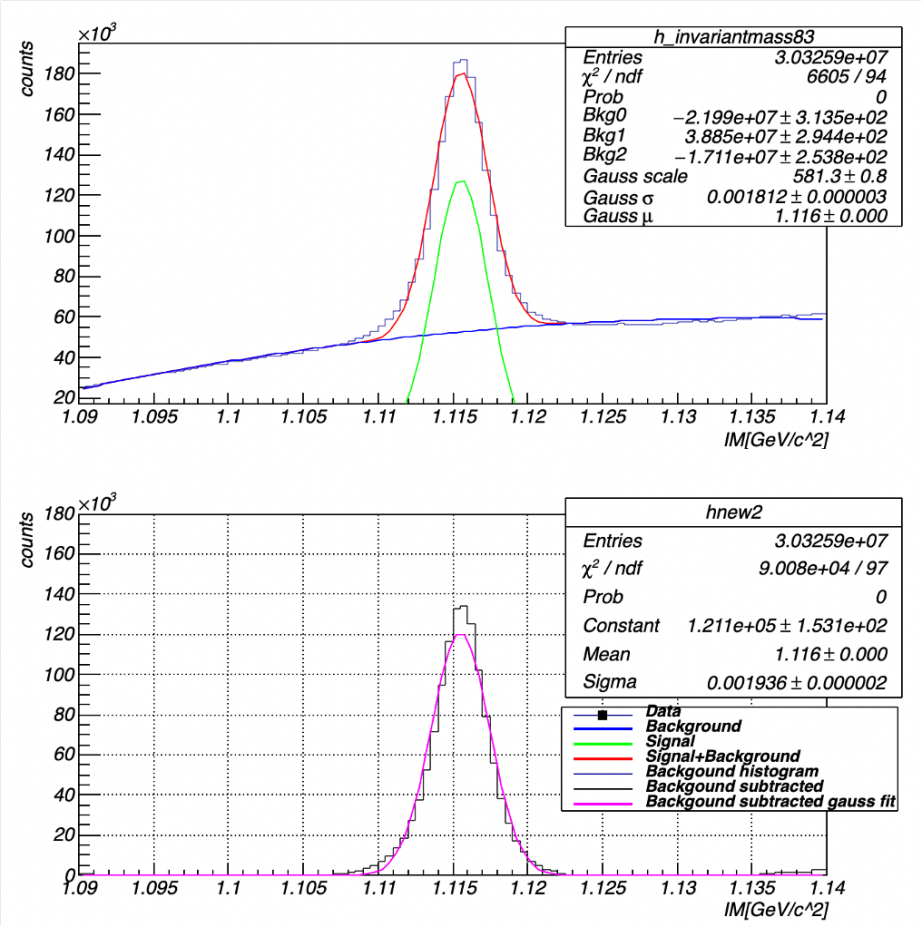

Figure A.15 Background subtraction on $IM_{p\pi^-}$ for the inclusive analysis using a fit to a Gaussian + second order polynomial functions for $p_\Lambda = [0.8, 0.9]$ GeV/c and $\theta_\Lambda = [0.4, 0.5]$ rad.

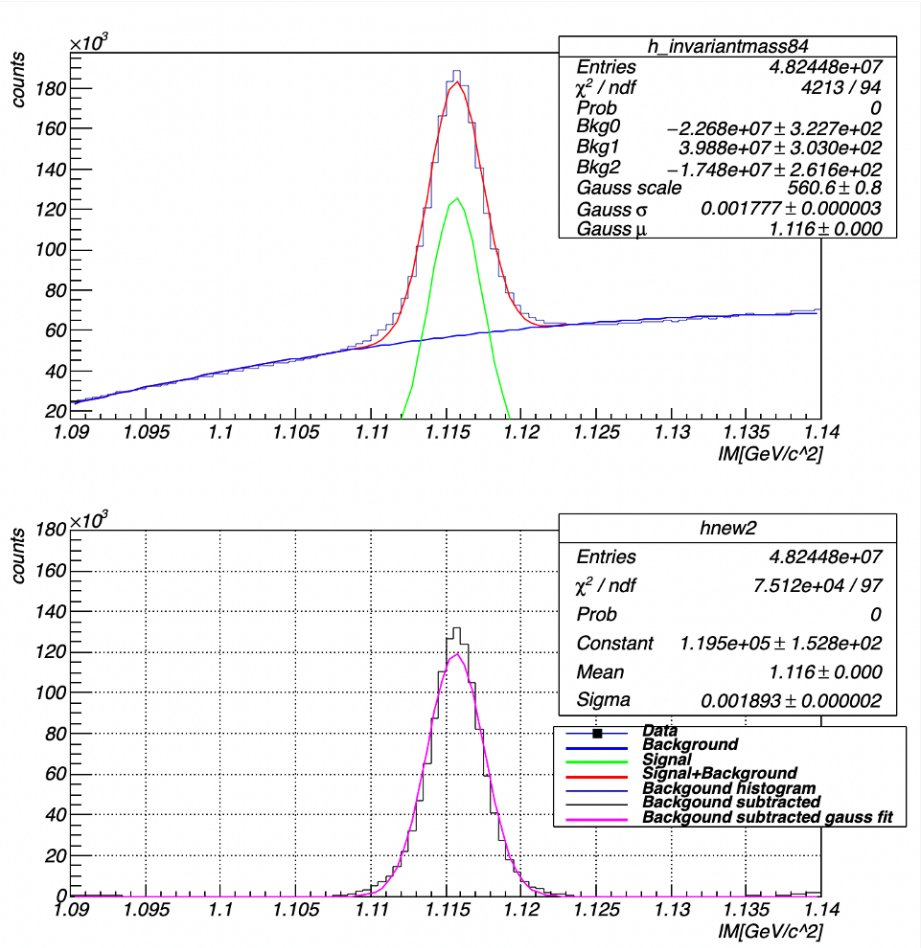

Figure A.16 Background subtraction on $IM_{p\pi^-}$ for the inclusive analysis using a fit to a Gaussian + second order polynomial functions for $p_\Lambda = [0.8, 0.9]$ GeV/c and $\theta_\Lambda = [0.5, 0.6]$ rad.

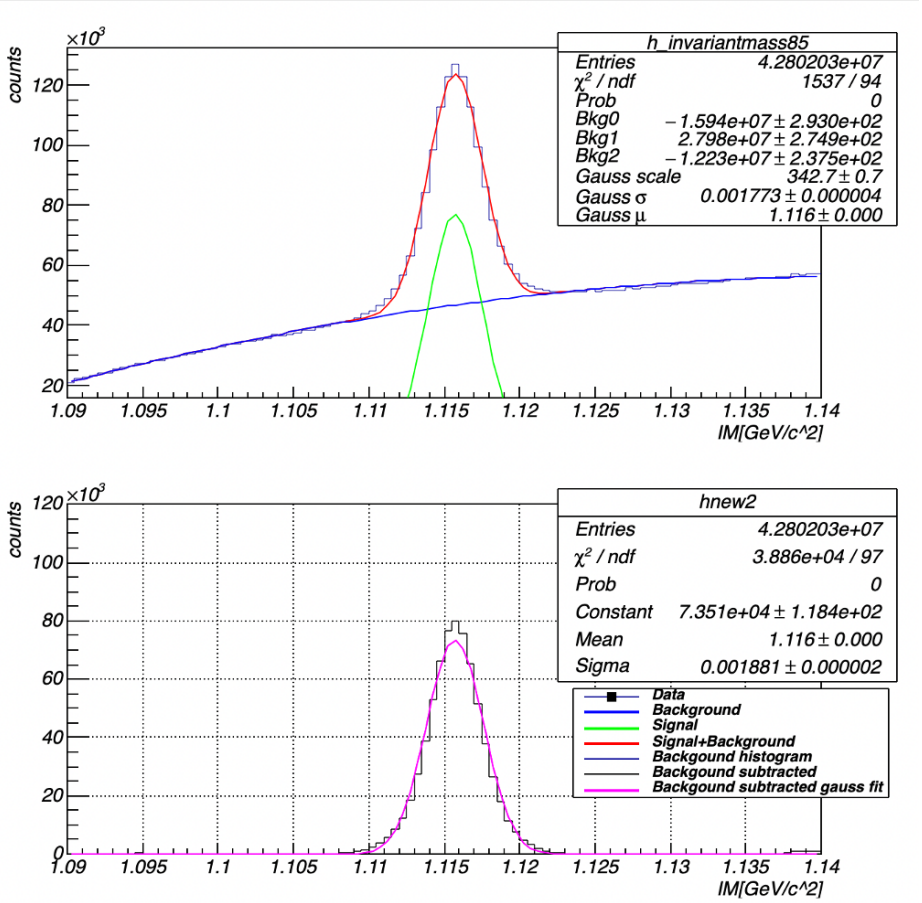

Figure A.17 Background subtraction on $IM_{p\pi^-}$ for the inclusive analysis using a fit to a Gaussian + second order polynomial functions for $p_\Lambda = [0.8, 0.9]$ GeV/c and $\theta_\Lambda = [0.6, 0.7]$ rad.

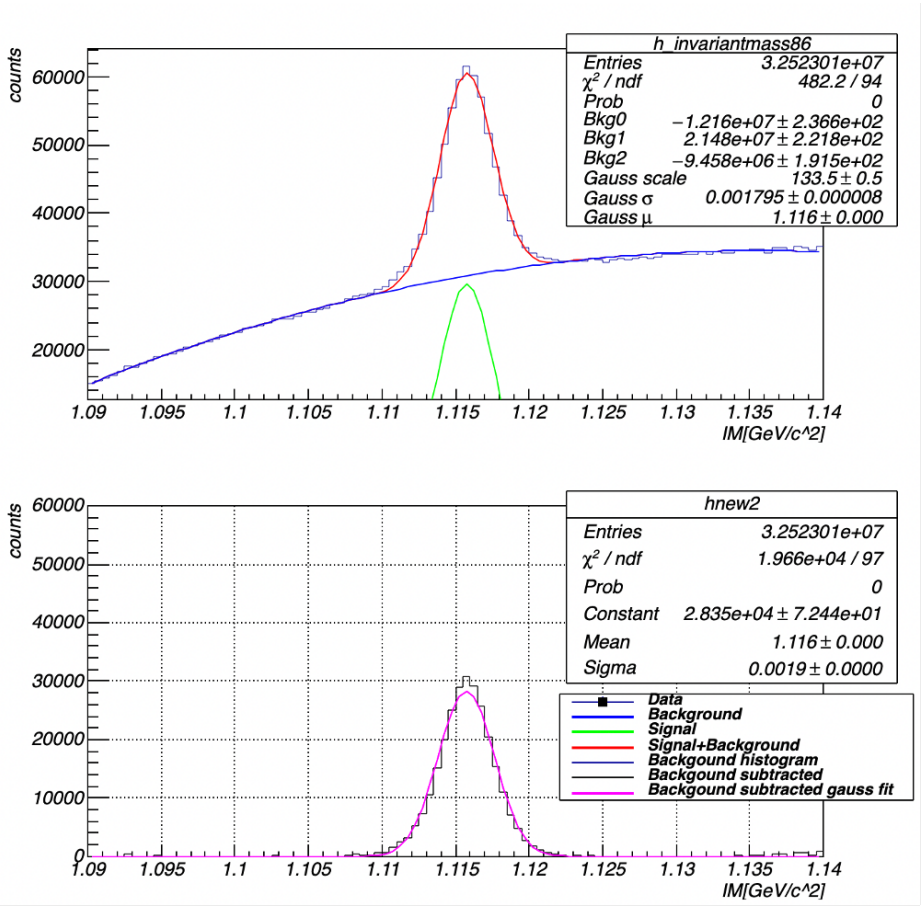

Figure A.18 Background subtraction on $IM_{p\pi^-}$ for the inclusive analysis using a fit to a Gaussian + second order polynomial functions for $p_\Lambda = [0.8, 0.9]$ GeV/c and $\theta_\Lambda = [0.7, 0.8]$ rad.

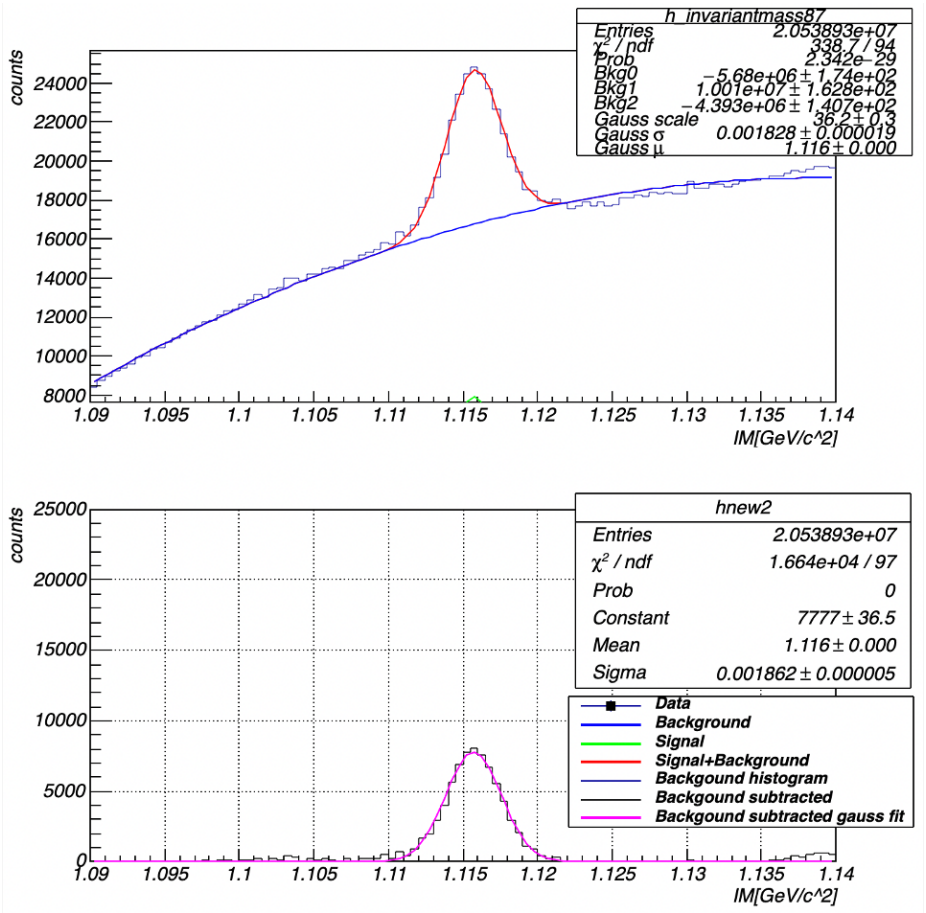

Figure A.19 Background subtraction on $IM_{p\pi^-}$ for the inclusive analysis using a fit to a Gaussian + second order polynomial functions for $p_\Lambda = [0.8, 0.9]$ GeV/c and $\theta_\Lambda = [0.8, 0.9]$ rad.

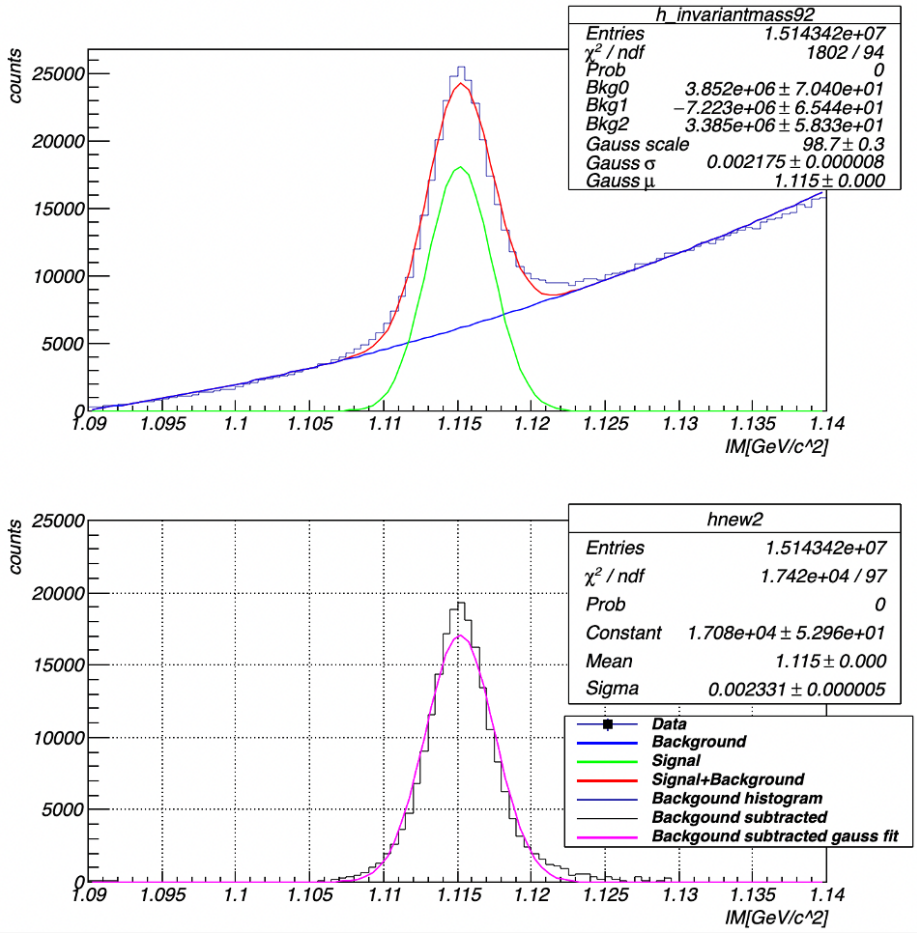

Figure A.20 Background subtraction on $IM_{p\pi^-}$ for the inclusive analysis using a fit to a Gaussian + second order polynomial functions for $p_\Lambda = [0.9, 1.0]$ GeV/c and $\theta_\Lambda = [0.2, 0.3]$ rad.

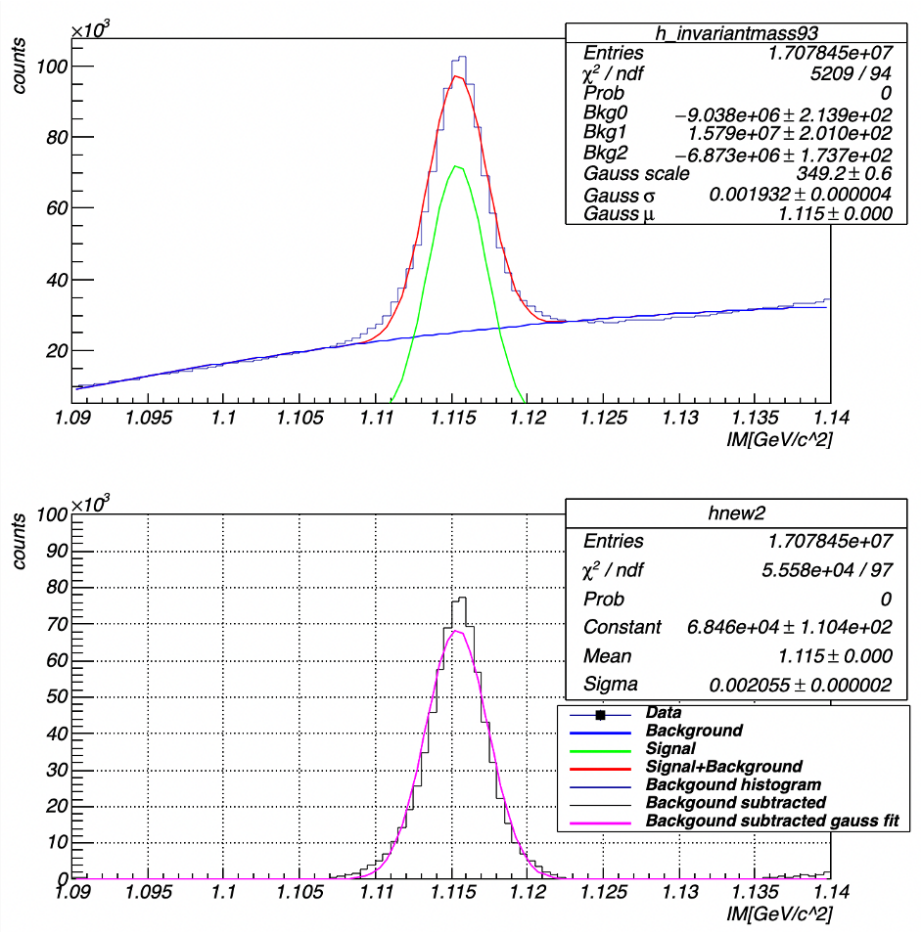

Figure A.21 Background subtraction on $IM_{p\pi^-}$ for the inclusive analysis using a fit to a Gaussian + second order polynomial functions for $p_\Lambda = [0.9, 1.0]$ GeV/c and $\theta_\Lambda = [0.3, 0.4]$ rad.

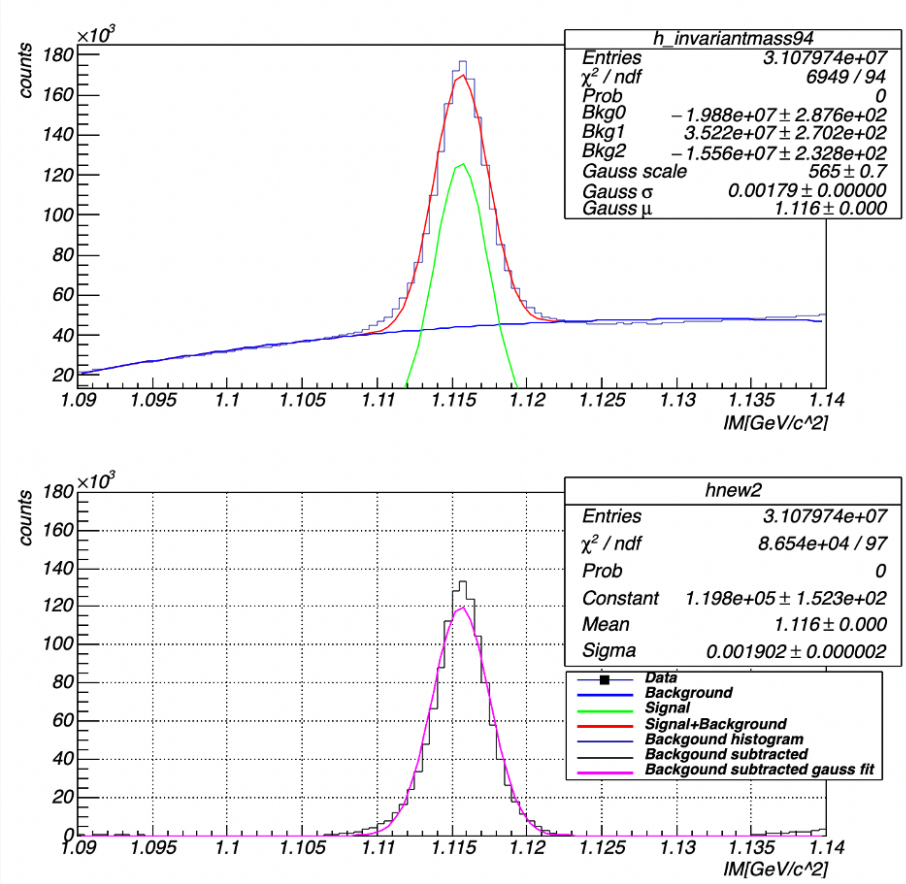

Figure A.22 Background subtraction on $IM_{p\pi^-}$ for the inclusive analysis using a fit to a Gaussian + second order polynomial functions for $p_\Lambda = [0.9, 1.0]$ GeV/c and $\theta_\Lambda = [0.4, 0.5]$ rad.

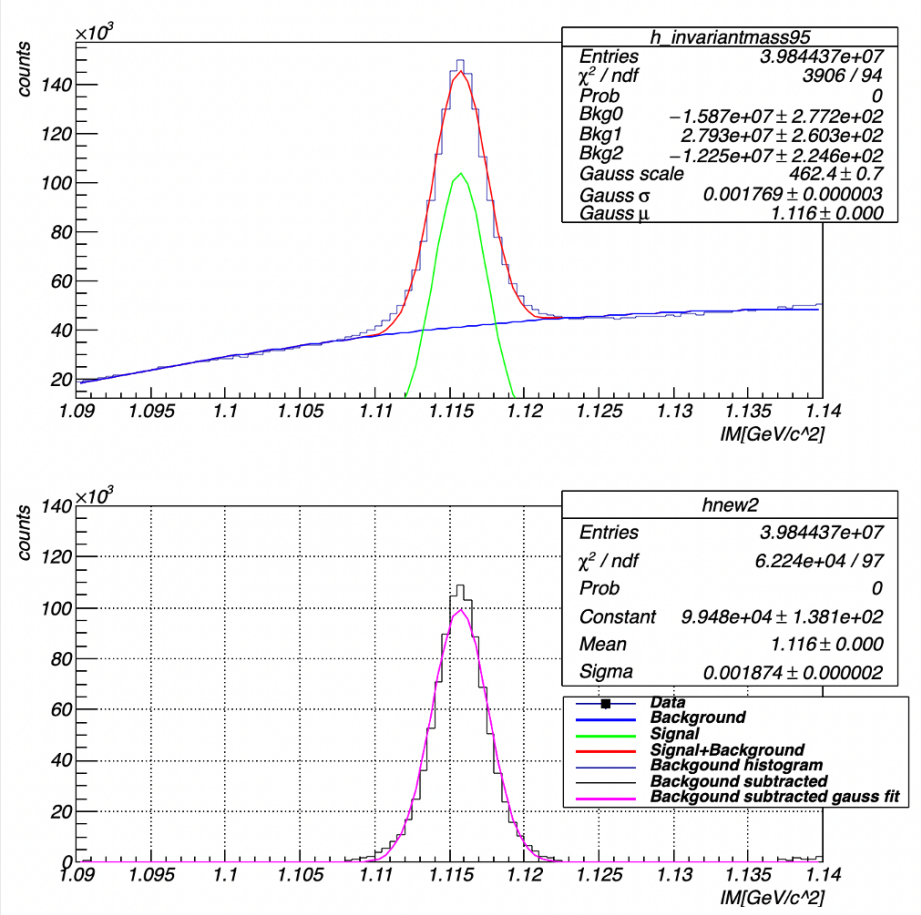

Figure A.23 Background subtraction on $IM_{p\pi^-}$ for the inclusive analysis using a fit to a Gaussian + second order polynomial functions for $p_\Lambda = [0.9, 1.0]$ GeV/c and $\theta_\Lambda = [0.5, 0.6]$ rad.

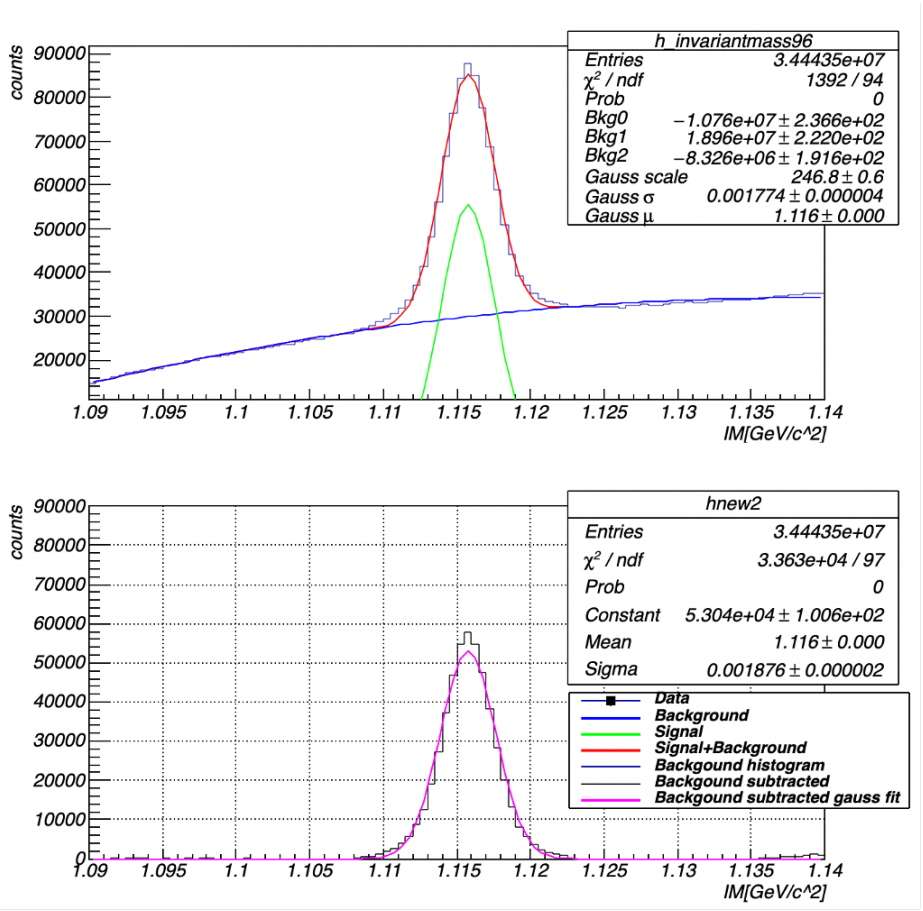

Figure A.24 Background subtraction on $IM_{p\pi^-}$ for the inclusive analysis using a fit to a Gaussian + second order polynomial functions for $p_\Lambda = [0.9, 1.0]$ GeV/c and $\theta_\Lambda = [0.6, 0.7]$ rad.

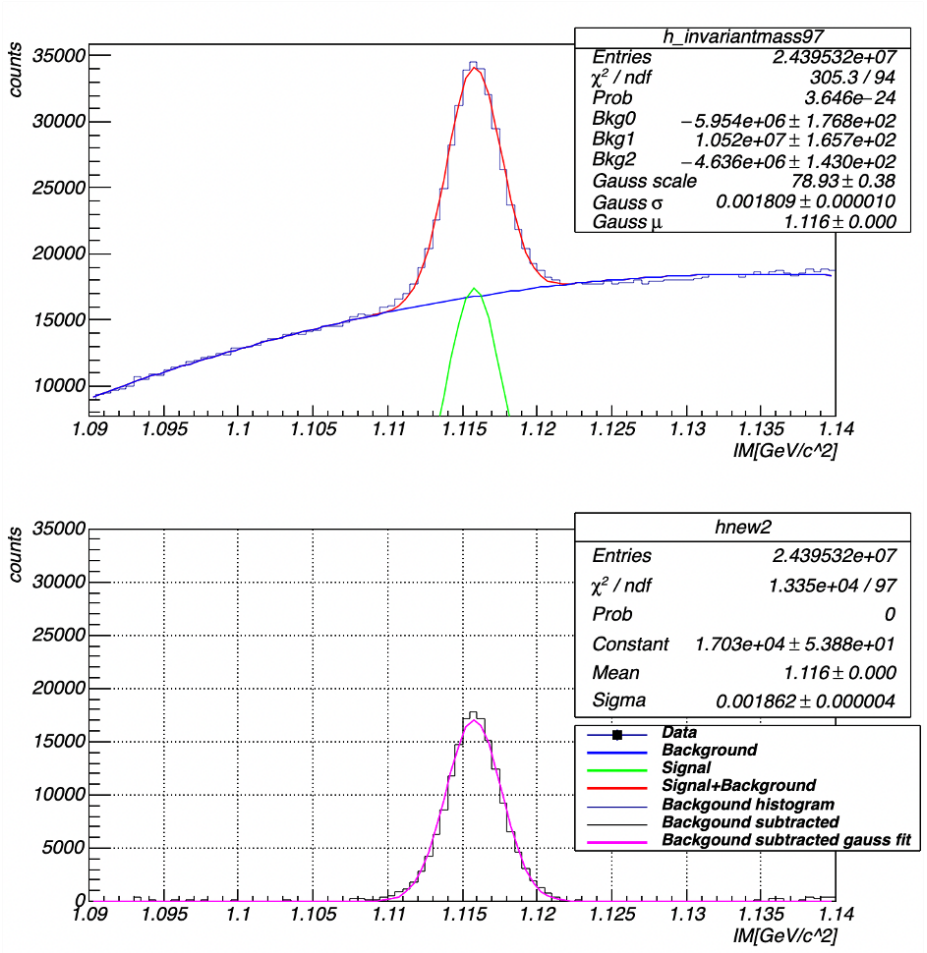

Figure A.25 Background subtraction on $IM_{p\pi^-}$ for the inclusive analysis using a fit to a Gaussian + second order polynomial functions for $p_\Lambda = [0.9, 1.0]$ GeV/c and $\theta_\Lambda = [0.7, 0.8]$ rad.

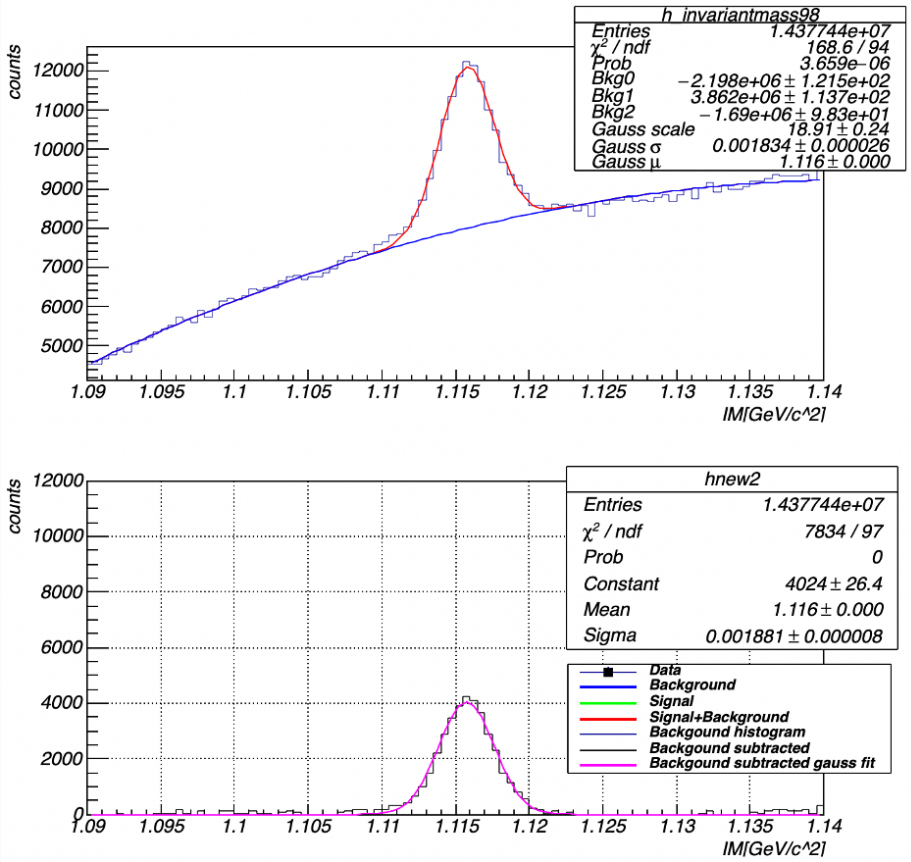

Figure A.26 Background subtraction on $IM_{p\pi^-}$ for the inclusive analysis using a fit to a Gaussian + second order polynomial functions for $p_\Lambda = [0.9, 1.0]$ GeV/c and $\theta_\Lambda = [0.8, 0.9]$ rad.

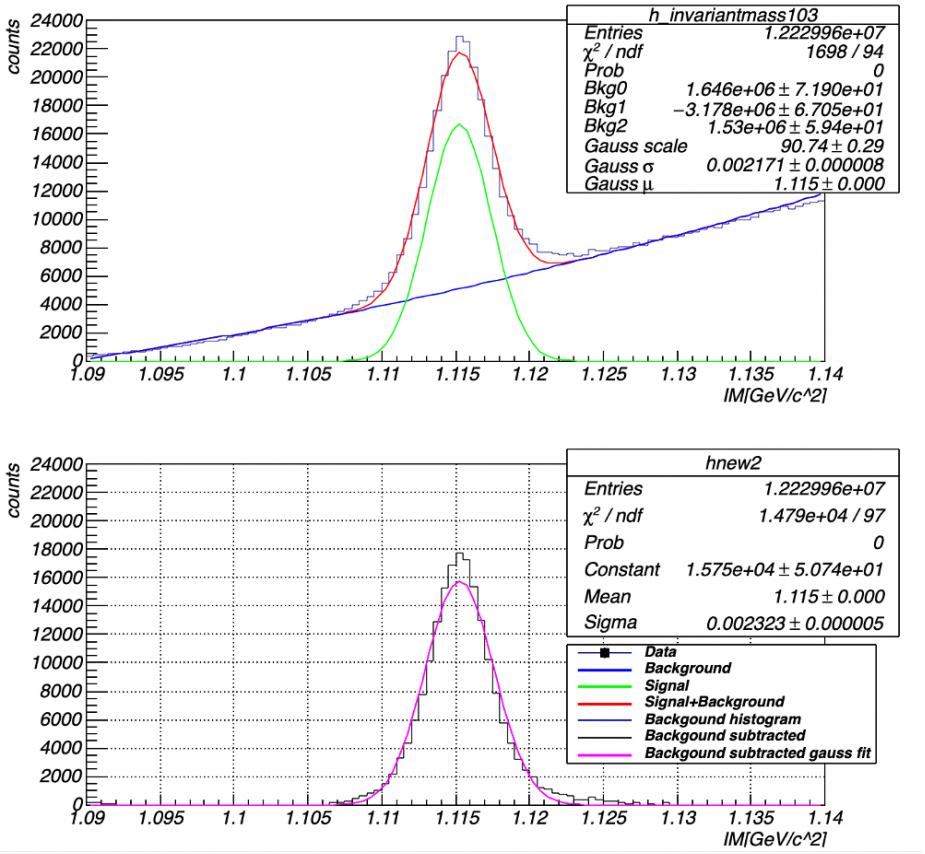

Figure A.27 Background subtraction on $IM_{p\pi^-}$ for the inclusive analysis using a fit to a Gaussian + second order polynomial functions for $p_\Lambda = [1.0, 1.1]$ GeV/c and $\theta_\Lambda = [0.2, 0.3]$ rad.

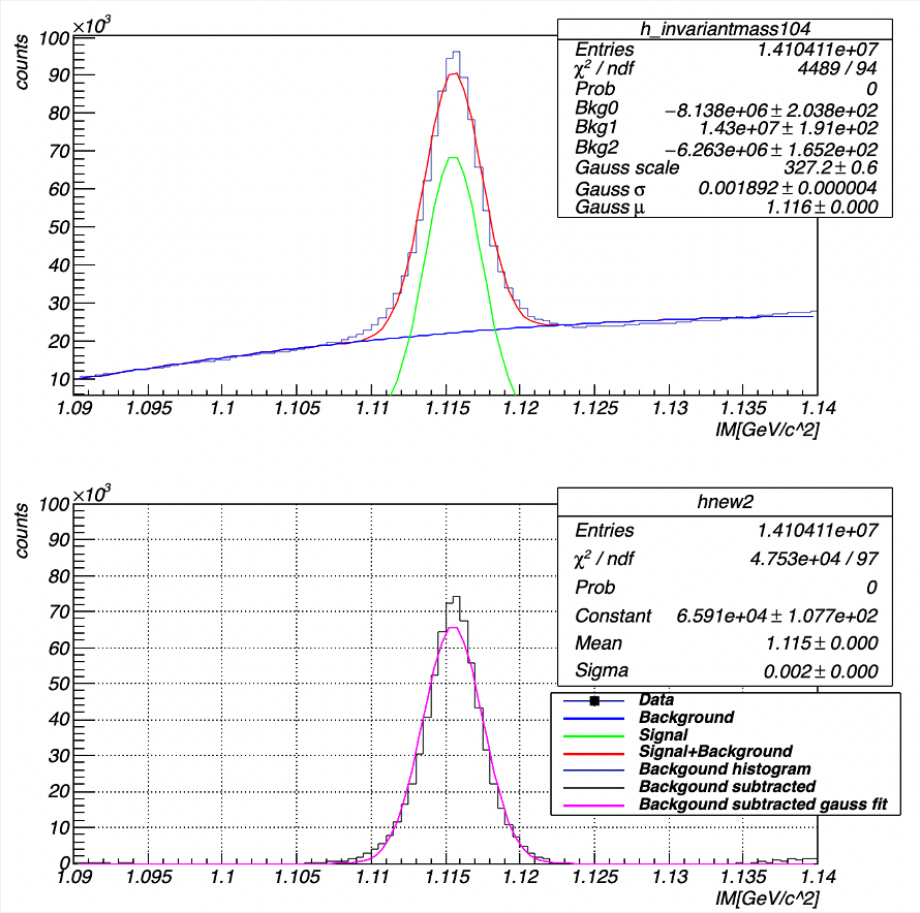

Figure A.28 Background subtraction on $IM_{p\pi^-}$ for the inclusive analysis using a fit to a Gaussian + second order polynomial functions for $p_\Lambda = [1.0, 1.1]$ GeV/c and $\theta_\Lambda = [0.3, 0.4]$ rad.

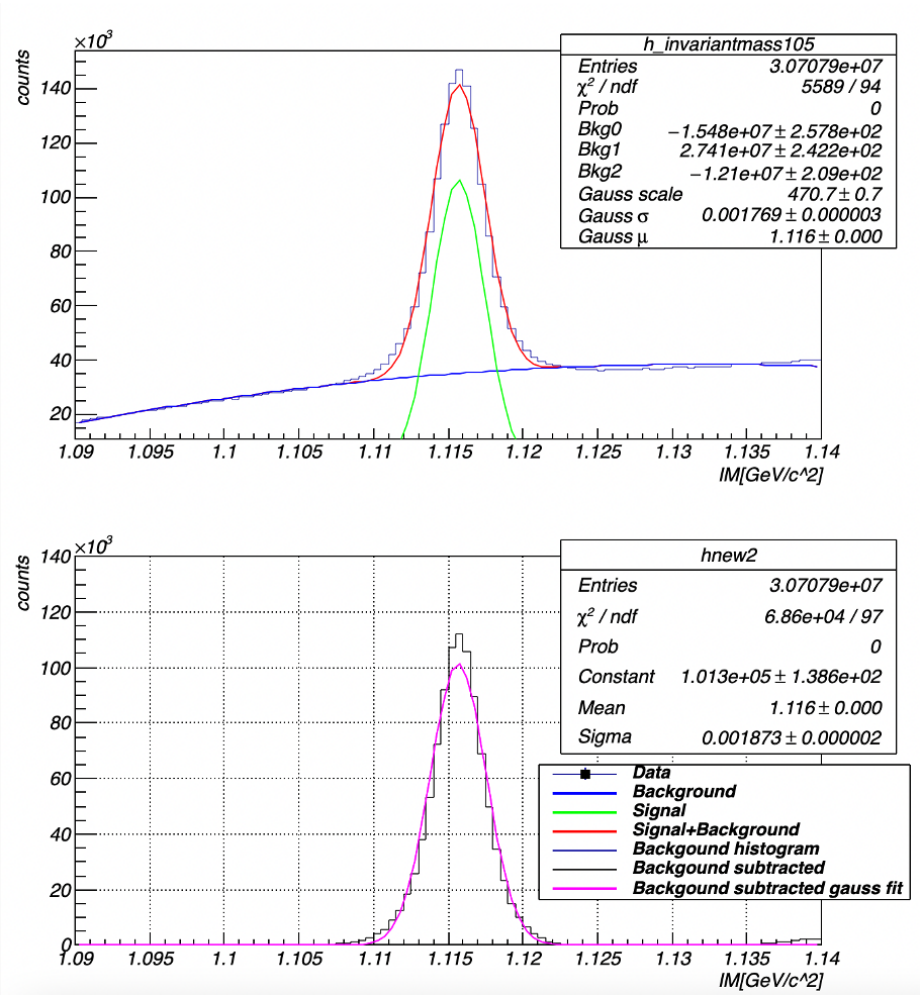

Figure A.29 Background subtraction on $IM_{p\pi^-}$ for the inclusive analysis using a fit to a Gaussian + second order polynomial functions for $p_\Lambda = [1.0, 1.1]$ GeV/c and $\theta_\Lambda = [0.4, 0.5]$ rad.

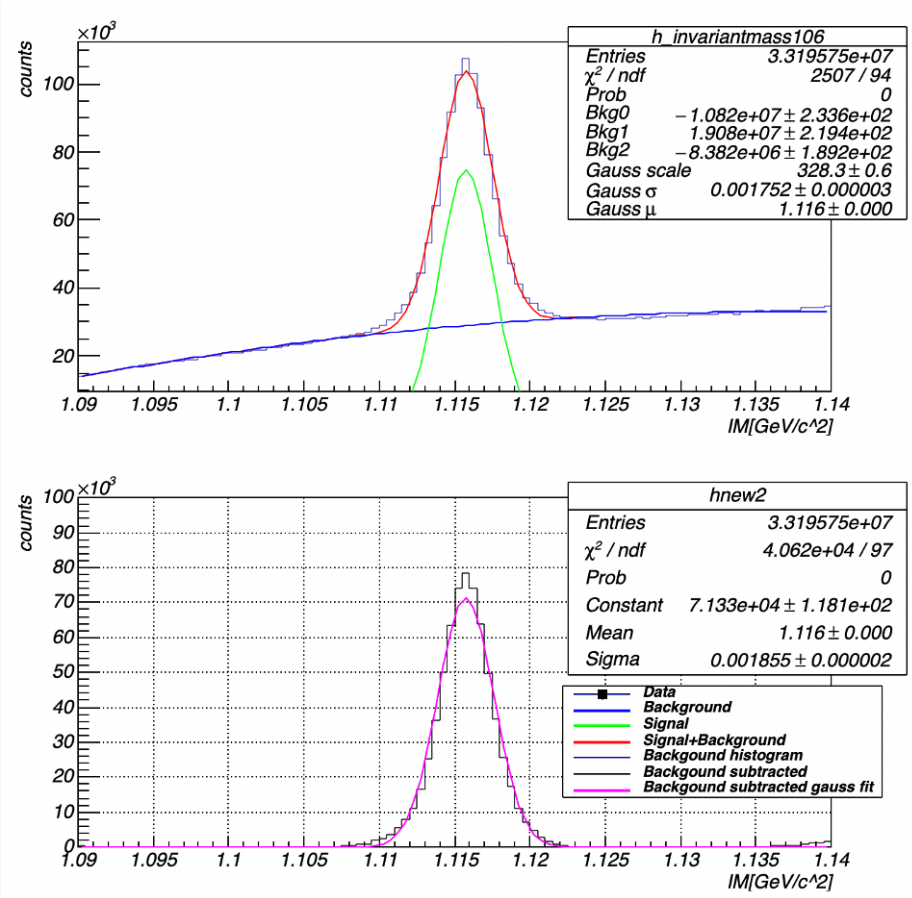

Figure A.30 Background subtraction on $IM_{p\pi^-}$ for the inclusive analysis using a fit to a Gaussian + second order polynomial functions for $p_\Lambda = [1.0, 1.1]$ GeV/c and $\theta_\Lambda = [0.5, 0.6]$ rad.

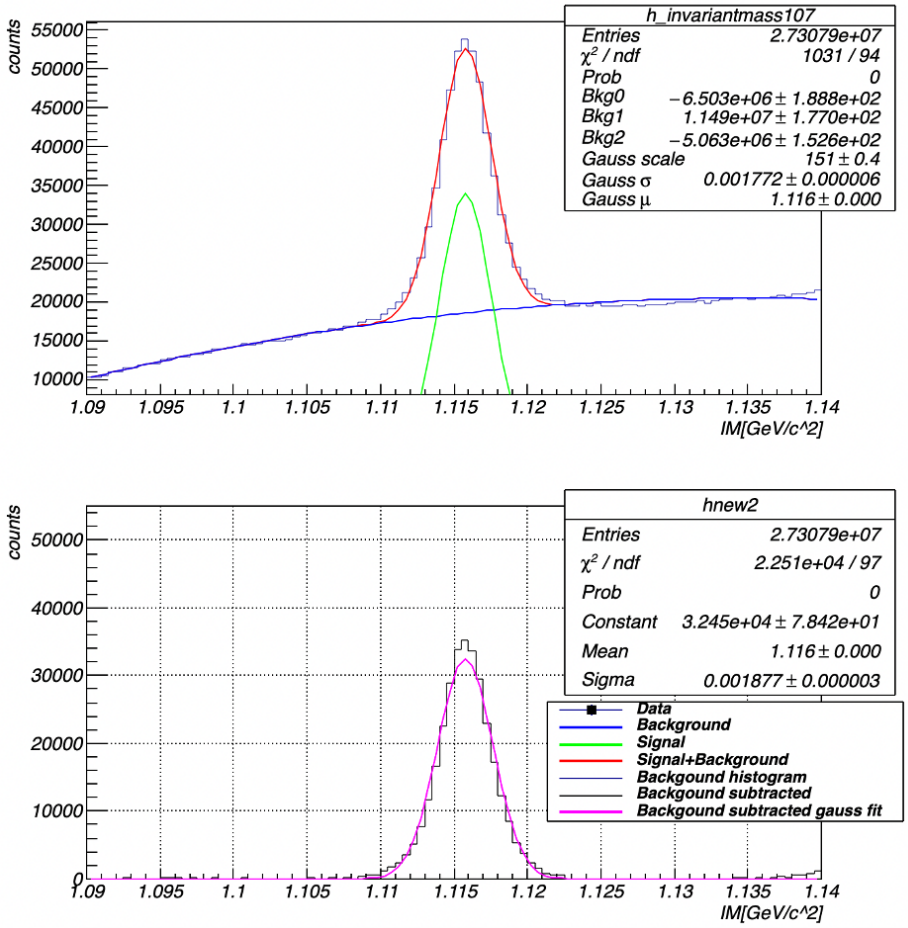

Figure A.31 Background subtraction on $IM_{p\pi^-}$ for the inclusive analysis using a fit to a Gaussian + second order polynomial functions for $p_\Lambda = [1.0, 1.1]$ GeV/c and $\theta_\Lambda = [0.6, 0.7]$ rad.

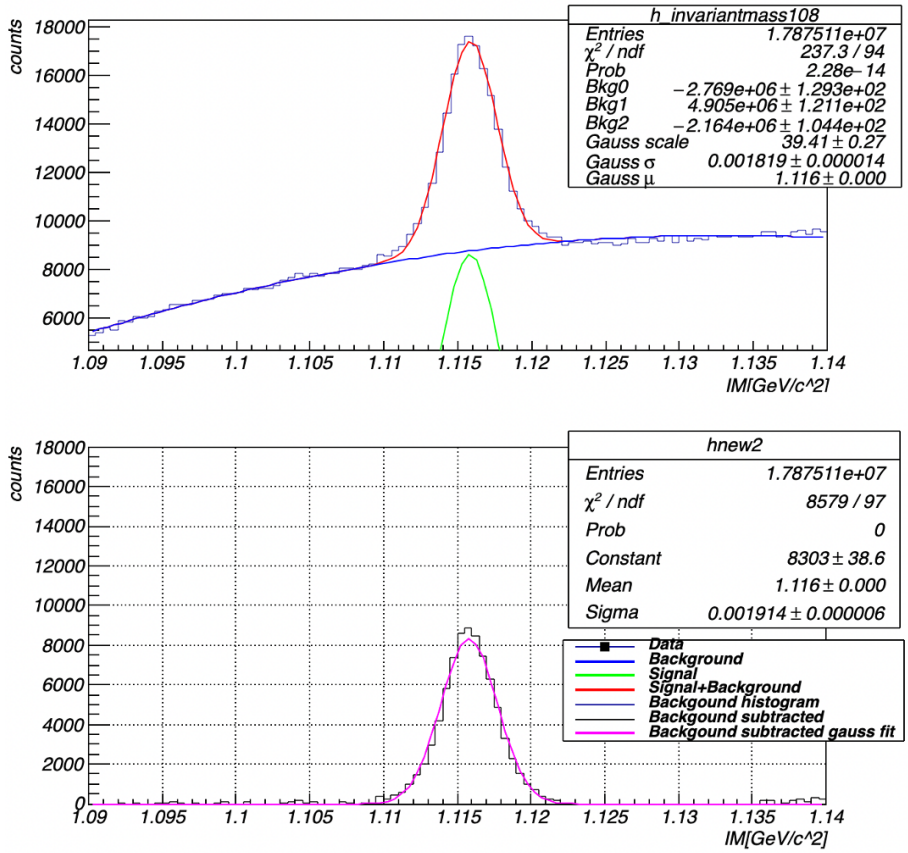

Figure A.32 Background subtraction on $IM_{p\pi^-}$ for the inclusive analysis using a fit to a Gaussian + second order polynomial functions for $p_\Lambda = [1.0, 1.1]$ GeV/c and $\theta_\Lambda = [0.7, 0.8]$ rad.

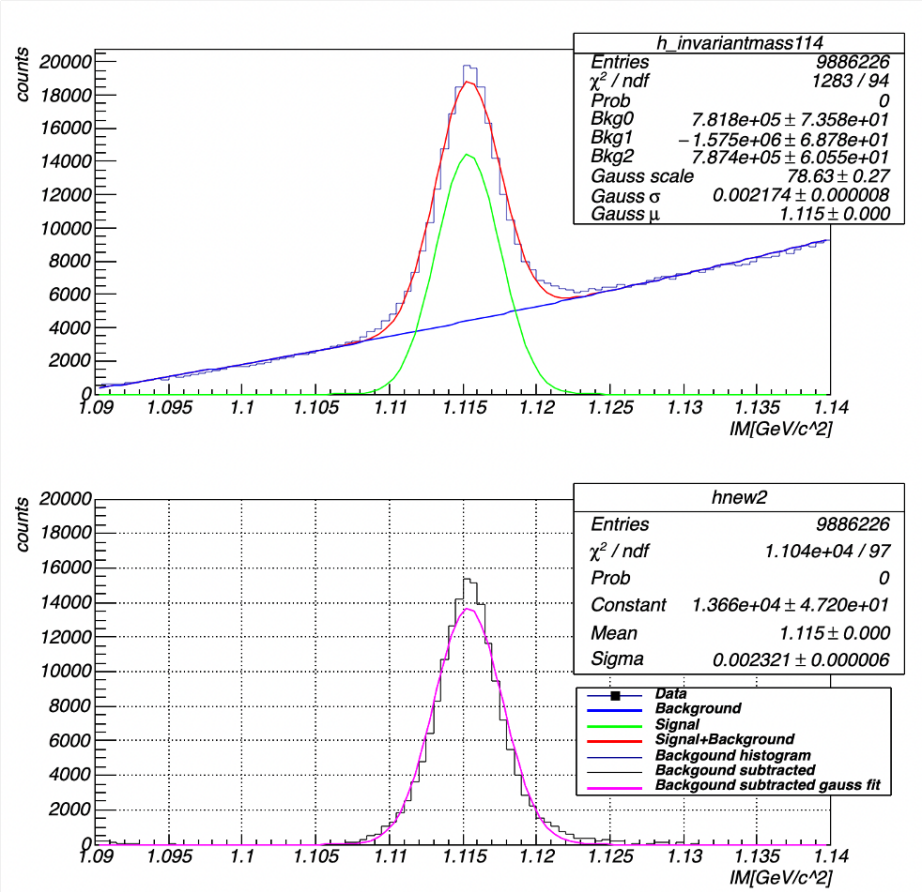

Figure A.33 Background subtraction on $IM_{p\pi^-}$ for the inclusive analysis using a fit to a Gaussian + second order polynomial functions for $p_\Lambda = [1.1, 1.2]$ GeV/c and $\theta_\Lambda = [0.2, 0.3]$ rad.

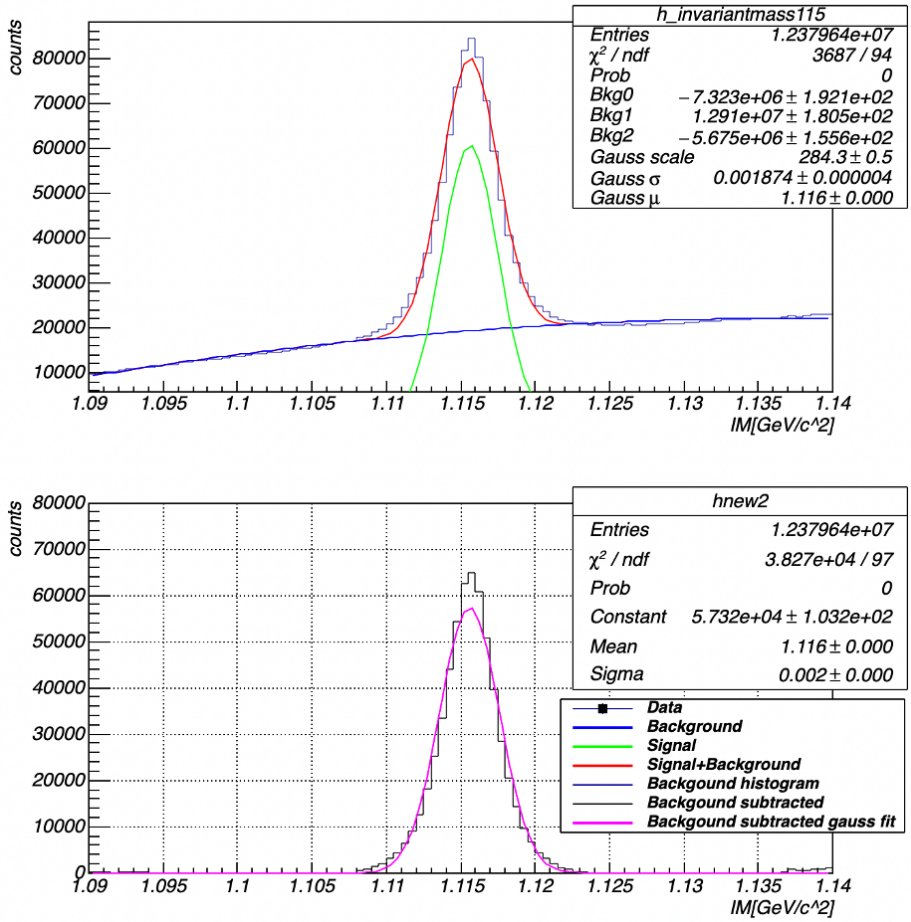

Figure A.34 Background subtraction on $IM_{p\pi^-}$ for the inclusive analysis using a fit to a Gaussian + second order polynomial functions for $p_\Lambda = [1.1, 1.2]$ GeV/c and $\theta_\Lambda = [0.3, 0.4]$ rad.

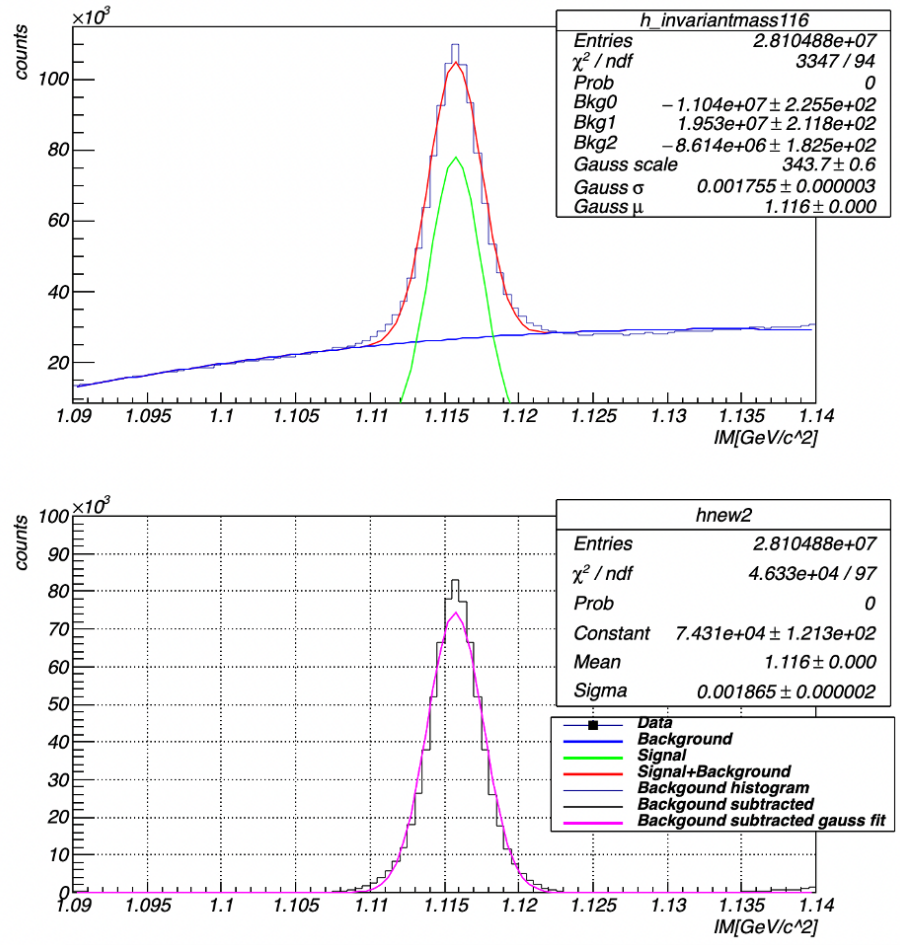

Figure A.35 Background subtraction on $IM_{p\pi^-}$ for the inclusive analysis using a fit to a Gaussian + second order polynomial functions for $p_\Lambda = [1.1, 1.2]$ GeV/c and $\theta_\Lambda = [0.4, 0.5]$ rad.

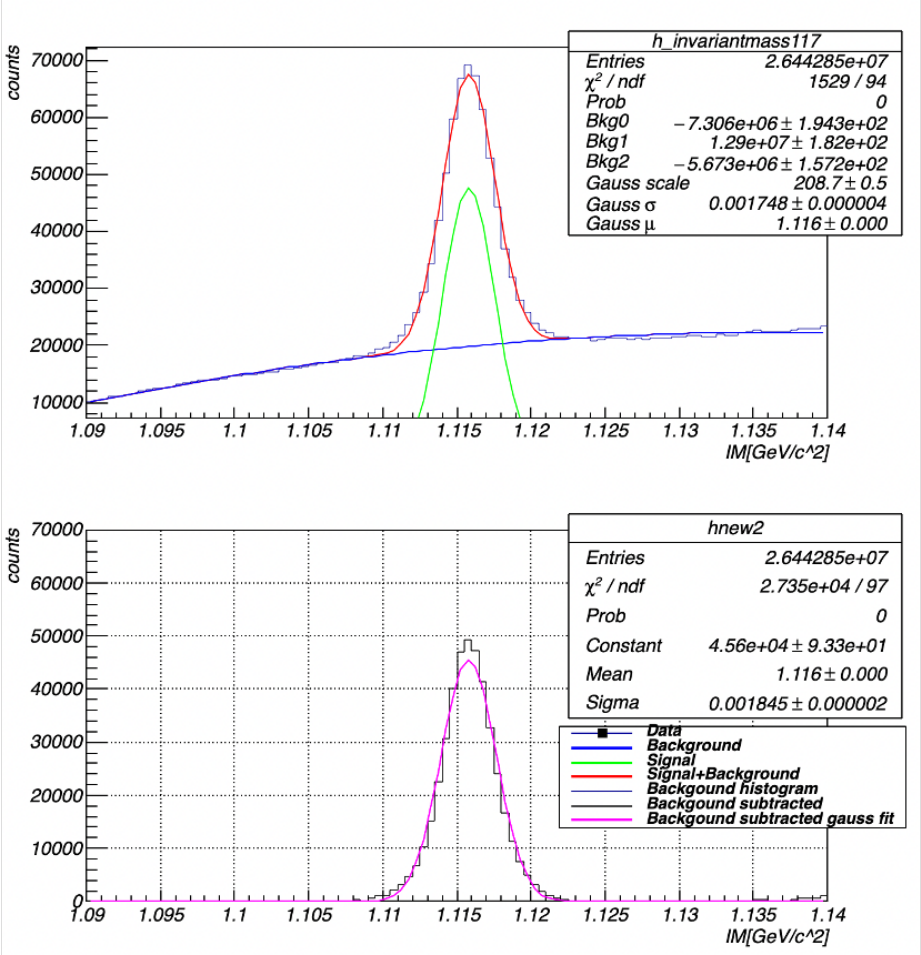

Figure A.36 Background subtraction on $IM_{p\pi^-}$ for the inclusive analysis using a fit to a Gaussian + second order polynomial functions for $p_\Lambda = [1.1, 1.2]$ GeV/c and $\theta_\Lambda = [0.5, 0.6]$ rad.

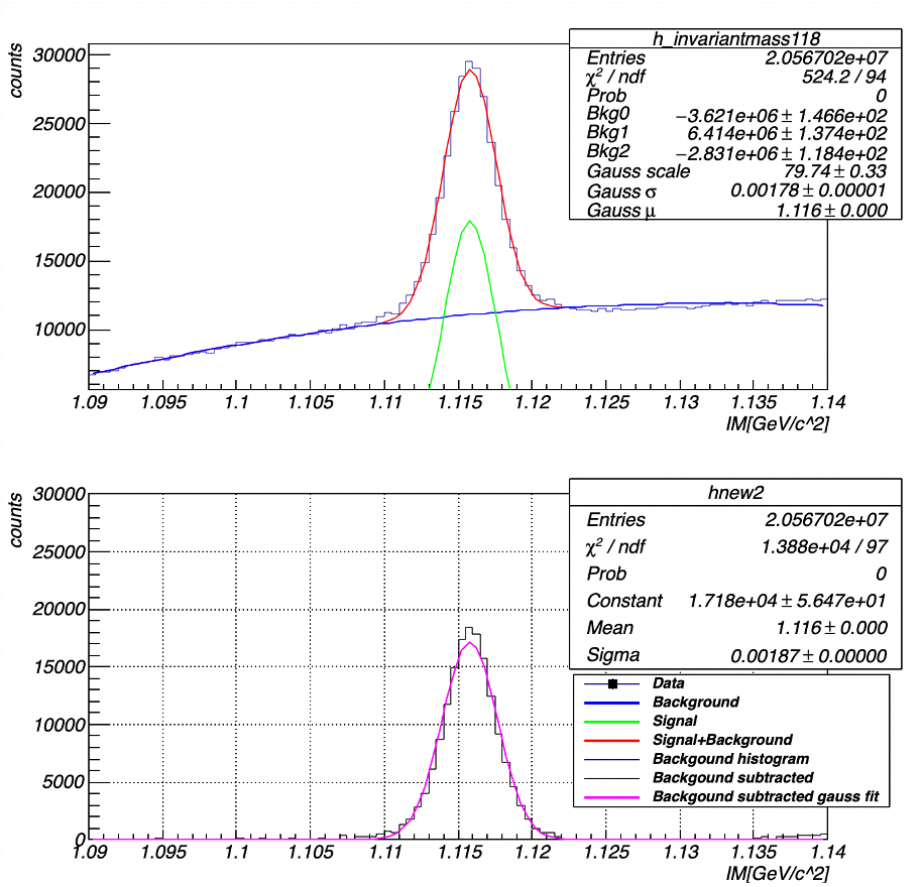

Figure A.37 Background subtraction on $IM_{p\pi^-}$ for the inclusive analysis using a fit to a Gaussian + second order polynomial functions for $p_\Lambda = [1.1, 1.2]$ GeV/c and $\theta_\Lambda = [0.6, 0.7]$ rad.

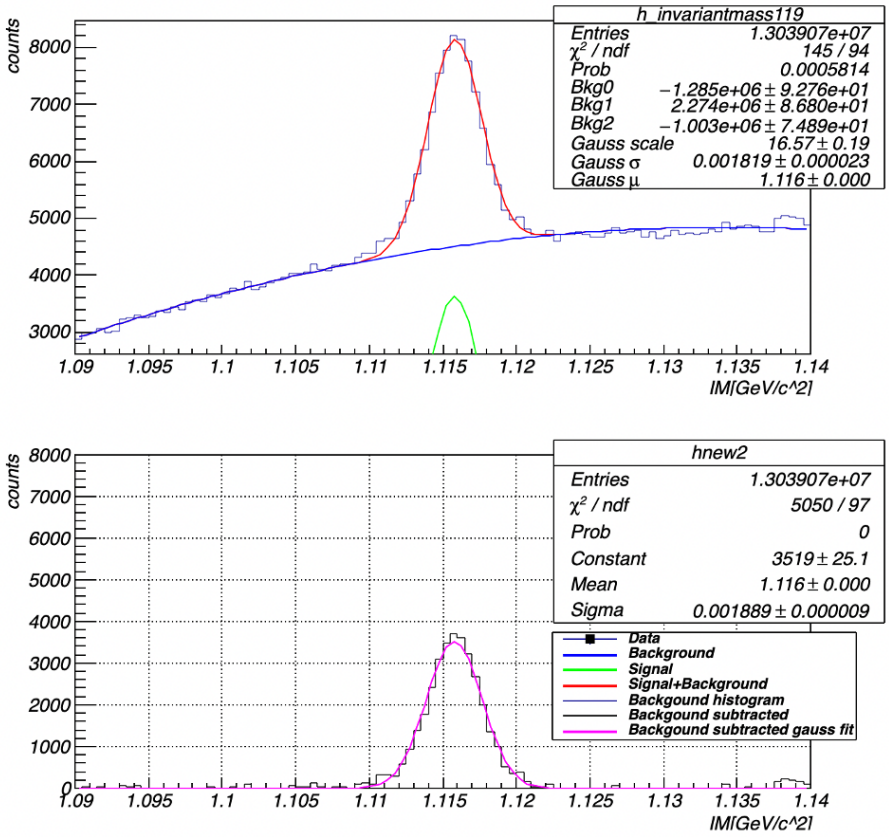

Figure A.38 Background subtraction on $IM_{p\pi^-}$ for the inclusive analysis using a fit to a Gaussian + second order polynomial functions for $p_\Lambda = [1.1, 1.2]$ GeV/c and $\theta_\Lambda = [0.7, 0.8]$ rad.

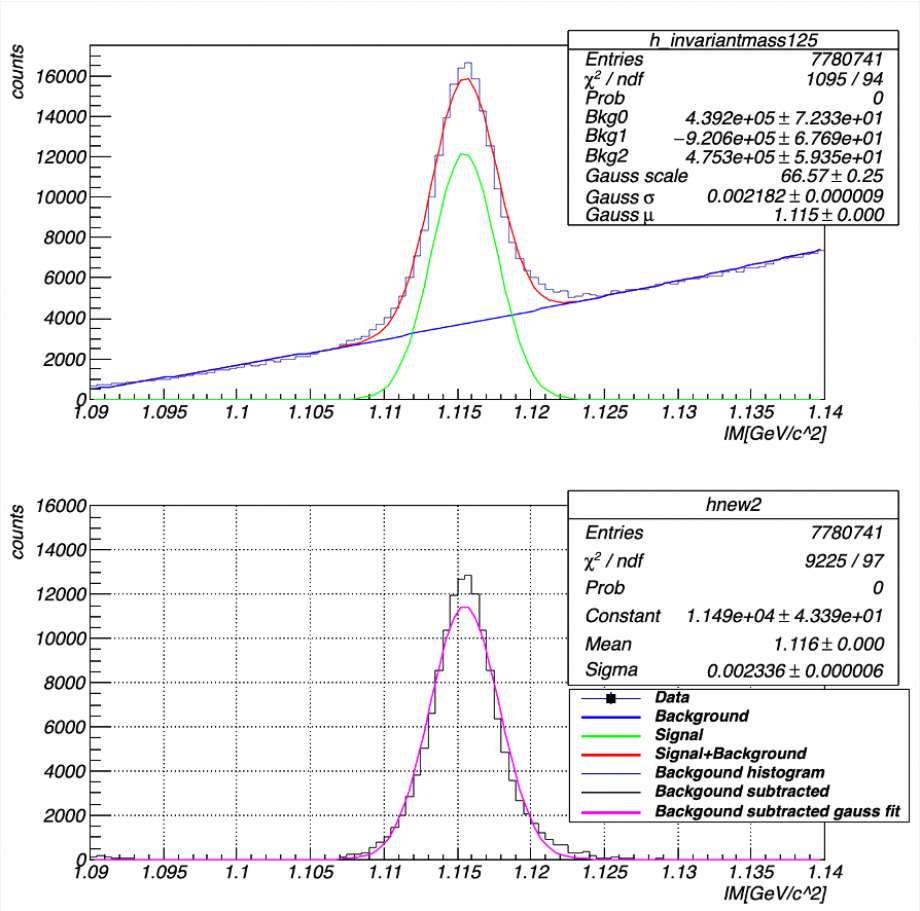

Figure A.39 Background subtraction on $IM_{p\pi^-}$ for the inclusive analysis using a fit to a Gaussian + second order polynomial functions for $p_\Lambda = [1.2, 1.3]$ GeV/c and $\theta_\Lambda = [0.2, 0.3]$ rad.

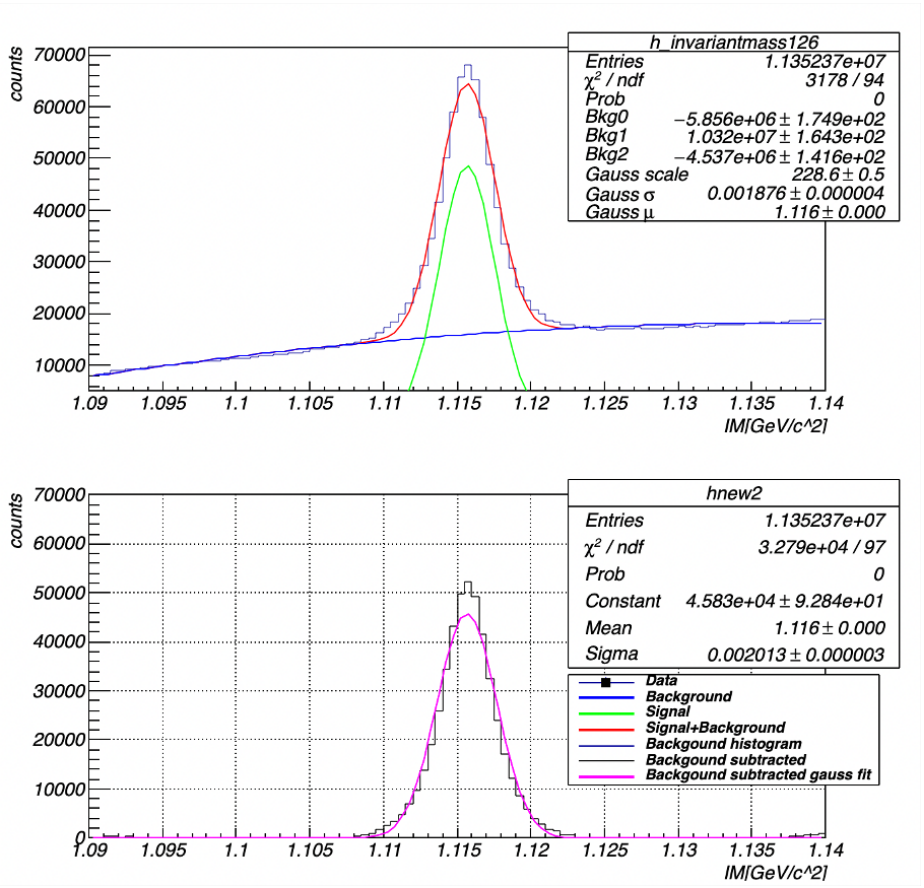

Figure A.40 Background subtraction on $IM_{p\pi^-}$ for the inclusive analysis using a fit to a Gaussian + second order polynomial functions for $p_\Lambda = [1.2, 1.3]$ GeV/c and $\theta_\Lambda = [0.3, 0.4]$ rad.

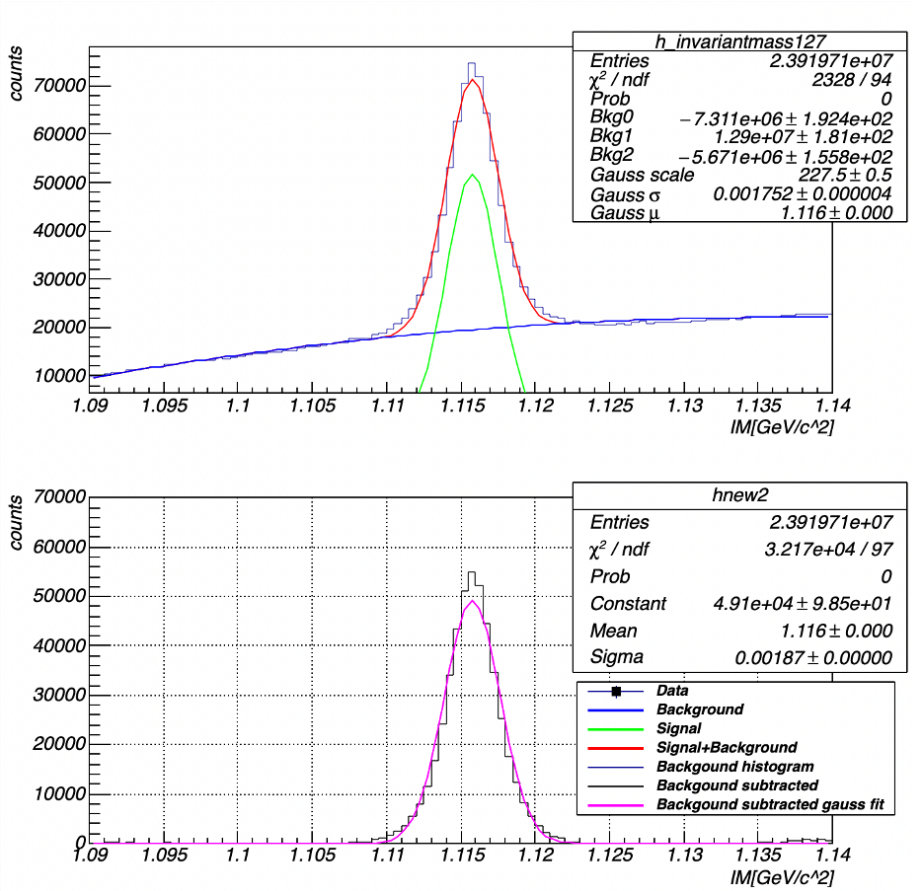

Figure A.41 Background subtraction on $IM_{p\pi^-}$ for the inclusive analysis using a fit to a Gaussian + second order polynomial functions for $p_\Lambda = [1.2, 1.3]$ GeV/c and $\theta_\Lambda = [0.4, 0.5]$ rad.

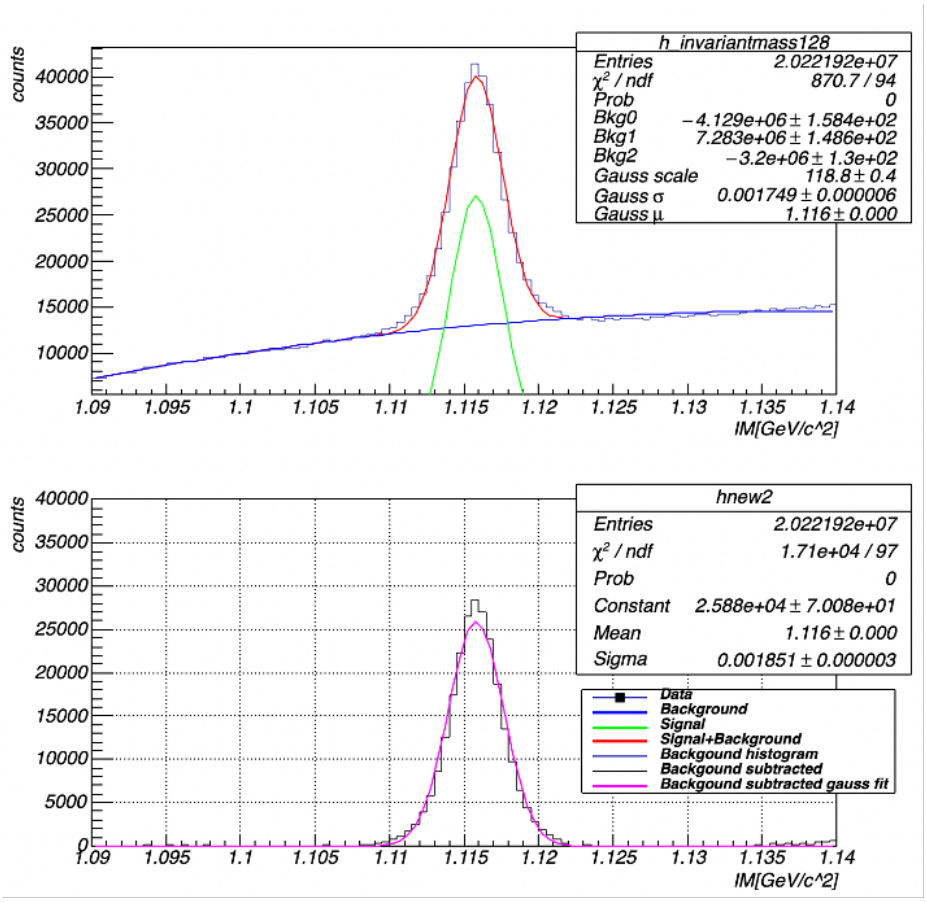

Figure A.42 Background subtraction on $IM_{p\pi^-}$ for the inclusive analysis using a fit to a Gaussian + second order polynomial functions for $p_\Lambda = [1.2, 1.3]$ GeV/c and $\theta_\Lambda = [0.5, 0.6]$ rad.

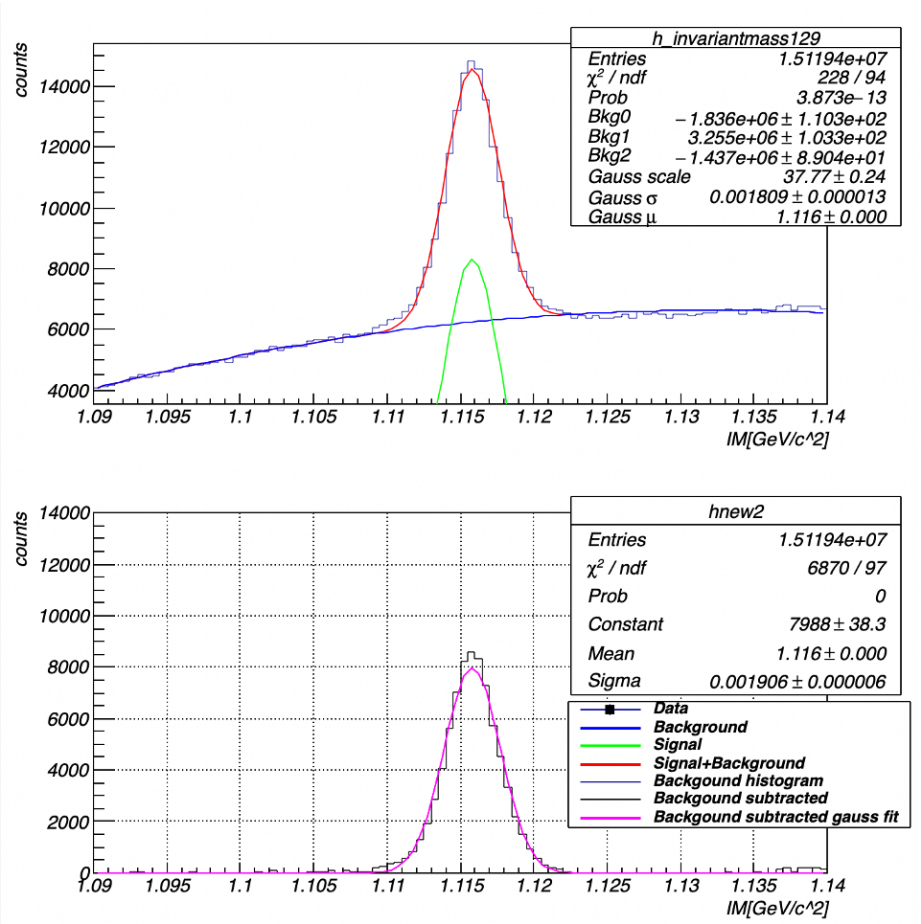

Figure A.43 Background subtraction on $IM_{p\pi^-}$ for the inclusive analysis using a fit to a Gaussian + second order polynomial functions for $p_\Lambda = [1.2, 1.3]$ GeV/c and $\theta_\Lambda = [0.6, 0.7]$ rad.

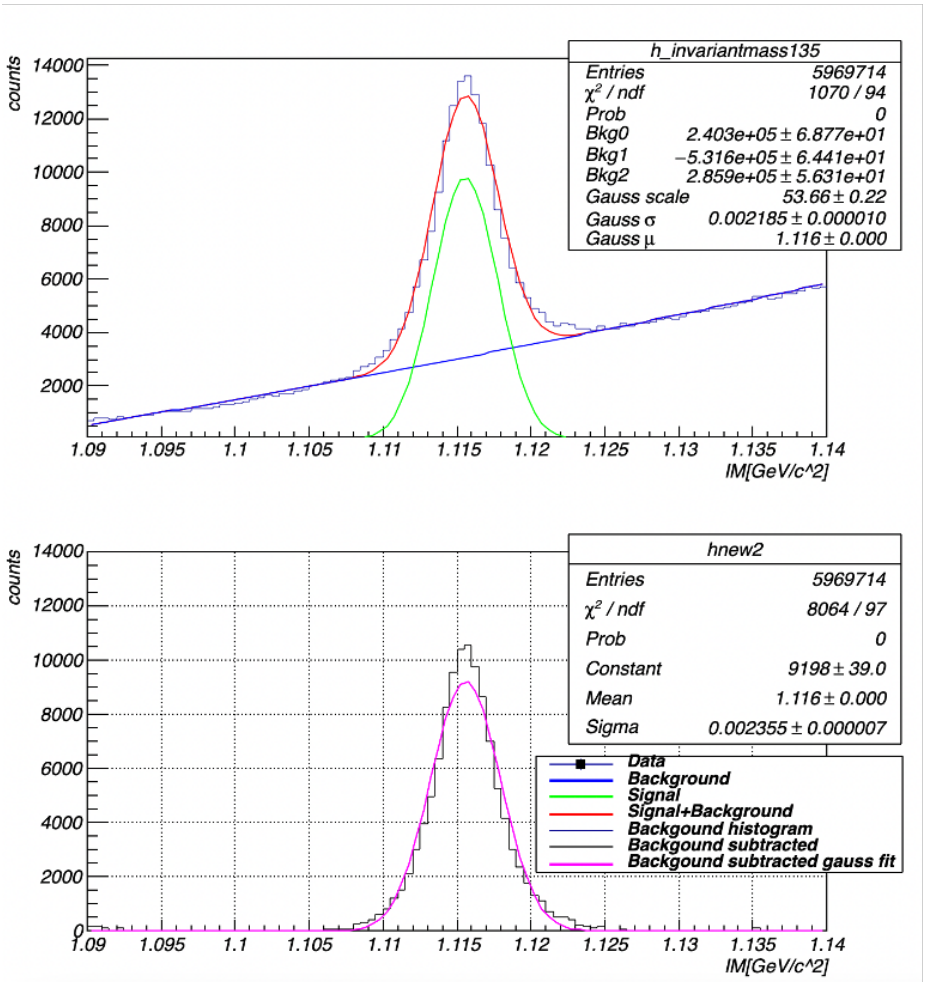

Figure A.44 Background subtraction on $IM_{p\pi^-}$ for the inclusive analysis using a fit to a Gaussian + second order polynomial functions for $p_\Lambda = [1.3, 1.4]$ GeV/c and $\theta_\Lambda = [0.2, 0.3]$ rad.

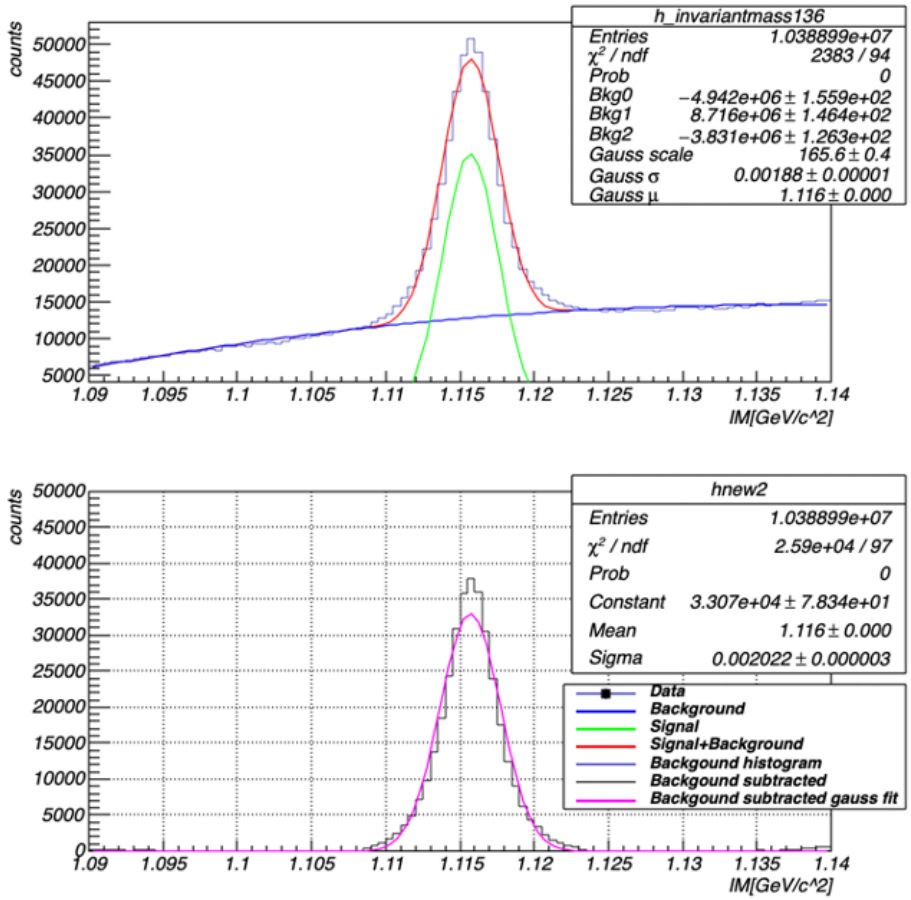

Figure A.45 Background subtraction on $IM_{p\pi^-}$ for the inclusive analysis using a fit to a Gaussian + second order polynomial functions for $p_\Lambda = [1.3, 1.4]$ GeV/c and $\theta_\Lambda = [0.3, 0.4]$ rad.

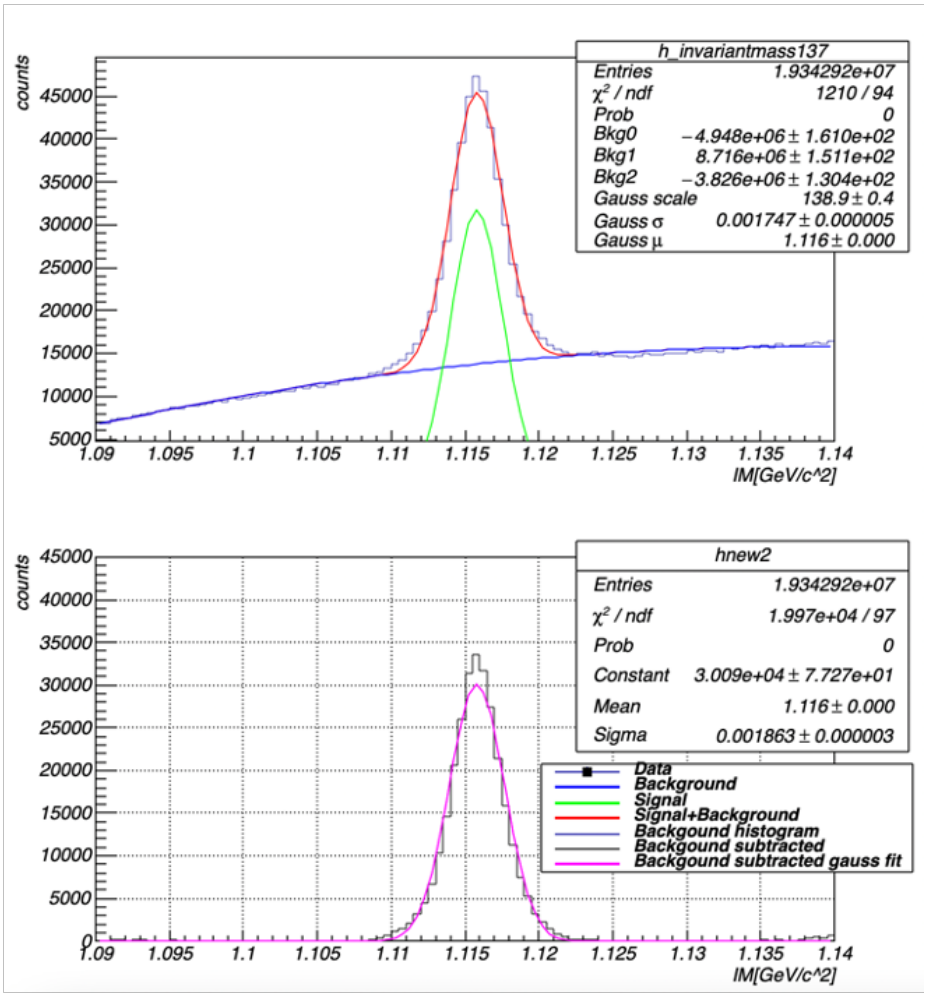

Figure A.46 Background subtraction on $IM_{p\pi^-}$ for the inclusive analysis using a fit to a Gaussian + second order polynomial functions for $p_\Lambda = [1.3, 1.4]$ GeV/c and $\theta_\Lambda = [0.4, 0.5]$ rad.

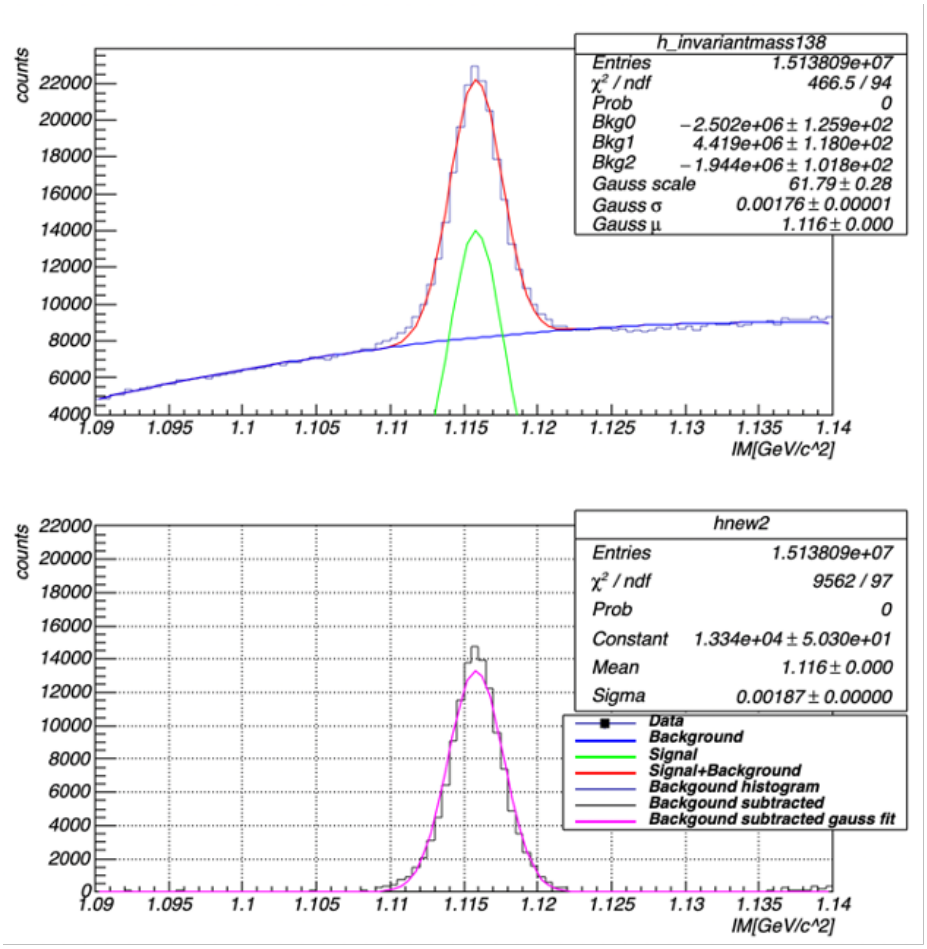

Figure A.47 Background subtraction on $IM_{p\pi^-}$ for the inclusive analysis using a fit to a Gaussian + second order polynomial functions for $p_\Lambda = [1.3, 1.4]$ GeV/c and $\theta_\Lambda = [0.5, 0.6]$ rad.

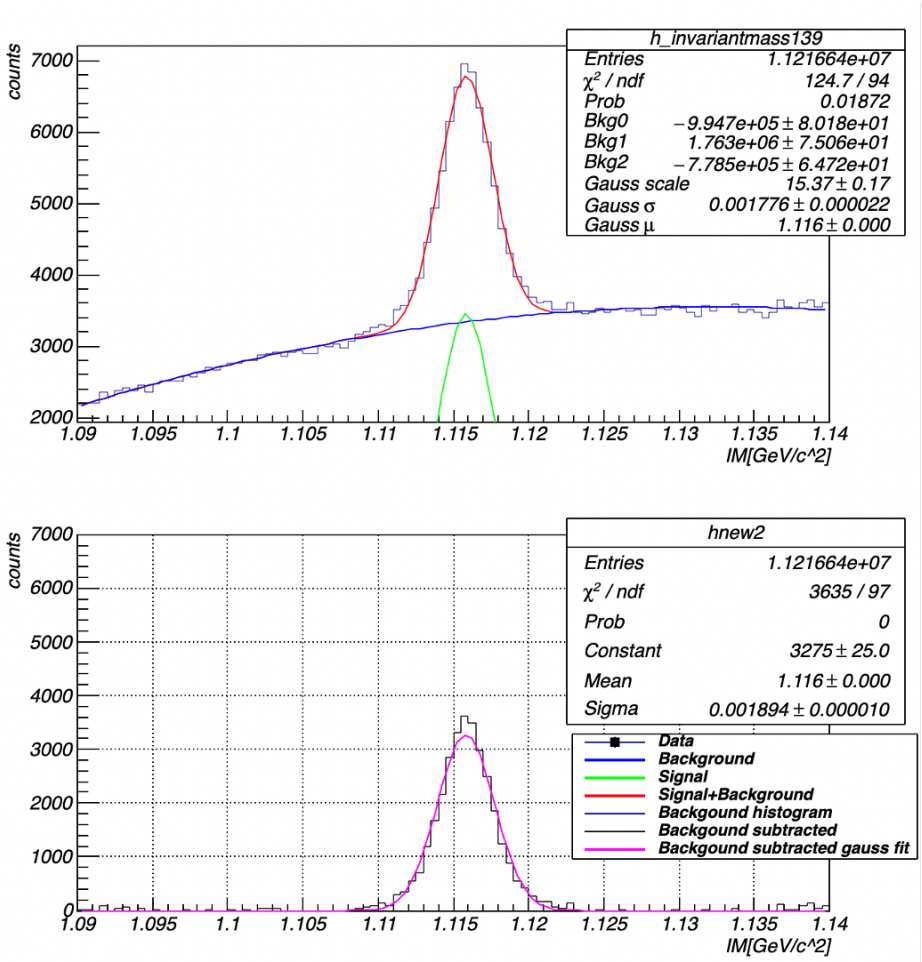

Figure A.48 Background subtraction on $IM_{p\pi^-}$ for the inclusive analysis using a fit to a Gaussian + second order polynomial functions for $p_\Lambda = [1.3, 1.4]$ GeV/c and $\theta_\Lambda = [0.6, 0.7]$ rad.

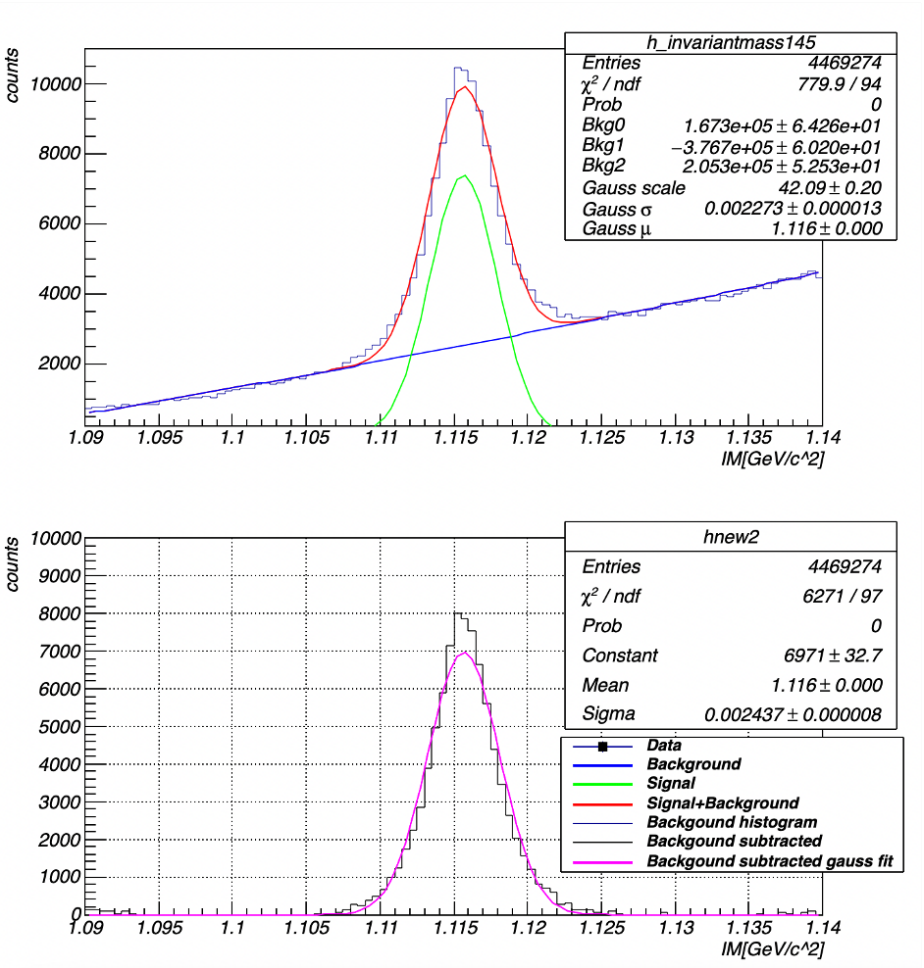

Figure A.49 Background subtraction on $IM_{p\pi^-}$ for the inclusive analysis using a fit to a Gaussian + second order polynomial functions for $p_\Lambda = [1.4, 1.5]$ GeV/c and $\theta_\Lambda = [0.2, 0.3]$ rad.

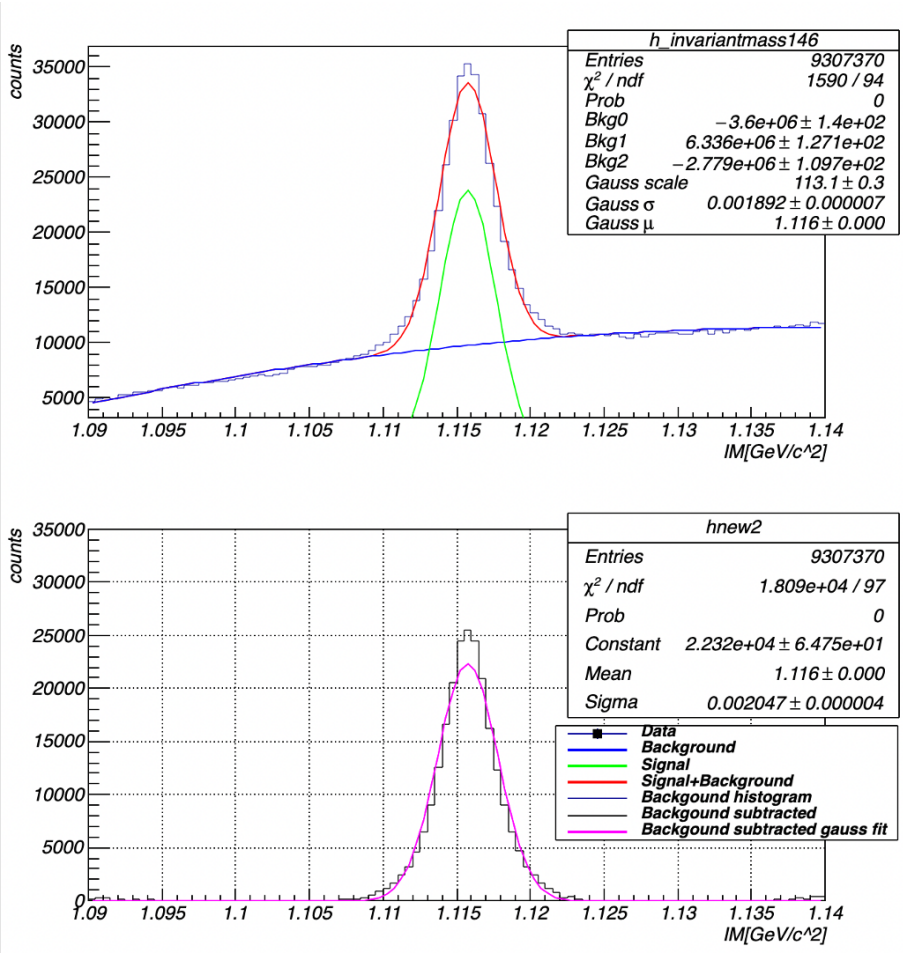

Figure A.50 Background subtraction on $IM_{p\pi^-}$ for the inclusive analysis using a fit to a Gaussian + second order polynomial functions for $p_\Lambda = [1.4, 1.5]$ GeV/c and $\theta_\Lambda = [0.3, 0.4]$ rad.

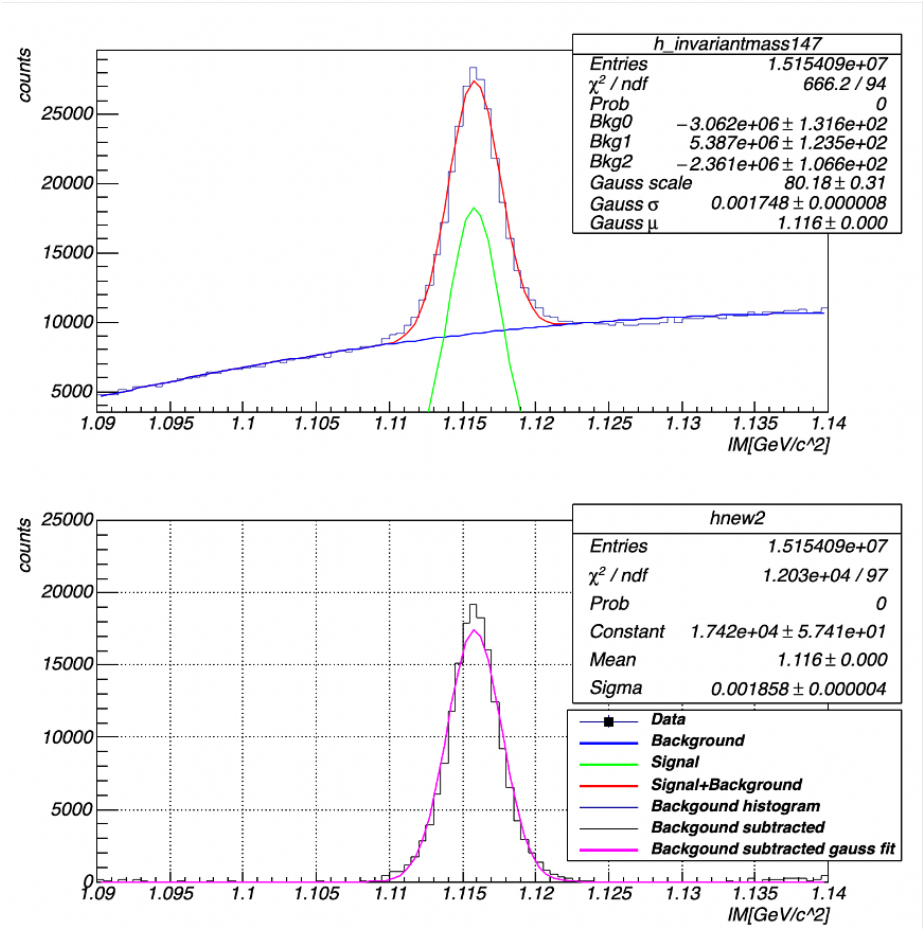

Figure A.51 Background subtraction on $IM_{p\pi^-}$ for the inclusive analysis using a fit to a Gaussian + second order polynomial functions for $p_\Lambda = [1.4, 1.5]$ GeV/c and $\theta_\Lambda = [0.4, 0.5]$ rad.

Appendix B

Background subtracted kaon-mass histogram for the exclusive analysis, fitted with Gaussian + exponential functions for all $IM^2_{p\pi^-}$ bins

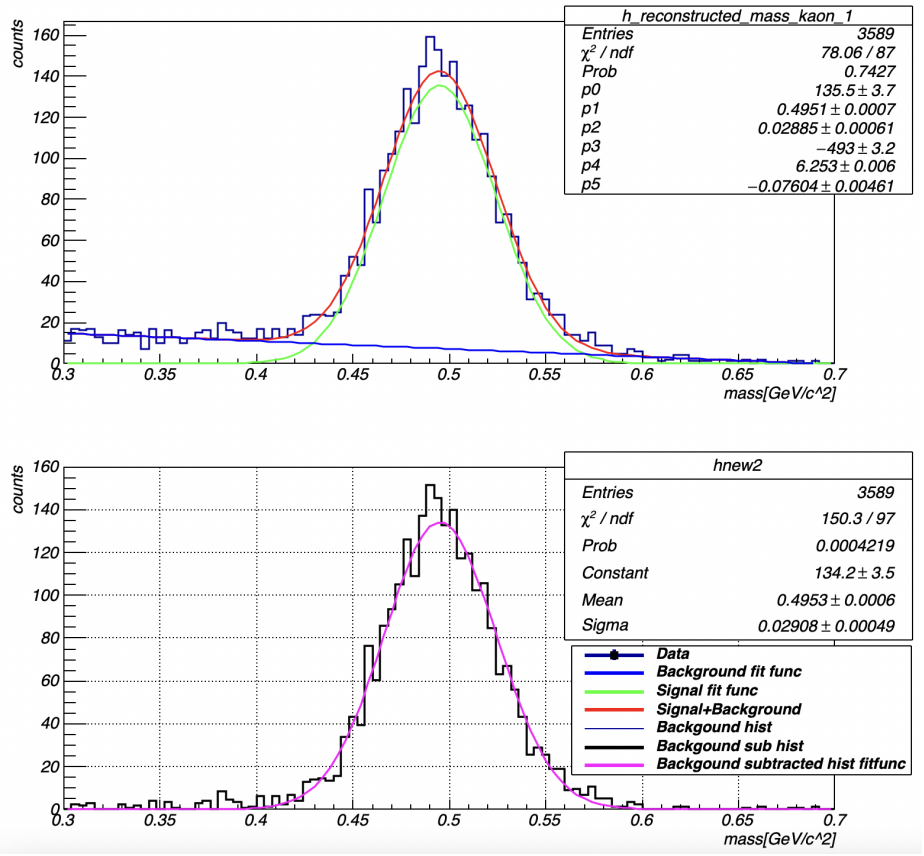

Figure B.1 Background subtracted kaon-mass histogram for the exclusive analysis, fitted with Gaussian + exponential functions for $IM^2_{p\pi^-}$ bin 1.17 – 1.18 ((GeV/c^2)^2).

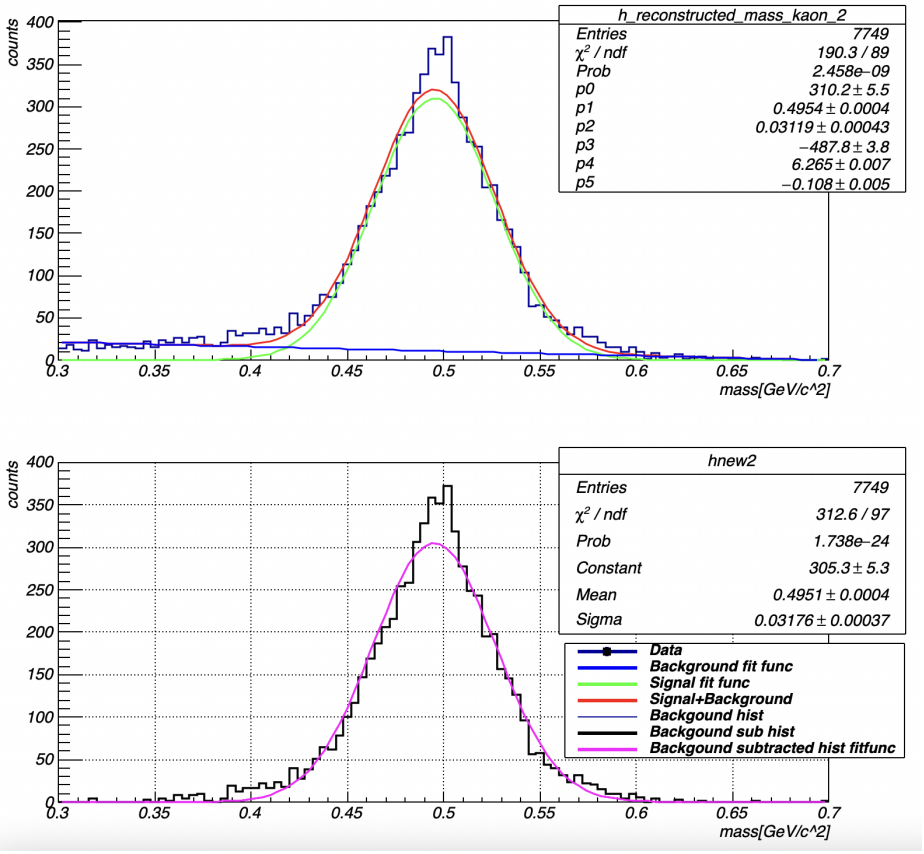

Figure B.2 Background subtracted kaon-mass histogram for the exclusive analysis, fitted with Gaussian + exponential functions for $IM^2_{p\pi^-}$ bin 1.18 – 1.19 $((\mathrm{GeV}/c^2)^2)$.

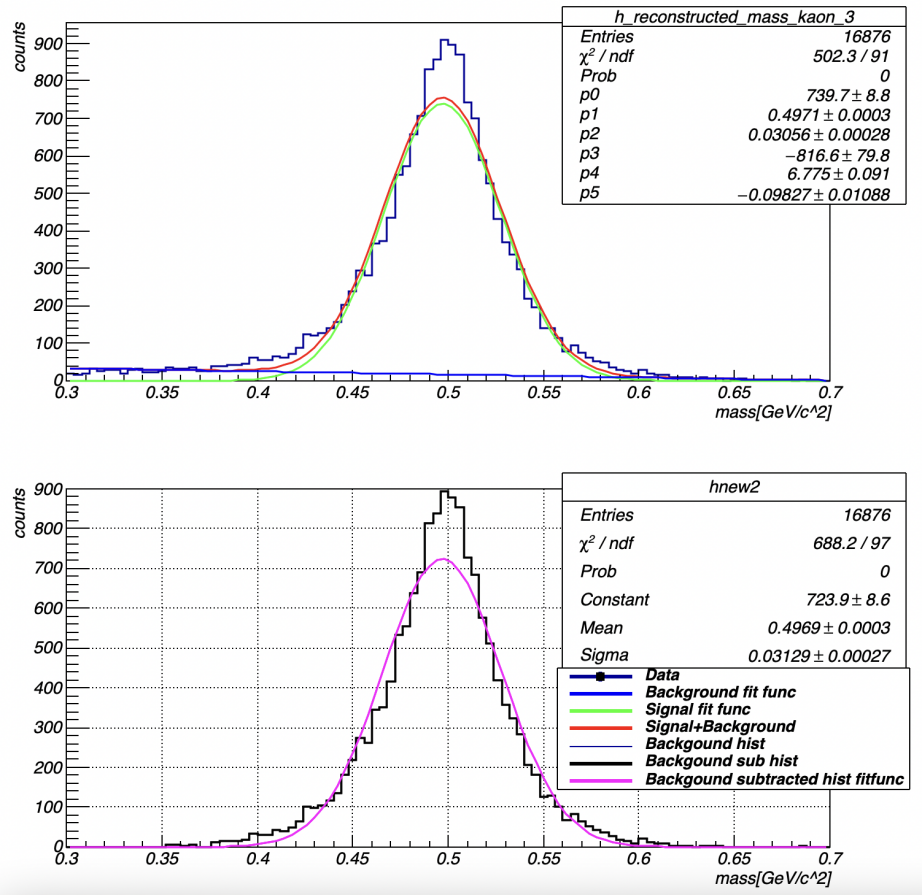

Figure B.3 Background subtracted kaon-mass histogram for the exclusive analysis, fitted with Gaussian + exponential functions for $IM^2_{p\pi^-}$ bin 1.19 – 1.20 $((\mathrm{GeV}/c^2)^2)$.

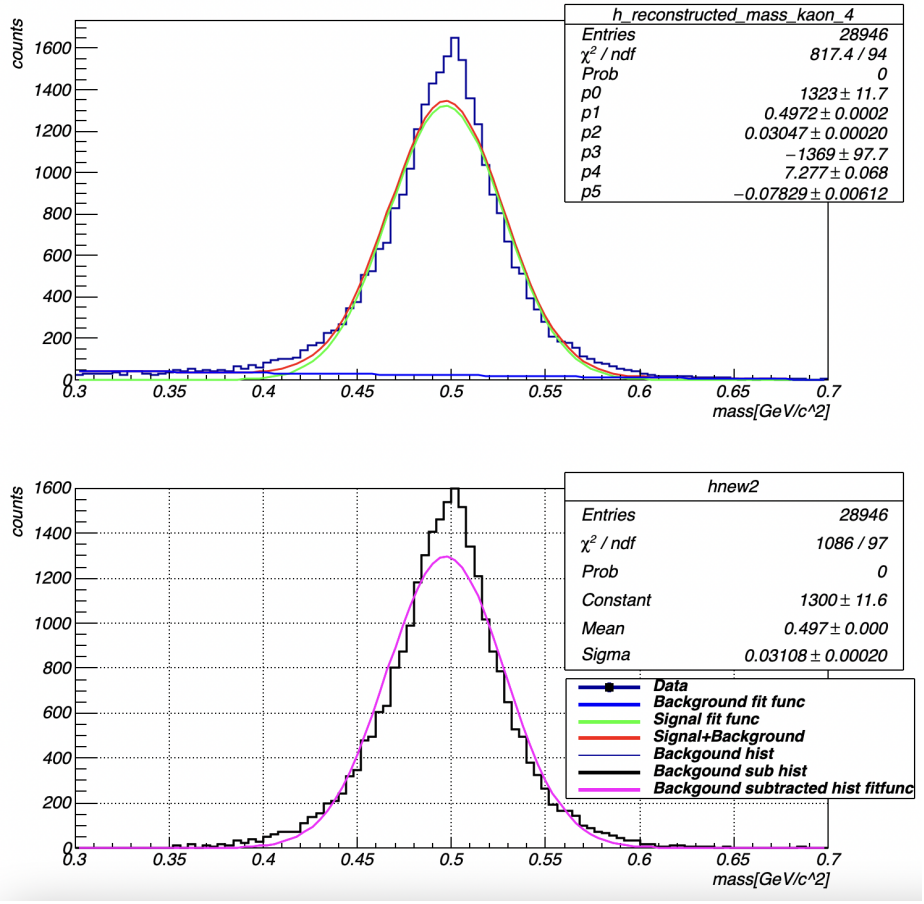

Figure B.4 Background subtracted kaon-mass histogram for the exclusive analysis, fitted with Gaussian + exponential functions for $IM^2_{p\pi^-}$ bin 1.20 – 1.21 $((\mathrm{GeV}/c^2)^2)$.

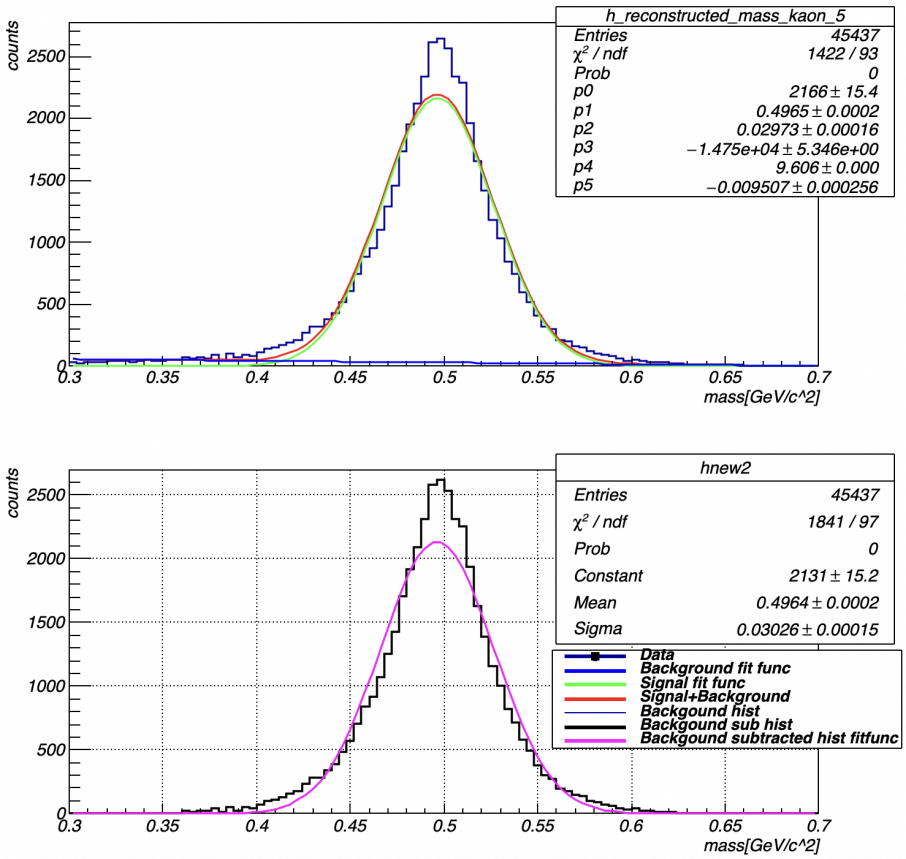

Figure B.5 Background subtracted kaon-mass histogram for the exclusive analysis, fitted with Gaussian + exponential functions for $IM^2_{p\pi^-}$ bin 1.21 – 1.22 $((\mathrm{GeV}/c^2)^2)$.

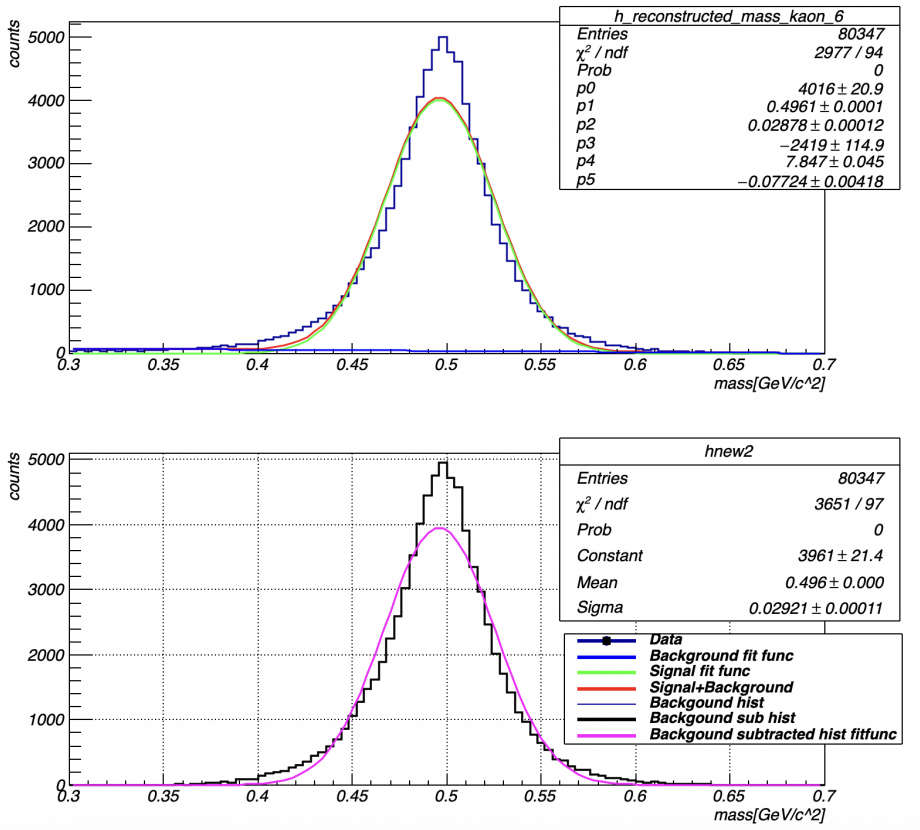

Figure B.6 Background subtracted kaon-mass histogram for the exclusive analysis, fitted with Gaussian + exponential functions for $IM^2_{p\pi^-}$ bin 1.22 – 1.23 $((\mathrm{GeV}/c^2)^2)$.

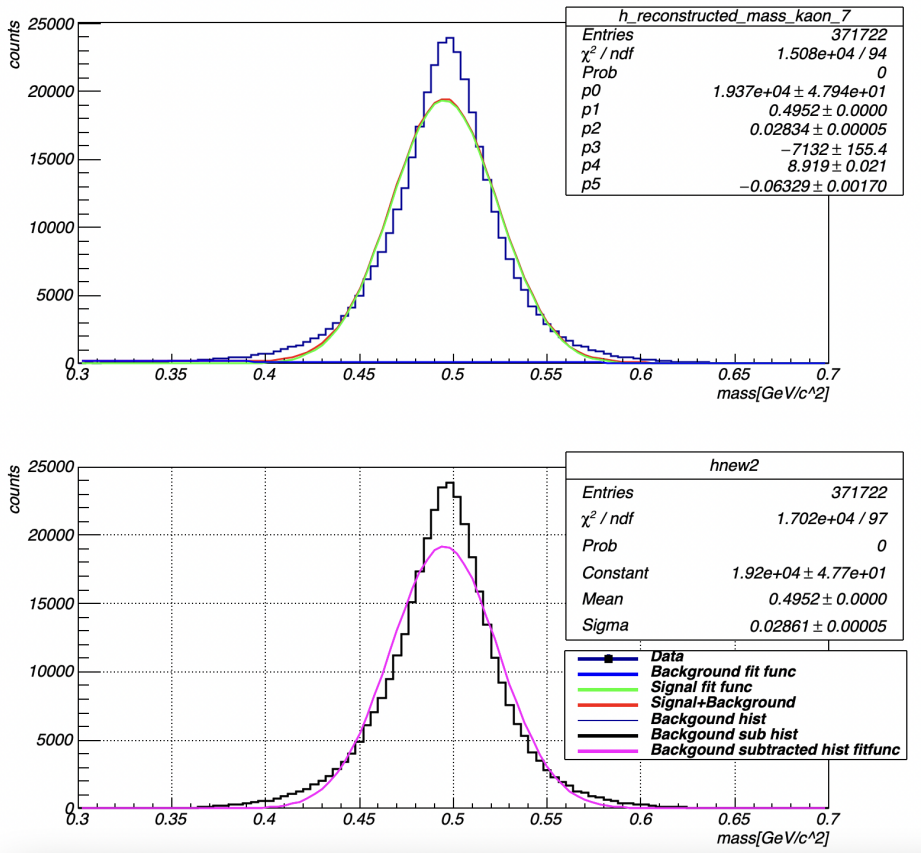

Figure B.7 Background subtracted kaon-mass histogram for the exclusive analysis, fitted with Gaussian + exponential functions for $IM^2_{p\pi^-}$ bin 1.23 – 1.24 $((\mathrm{GeV}/c^2)^2)$.

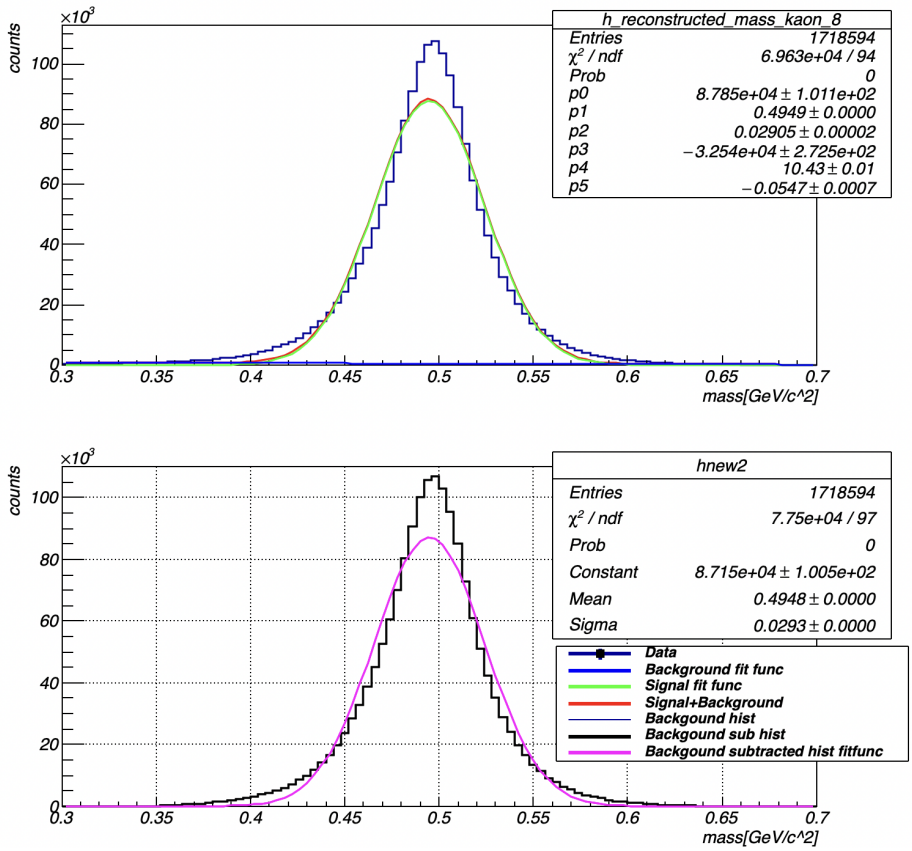

Figure B.8 Background subtracted kaon-mass histogram for the exclusive analysis, fitted with Gaussian + exponential functions for $IM^2_{p\pi^-}$ bin 1.24 – 1.25 $((\mathrm{GeV}/c^2)^2)$.

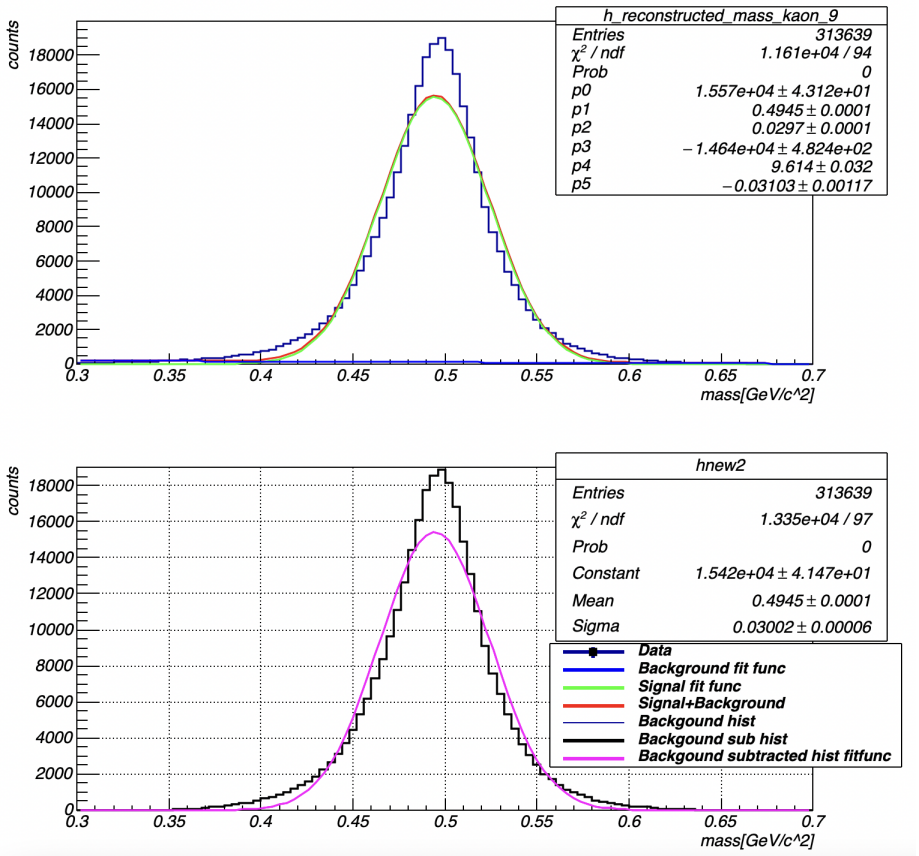

Figure B.9 Background subtracted kaon-mass histogram for the exclusive analysis, fitted with Gaussian + exponential functions for $IM^2_{p\pi^-}$ bin 1.25 – 1.26 $((\mathrm{GeV}/c^2)^2)$.

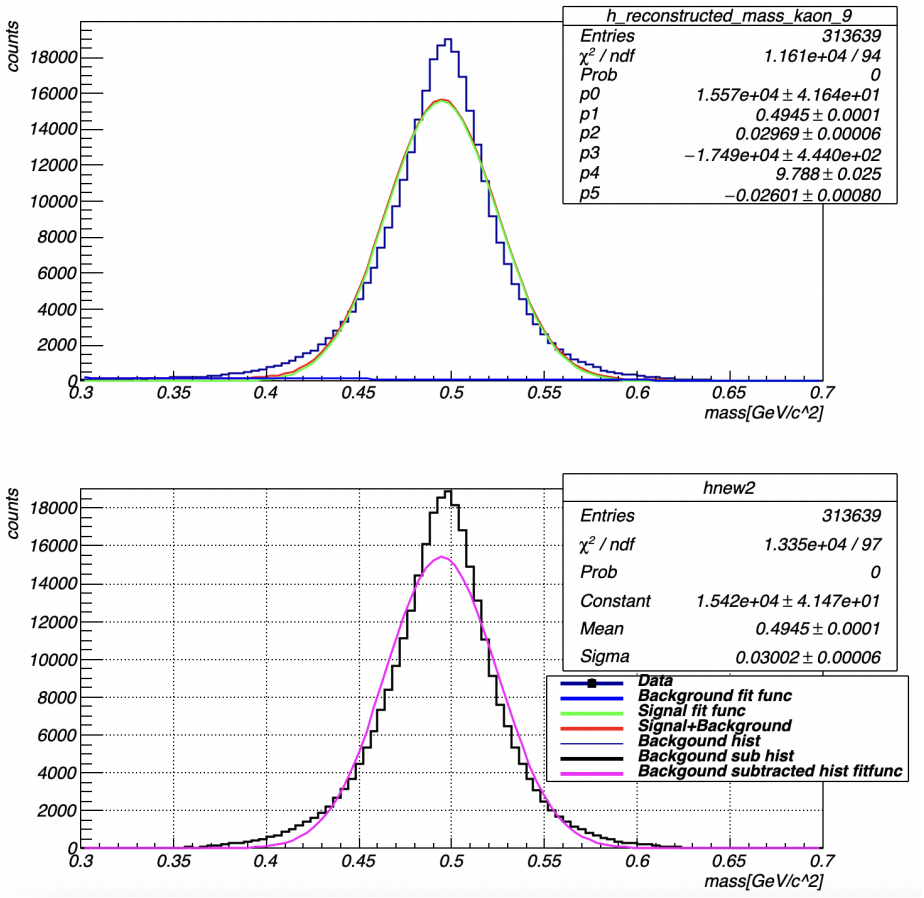

Figure B.10 Background subtracted kaon-mass histogram for the exclusive analysis, fitted with Gaussian + exponential functions for $IM^2_{p\pi^-}$ bin 1.26 – 1.27 $((\mathrm{GeV}/c^2)^2)$.

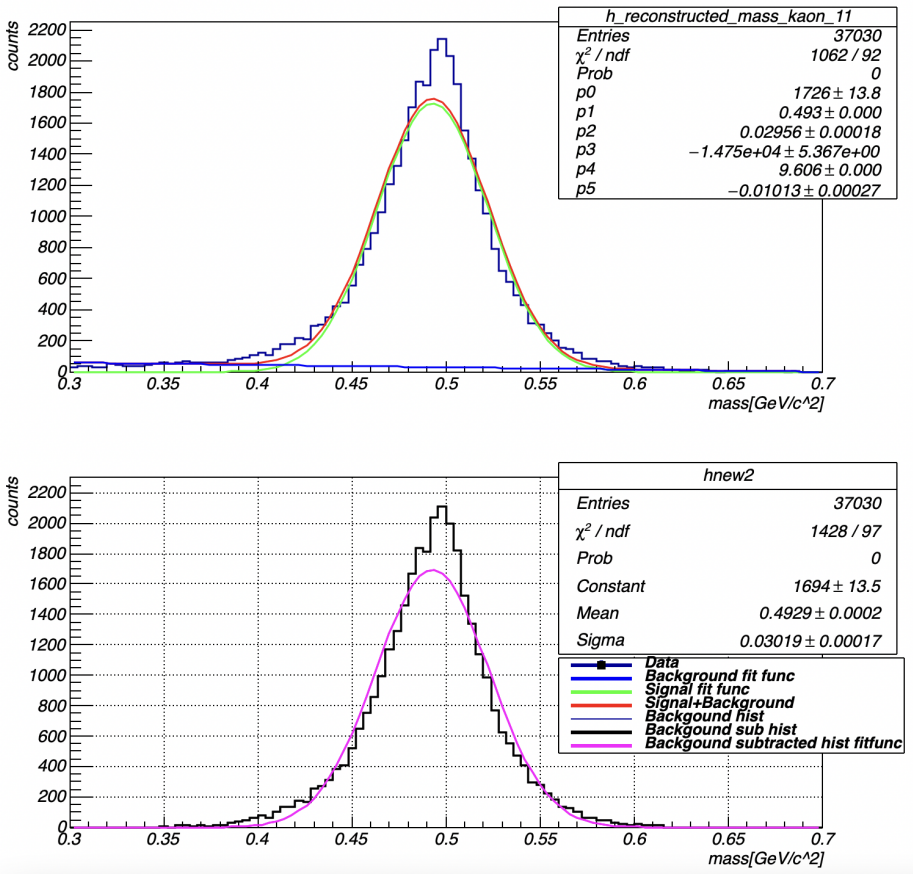

Figure B.11 Background subtracted kaon-mass histogram for the exclusive analysis, fitted with Gaussian + exponential functions for $IM^2_{p\pi^-}$ bin 1.27 – 1.28 $((\mathrm{GeV}/c^2)^2)$.

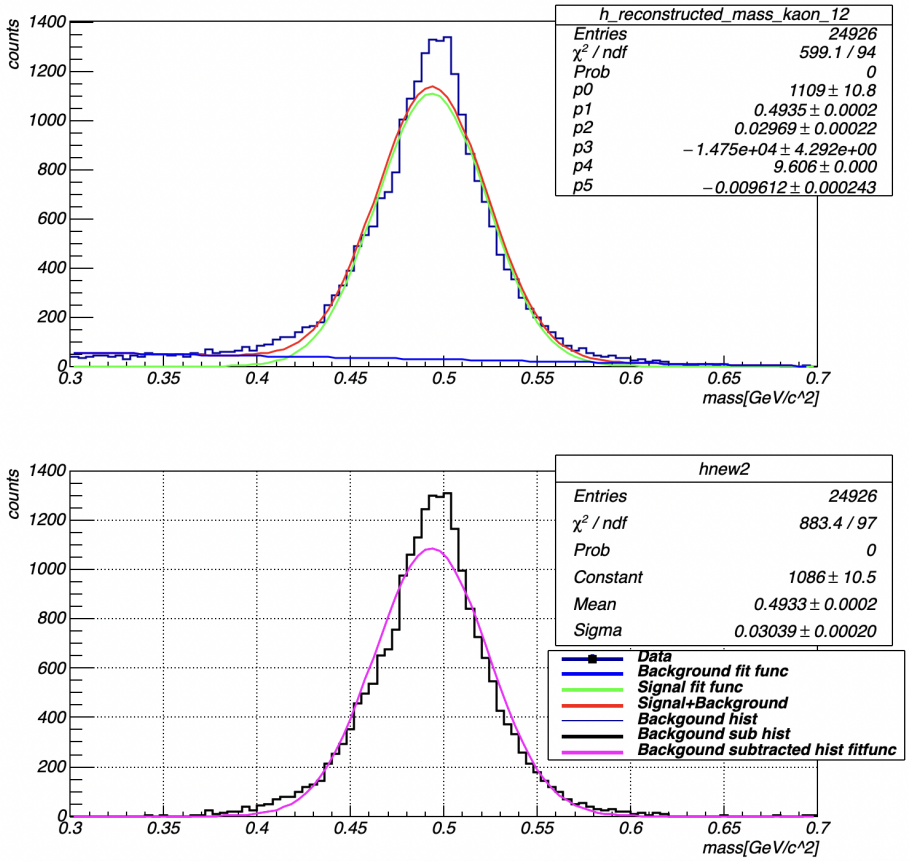

Figure B.12 Background subtracted kaon-mass histogram for the exclusive analysis, fitted with Gaussian + exponential functions for $IM^2_{p\pi^-}$ bin 1.28 – 1.29 $((\mathrm{GeV}/c^2)^2)$.

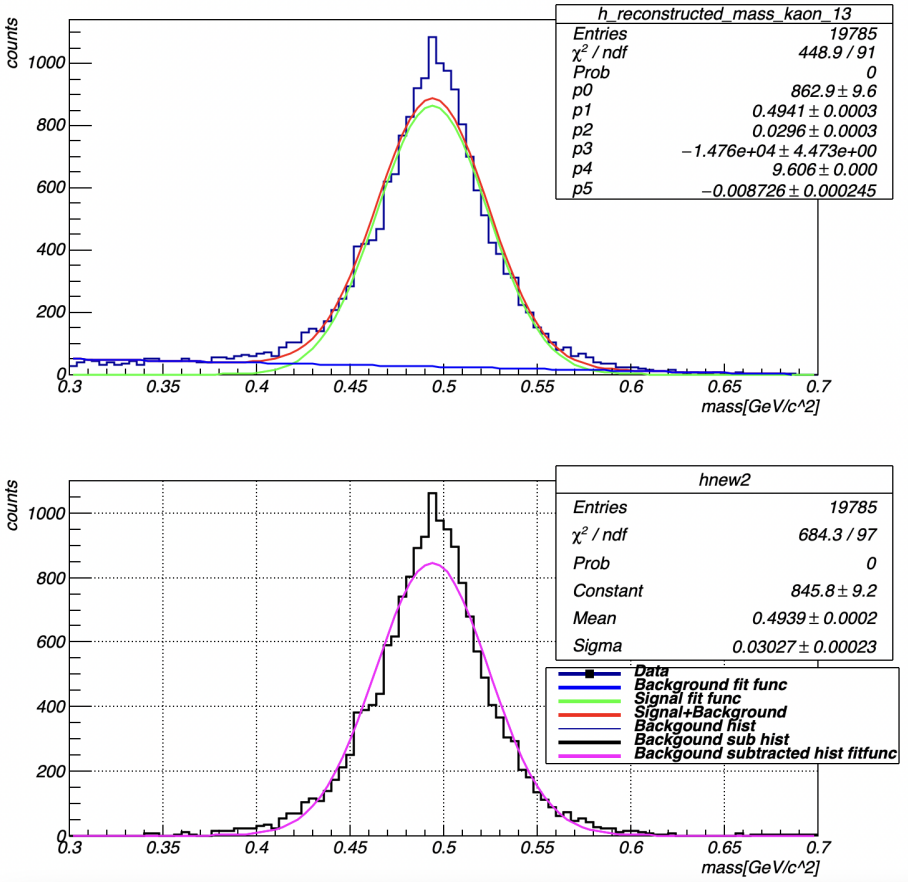

Figure B.13 Background subtracted kaon-mass histogram for the exclusive analysis, fitted with Gaussian + exponential functions for $IM^2_{p\pi^-}$ bin 1.29 – 1.30 $((\mathrm{GeV}/c^2)^2)$.

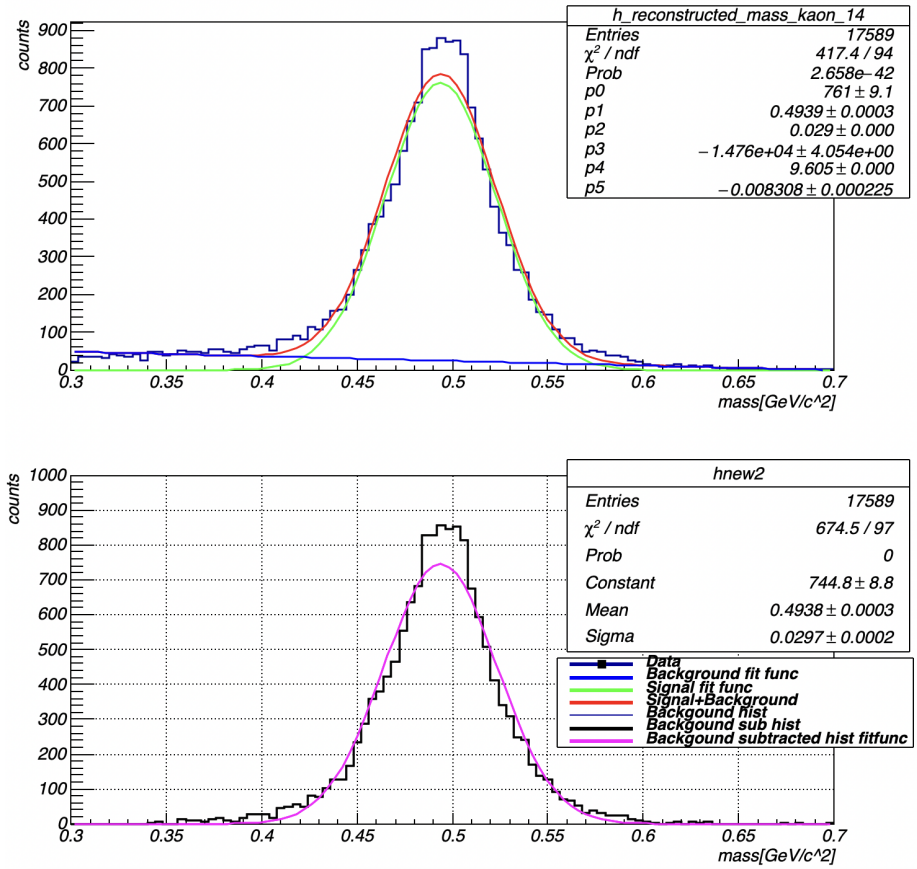

Figure B.14 Background subtracted kaon-mass histogram for the exclusive analysis, fitted with Gaussian + exponential functions for $IM^2_{p\pi^-}$ bin 1.30 – 1.31 $((\mathrm{GeV}/c^2)^2)$.

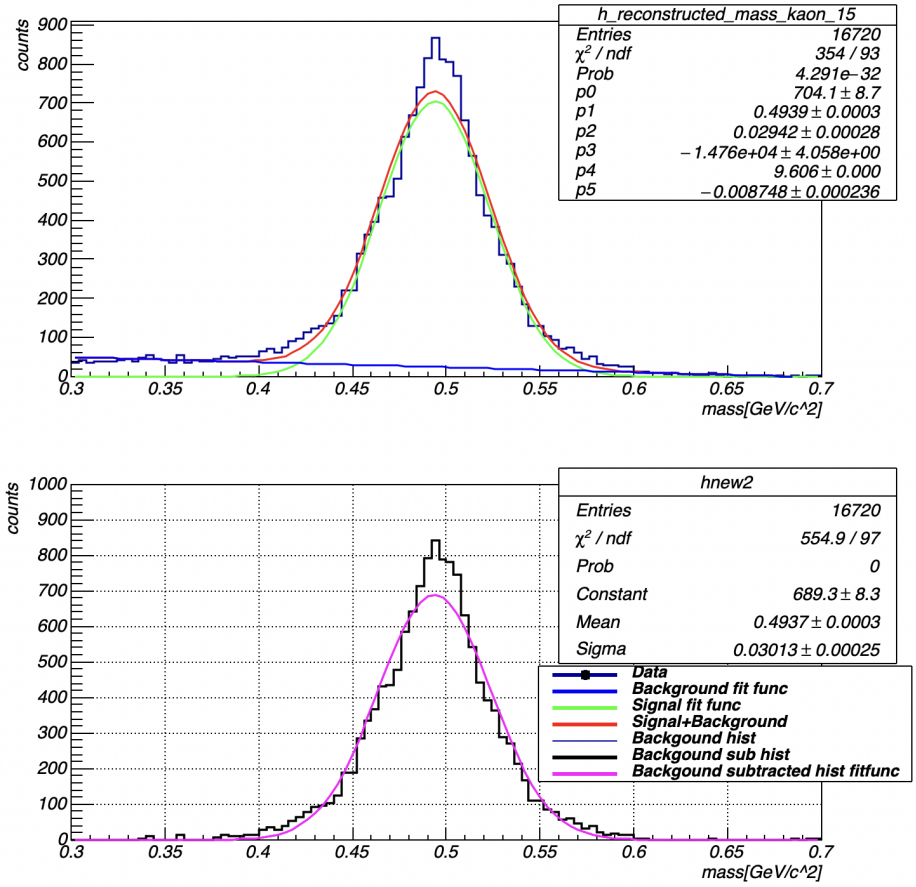

Figure B.15 Background subtracted kaon-mass histogram for the exclusive analysis, fitted with Gaussian + exponential functions for $IM^2_{p\pi^-}$ bin 1.31 – 1.32 $((\mathrm{GeV}/c^2)^2)$.

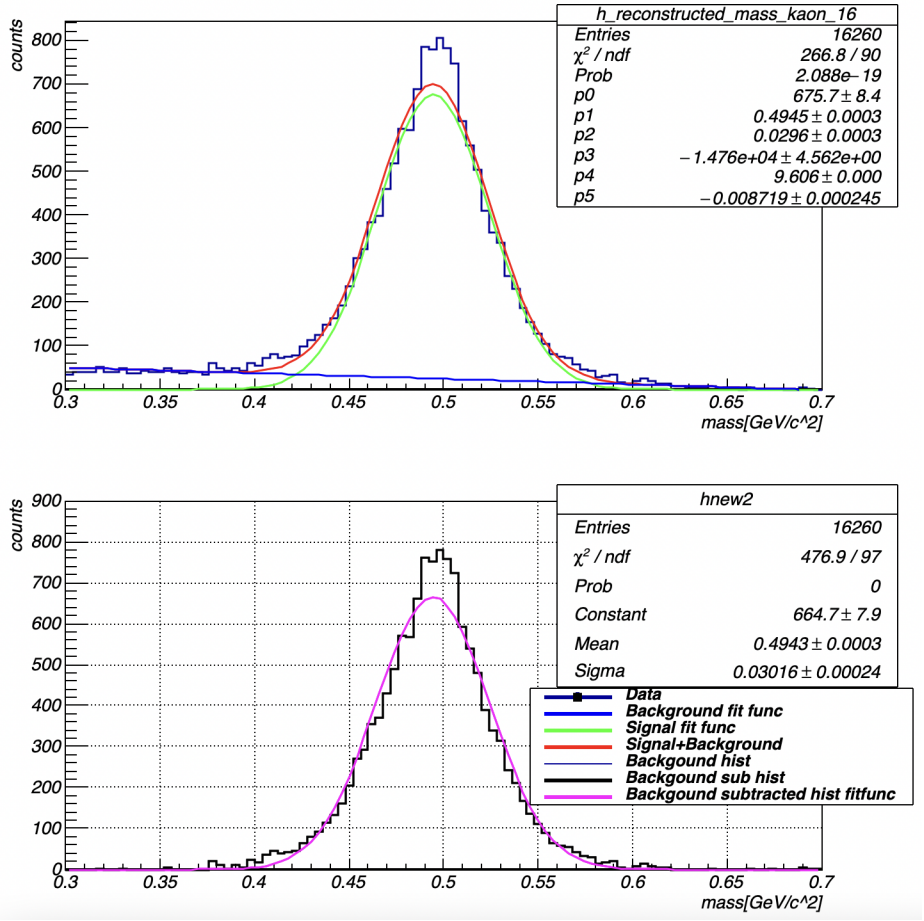

Figure B.16 Background subtracted kaon-mass histogram for the exclusive analysis, fitted with Gaussian + exponential functions for $IM^2_{p\pi^-}$ bin 1.32 – 1.33 $((\mathrm{GeV}/c^2)^2)$.

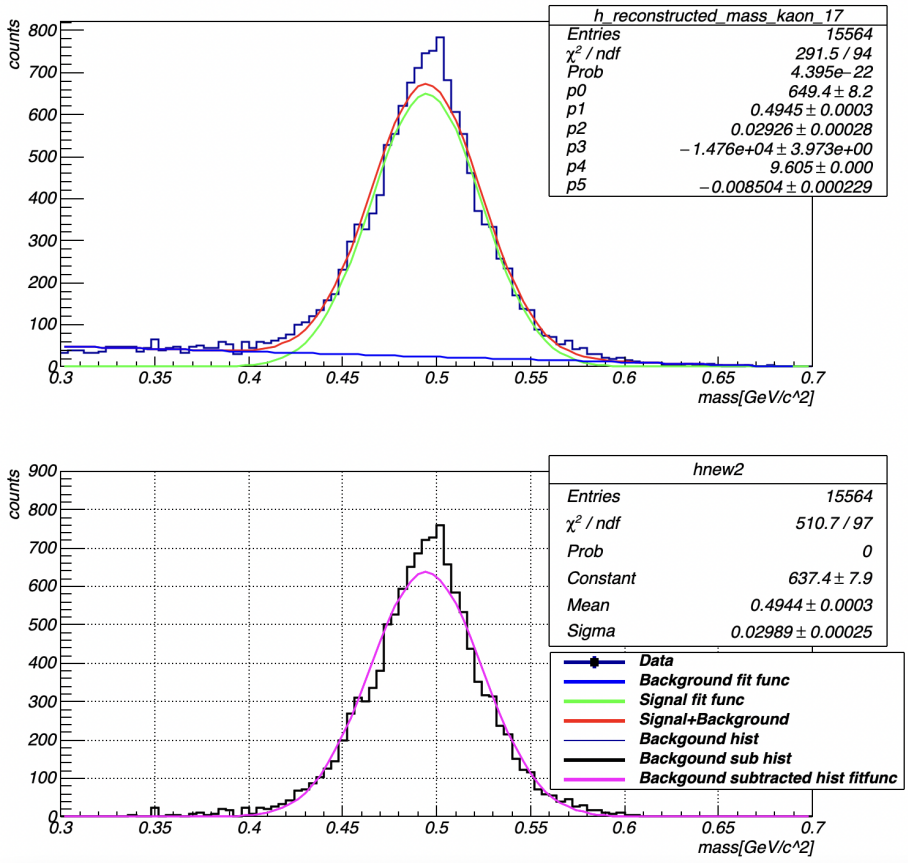

Figure B.17 Background subtracted kaon-mass histogram for the exclusive analysis, fitted with Gaussian + exponential functions for $IM^2_{p\pi^-}$ bin 1.33 – 1.34 $((\mathrm{GeV}/c^2)^2)$.

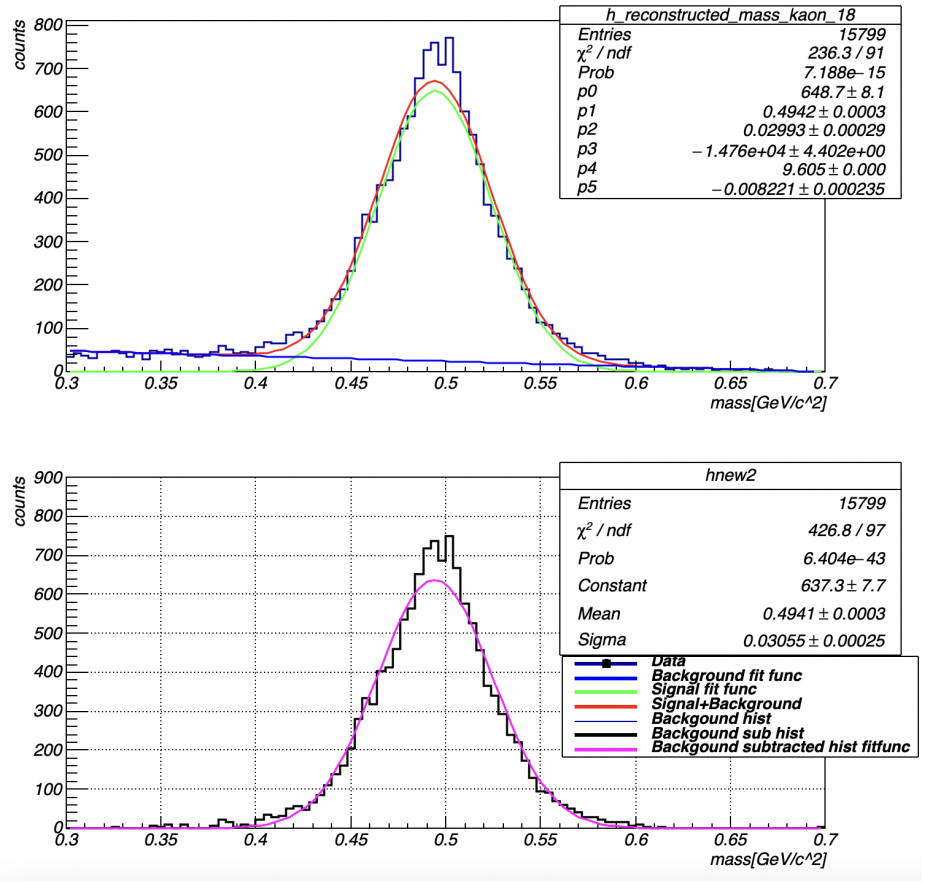

Figure B.18 Background subtracted kaon-mass histogram for the exclusive analysis, fitted with Gaussian + exponential functions for $IM^2_{p\pi^-}$ bin 1.34 – 1.35 $((\mathrm{GeV}/c^2)^2)$.

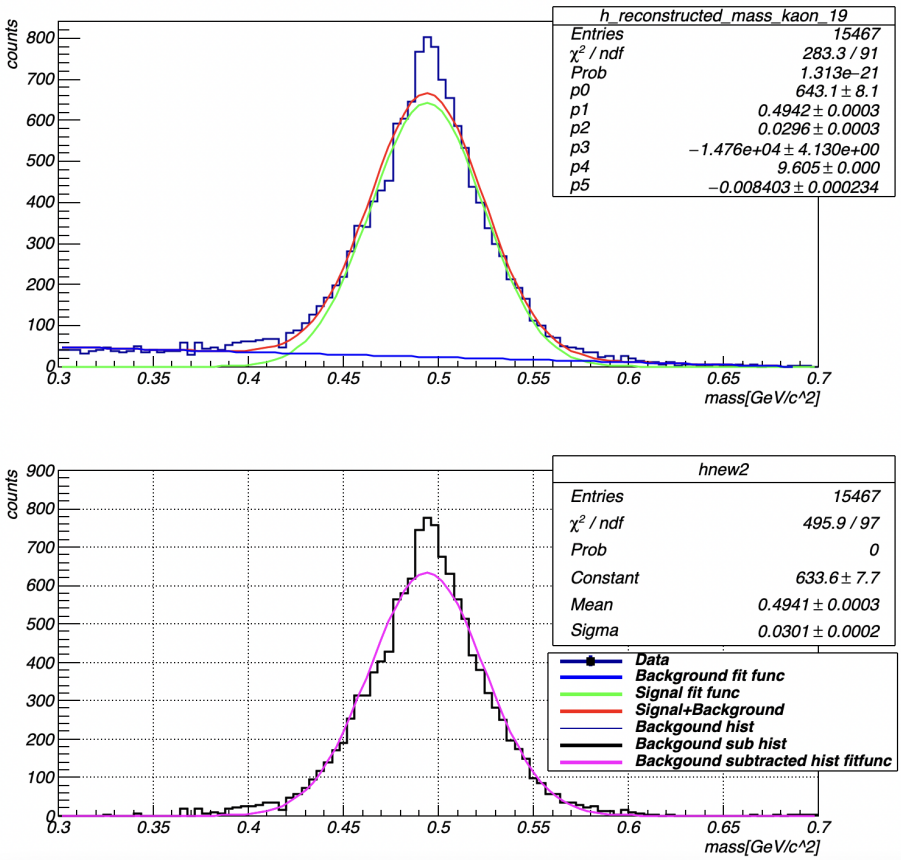

Figure B.19 Background subtracted kaon-mass histogram for the exclusive analysis, fitted with Gaussian + exponential functions for $IM^2_{p\pi^-}$ bin 1.35 – 1.36 $((\mathrm{GeV}/c^2)^2)$.

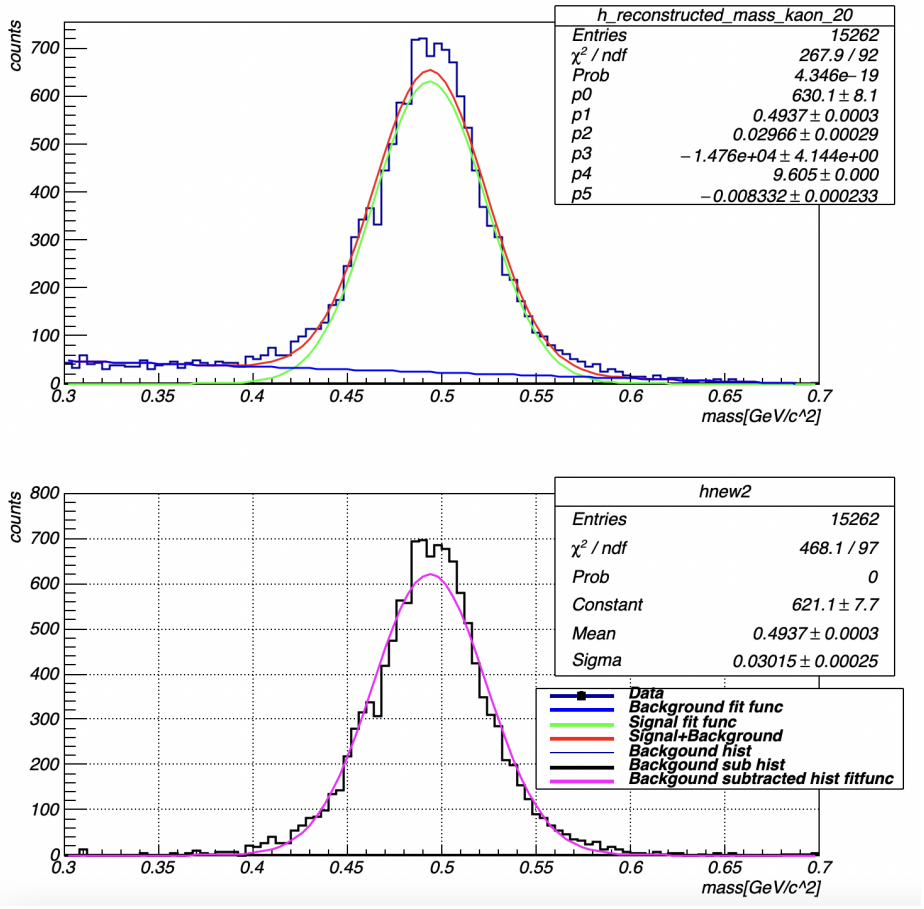

Figure B.20 Background subtracted kaon-mass histogram for the exclusive analysis, fitted with Gaussian + exponential functions for $IM^2_{p\pi^-}$ bin 1.36 – 1.37 $((\mathrm{GeV}/c^2)^2)$.

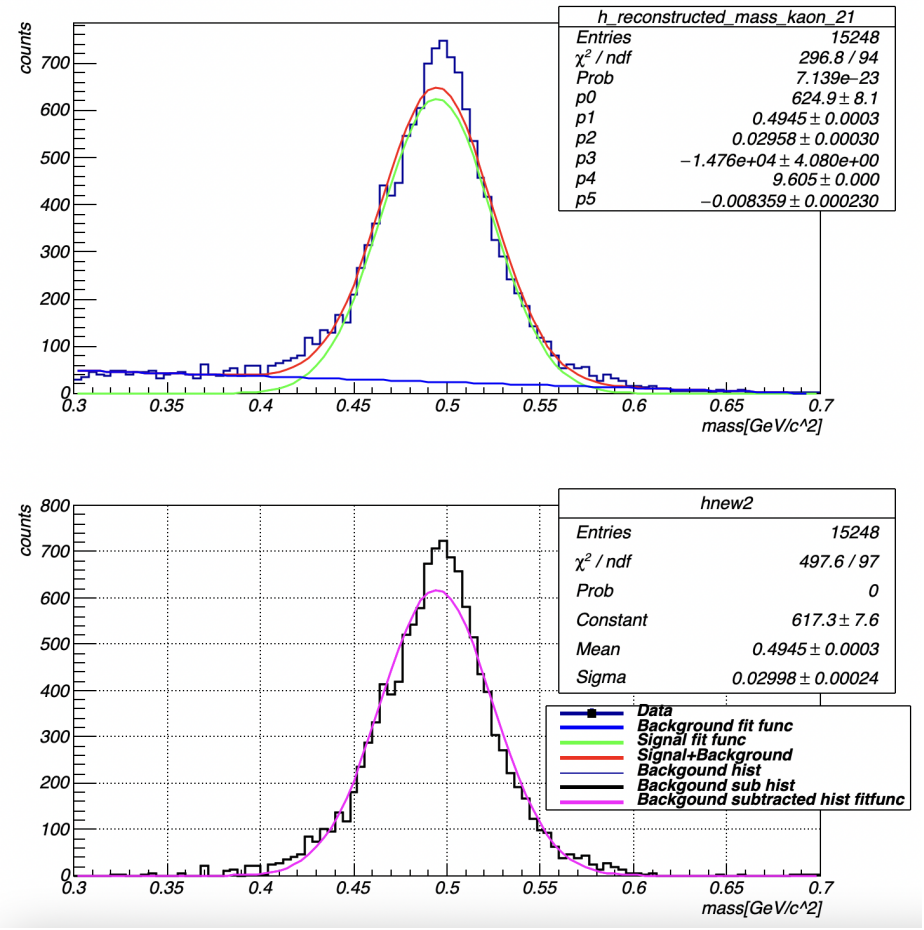

Figure B.21 Background subtracted kaon-mass histogram for the exclusive analysis, fitted with Gaussian + exponential functions for $IM^2_{p\pi^-}$ bin 1.37 – 1.38 $((\mathrm{GeV}/c^2)^2)$.

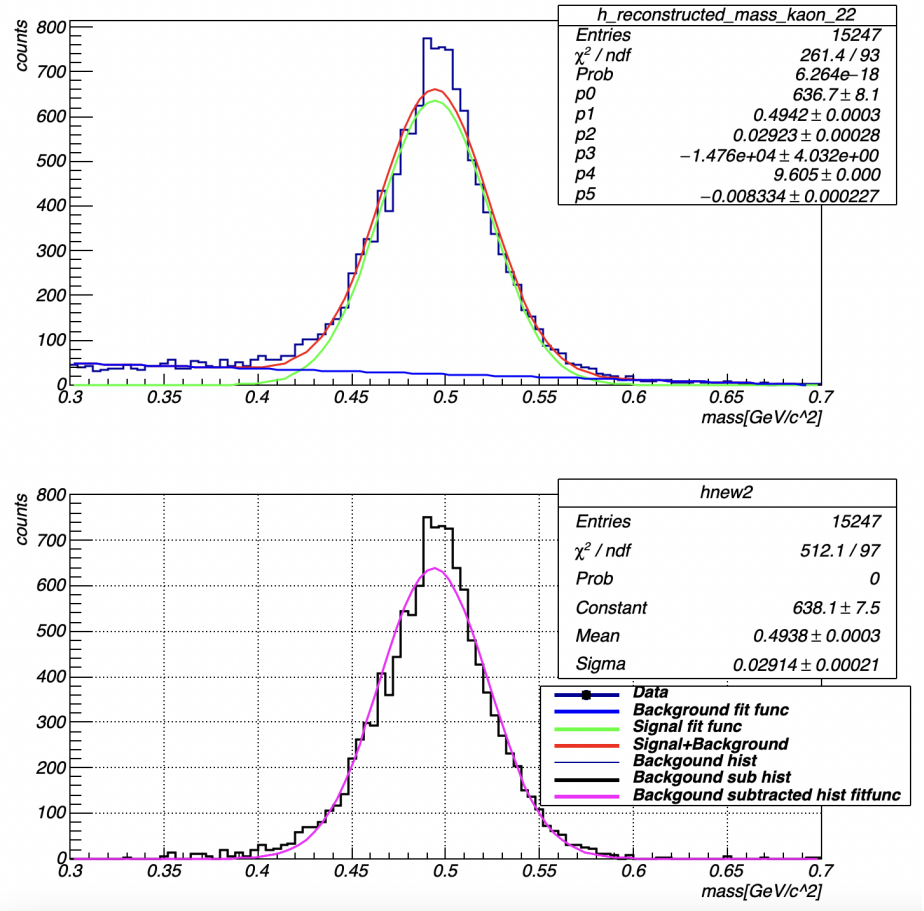

Figure B.22 Background subtracted kaon-mass histogram for the exclusive analysis, fitted with Gaussian + exponential functions for $IM^2_{p\pi^-}$ bin 1.38 – 1.39 $((\mathrm{GeV}/c^2)^2)$.

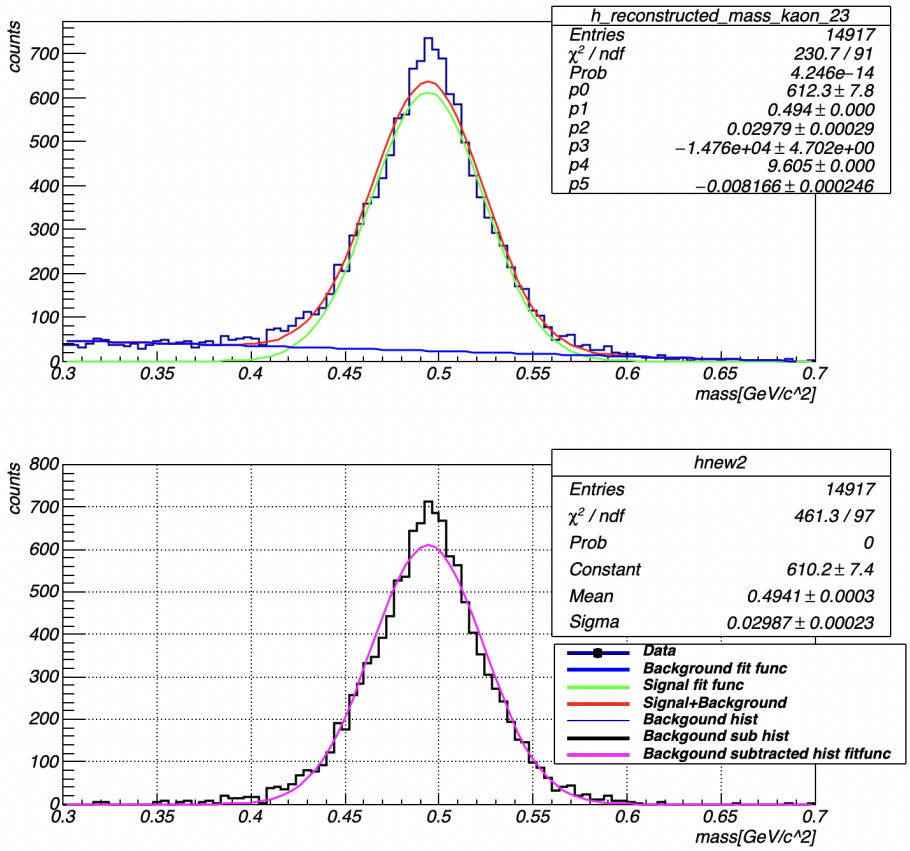

Figure B.23 Background subtracted kaon-mass histogram for the exclusive analysis, fitted with Gaussian + exponential functions for $IM^2_{p\pi^-}$ bin 1.39 – 1.40 $((\mathrm{GeV}/c^2)^2)$.

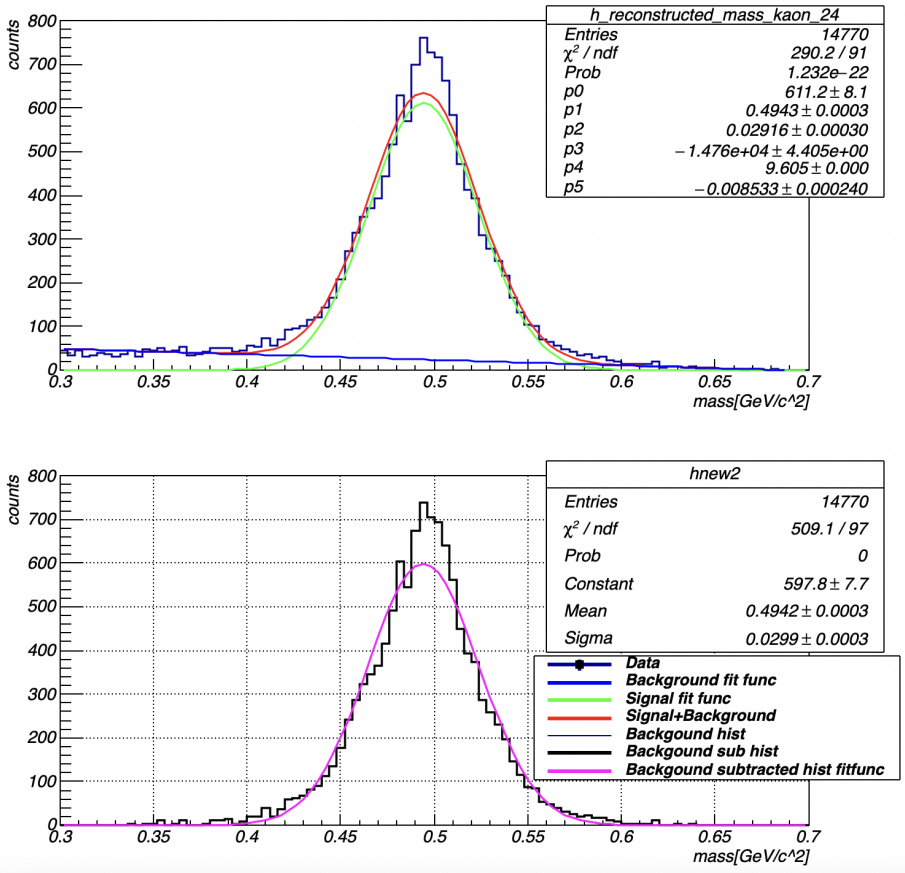

Figure B.24 Background subtracted kaon-mass histogram for the exclusive analysis, fitted with Gaussian + exponential functions for $IM^2_{p\pi^-}$ bin 1.40 – 1.41 $((\mathrm{GeV}/c^2)^2)$.

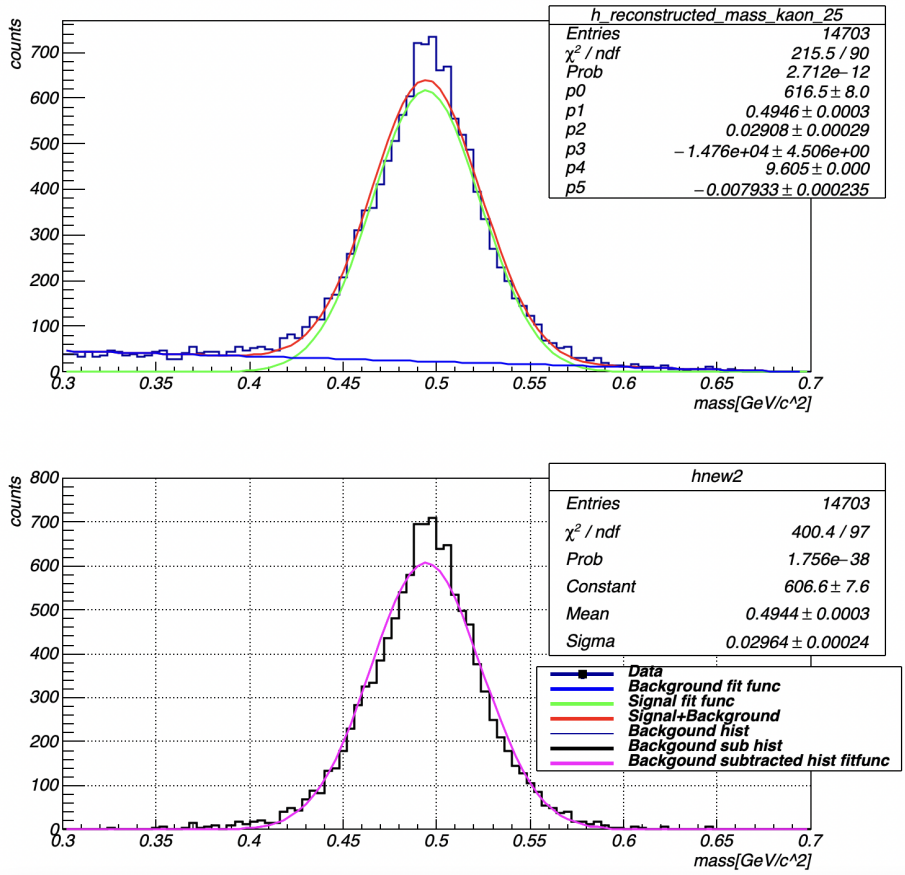

Figure B.25 Background subtracted kaon-mass histogram for the exclusive analysis, fitted with Gaussian + exponential functions for $IM^2_{p\pi^-}$ bin 1.41 – 1.42 $((\mathrm{GeV}/c^2)^2)$.

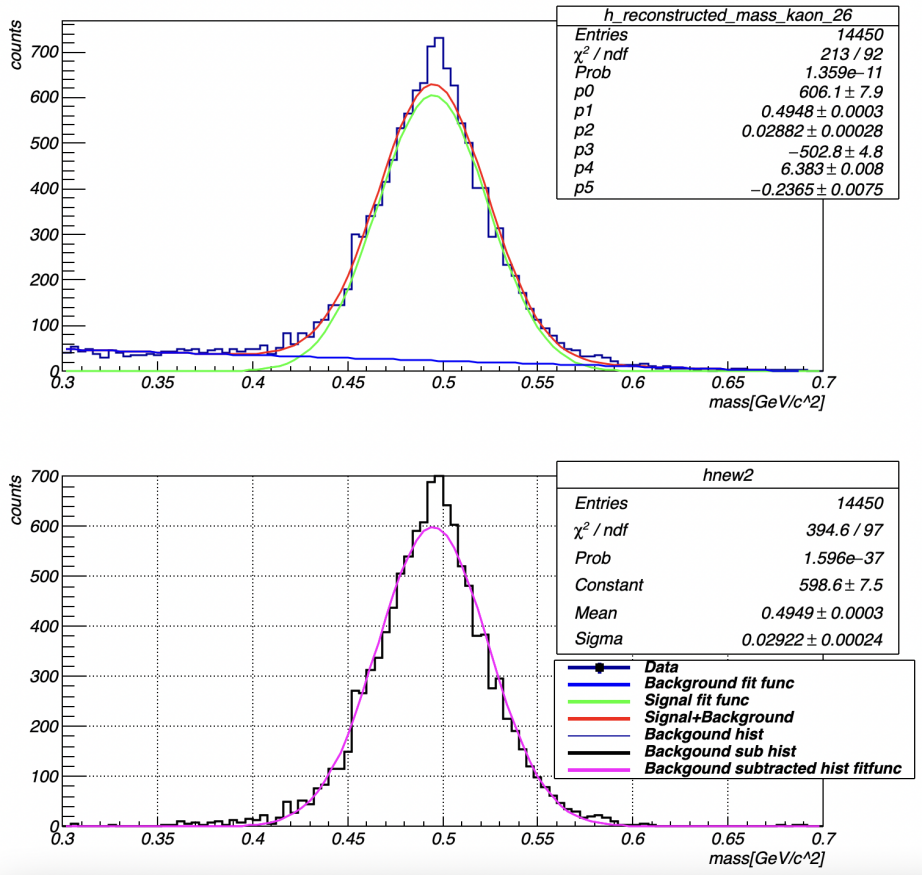

Figure B.26 Background subtracted kaon-mass histogram for the exclusive analysis, fitted with Gaussian + exponential functions for $IM^2_{p\pi^-}$ bin 1.42 – 1.43 $((\mathrm{GeV}/c^2)^2)$.

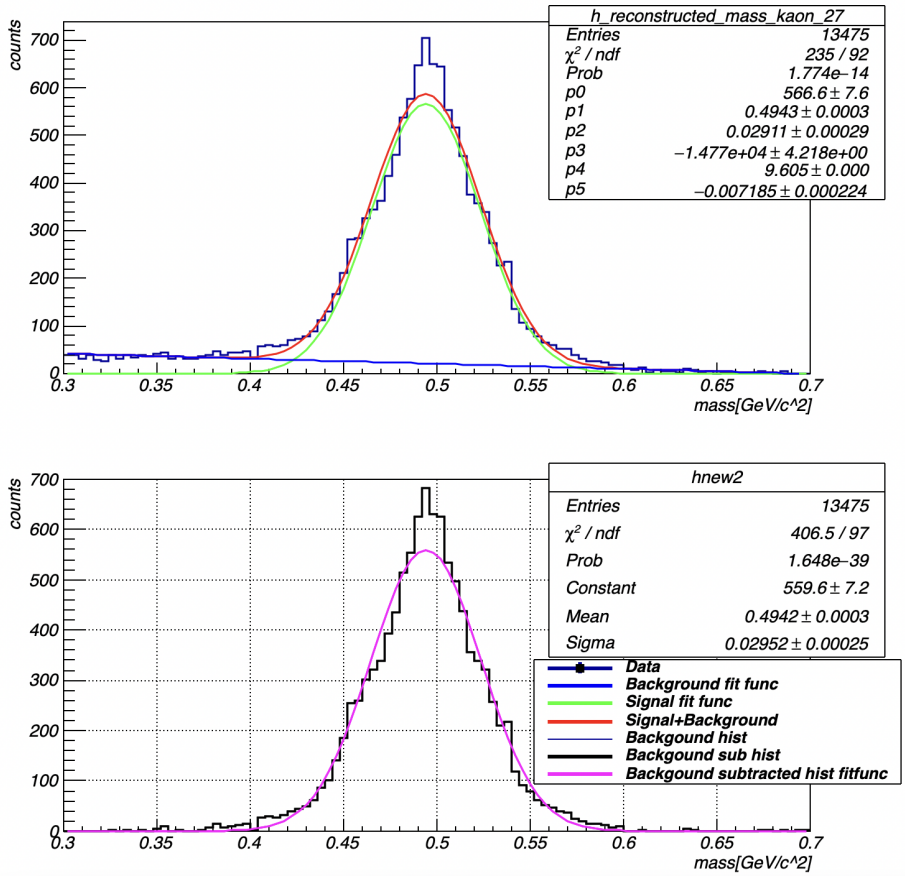

Figure B.27 Background subtracted kaon-mass histogram for the exclusive analysis, fitted with Gaussian + exponential functions for $IM^2_{p\pi^-}$ bin 1.43 – 1.44 $((\mathrm{GeV}/c^2)^2)$.

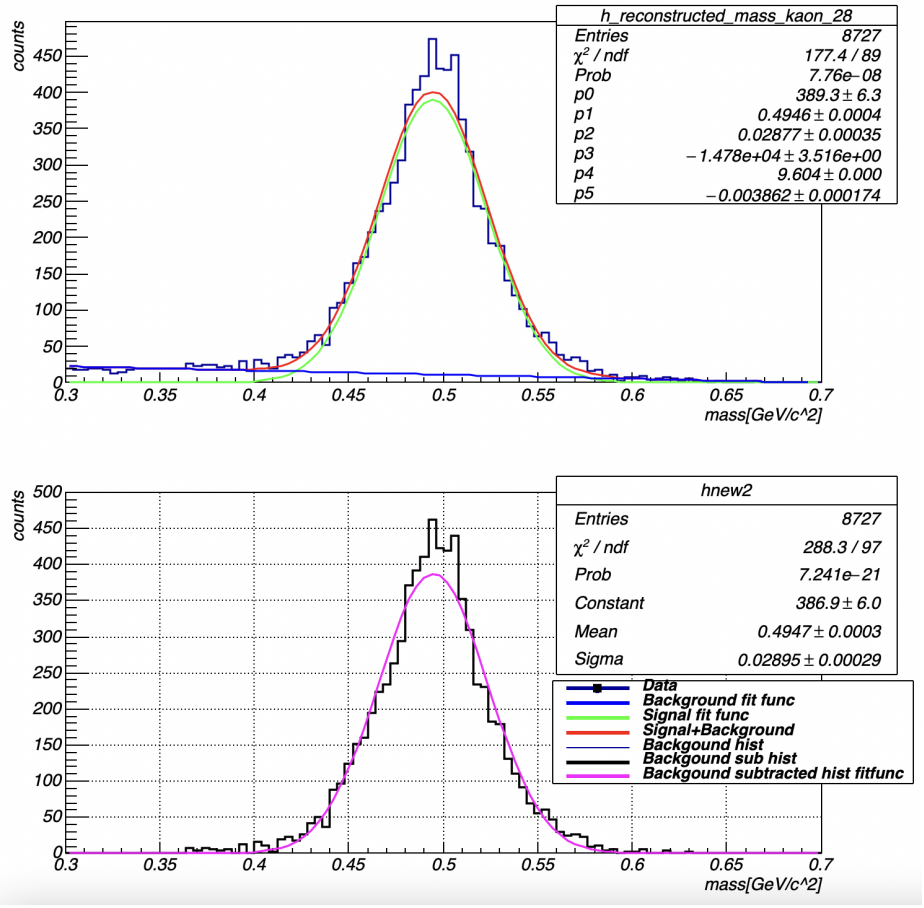

Figure B.28 Background subtracted kaon-mass histogram for the exclusive analysis, fitted with Gaussian + exponential functions for $IM^2_{p\pi^-}$ bin 1.44 – 1.45 $((\mathrm{GeV}/c^2)^2)$.

Appendix C

List of the $g13a$ runs

List of the g13a runs used in this work. In total, 546 runs were used.

53164 53165 53166 53167 53168 53169 53170 53171 53172 53173 53174 53175 53176
53177 53178 53179 53180 53181 53182 53213 53215 53216 53217 53218 53219 53220
53221 53222 53223 53224 53225 53226 53227 53231 53233 53234 53235 53236 53237
53238 53239 53240 53241 53242 53243 53244 53245 53246 53247 53248 53265 53267
53268 53269 53271 53272 53273 53274 53275 53276 53277 53281 53283 53284 53285
53286 53287 53288 53289 53290 53291 53292 53293 53296 53300 53301 53302 53304
53305 53306 53307 53308 53309 53310 53312 53313 53314 53320 53322 53323 53324
53326 53333 53335 53336 53337 53338 53339 53340 53341 53347 53348 53349 53350
53352 53353 53357 53359 53361 53362 53363 53365 53366 53367 53368 53369 53371
53372 53373 53374 53375 53376 53377 53378 53379 53380 53381 53382 53383 53384
53385 53386 53387 53390 53391 53392 53393 53403 53404 53405 53406 53407 53408
53409 53410 53411 53412 53414 53415 53416 53417 53418 53419 53420 53421 53422
53423 53424 53425 53426 53427 53428 53429 53431 53432 53433 53434 53435 53437
53438 53439 53441 53442 53443 53444 53445 53446 53448 53452 53453 53454 53455
53456 53457 53458 53459 53460 53461 53462 53463 53464 53465 53466 53467 53468
53469 53470 53471 53472 53473 53474 53475 53476 53478 53479 53481 53482 53483
53484 53485 53486 53487 53488 53489 53490 53491 53492 53493 53494 53495 53496
53497 53498 53499 53500 53501 53503 53504 53505 53506 53507 53508 53509 53510
53511 53512 53513 53514 53515 53517 53518 53519 53520 53521 53522 53523 53524
53525 53526 53527 53528 53531 53532 53538 53539 53540 53541 53542 53543 53544

53545 53546 53547 53550 53552 53553 53554 53555 53556 53557 53558 53567 53568
53569 53570 53571 53572 53573 53574 53575 53578 53579 53580 53581 53582 53583
53584 53585 53586 53587 53588 53590 53591 53592 53593 53594 53595 53596 53597
53599 53600 53601 53602 53603 53607 53608 53609 53610 53611 53612 53613 53614
53615 53616 53617 53618 53619 53620 53621 53622 53623 53624 53626 53627 53628
53629 53630 53631 53633 53634 53635 53636 53637 53638 53640 53641 53642 53643
53644 53645 53646 53647 53648 53649 53650 53651 53662 53664 53665 53666 53667
53668 53669 53670 53671 53672 53673 53683 53684 53685 53686 53687 53688 53689
53690 53691 53692 53693 53694 53695 53696 53697 53698 53700 53701 53702 53703
53704 53705 53706 53707 53708 53709 53710 53711 53712 53713 53714 53715 53716
53717 53718 53719 53720 53721 53722 53723 53724 53728 53729 53730 53731 53732
53733 53734 53735 53736 53737 53738 53739 53740 53741 53742 53743 53745 53747
53748 53752 53753 53754 53755 53756 53757 53758 53759 53760 53761 53762 53763
53764 53765 53766 53767 53768 53769 53772 53773 53774 53775 53776 53777 53778
53779 53780 53781 53782 53783 53784 53785 53786 53787 53788 53789 53790 53791
53792 53793 53794 53795 53796 53797 53798 53800 53801 53802 53803 53804 53805
53806 53807 53808 53809 53810 53811 53812 53813 53814 53815 53816 53817 53818
53820 53822 53823 53825 53826 53827 53828 53829 53830 53831 53832 53833 53834
53835 53837 53838 53839 53840 53841 53842 53843 53844 53845 53846 53847 53848
53849 53850 53851 53852 53853 53854 53855 53856 53857 53858 53859 53860 53862
53998 53999 54001 54002 54003 54004 54005 54006 54016 54017 54018 54019 54020
54021 54022 54023 54024 54025 54026 54029 54030 54031 54032 54033 54034 54035